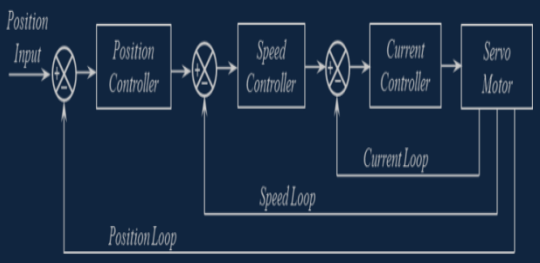

International Advanced Researches and Engineering Journal

e-ISSN

2618-575X

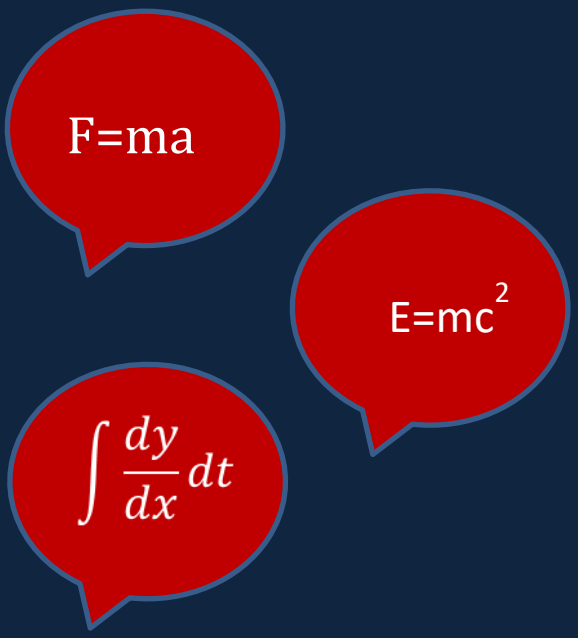

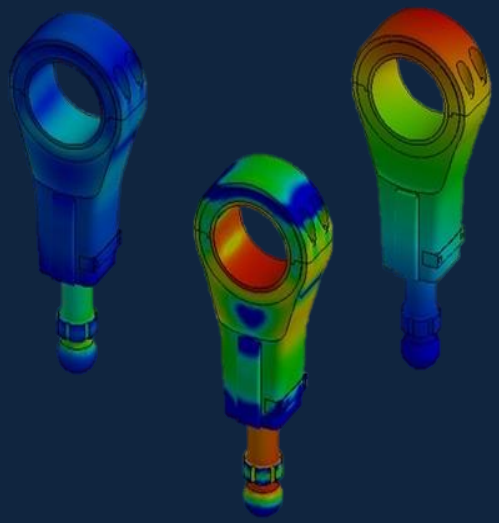

Volume 08 | **Issue** 03

December, 2024

e-ISSN: 2618-575X

Available online at www.dergipark.org.tr/en

INTERNATIONAL ADVANCED RESEARCHES
and
ENGINEERING JOURNAL

Journal homepage: www.dergipark.org.tr/en/pub/iarej

International
Open Access

Volume 08
Issue 02
August, 2024

International Advanced Researches and Engineering Journal (IAREJ) is a double-blind peer-reviewed and publicly available online journal that has Editorial Board (https://dergipark.org.tr/en/pub/iarej/board). The editor in chief of IAREJ welcomes the submissions that cover theoretical and/or applied researches on **Engineering** and related science with Engineering. The publication language of the Journal is **English**. **Writing Rules** are given in Author Guidelines (https://dergipark.org.tr/en/pub/iarej/writing-rules). IAREJ publishes **original papers** that are research papers and technical review papers.

IAREJ publication, which is **open access**, is **free of charge**. There is no article submission and processing charges (APCs).

IAREJ is indexed & abstracted in:

Crossref (Doi prefix: 10.35860/iarej.)
Directory of Open Access Scholarly Researches (ROAD)
Directory of Research Journals Indexing (DRJI)
EBSCO
Google Scholar
Index Copernicus (ICI Journal Master List)
J-Gate
TUBITAK ULAKBIM TR Dizin (TR index)
WorldCAT

Authors are responsible from the copyrights of the figures and the contents of the manuscripts, accuracy of the references, quotations and proposed ideas and the Publication Ethics (https://dergipark.org.tr/en/pub/iarej/page/4240).

e-ISSN: 2618-575X

Available online at www.dergipark.org.tr/en

INTERNATIONAL ADVANCED RESEARCHES
and
ENGINEERING JOURNAL

Journal homepage: www.dergipark.org.tr/en/pub/iarej

International
Open Access

Volume 08
Issue 03

December, 2024

TABLE of CONTENTS

Research Articles

Available online at www.dergipark.org.tr/en

INTERNATIONAL ADVANCED RESEARCHES and ENGINEERING JOURNAL

Journal homepage: www.dergipark.org.tr/en/pub/iarej

e-ISSN: 2618-575X

International Open Access

Volume 08
Issue 03

December, 2024

Research Article

Predicting medical drug usage intentions via SGD-based text classification model

Duygu Bağcı Daş [a,*]

[a] *Department of Computer Programming, Ege University, Izmir, 35100, Turkiye*

ARTICLE INFO

Article history:
Received 03 Juney 2024
Accepted 14 December 2024
Accepted 20 December 2024

Keywords:
Drug usage intention
Machine learning
Medical drug usage
Text classification
Text mining

ABSTRACT

The effects of medical drugs and their usage purposes vary among individuals due to the chemical composition of drugs, side effects, genetics, etc. Even if those effects are to be discovered pharmacologically, they cannot be fully understood. Hence, it becomes essential to analyze the individuals' reviews and experiences to unearth such effects and find out which other purposes drugs are used for, in addition to the target disease they are developed to cure. Text classification methods present various solutions to analyze those reviews effectively. Generally, these effects are investigated in terms of emotional analysis of medical drug usage experience as positive or negative. However, some drugs can be used for more than one specific treatment. For example, an antipsychotic drug can be used for both depression and anxiety or ADHD. Therefore, the effects of medical drug users and drug names to be associated with the review of the studies should be covered comprehensively. Based on this motivation, this study proposed a lightweight model for the prediction of medical drug usage intentions using text-based patient reviews. For this purpose, TF-IDF and bigram methods are used for text classification in the feature extraction step, then the Stochastic Gradient Descent (SGD) classifier is used for prediction and compared to other popular machine learning algorithms. Classification results indicate that the SGD and TF-IDF-Bigram approach effectively predicts drug usage intentions for medical purposes with an accuracy of 98.42%. Based on the outcomes, it is concluded that the findings of this study may be beneficial in pharmaceutics or medicine considering drug design, reducing side effects, health management, treatment adherence and process design, and personalized medicine.

1. Introduction

Machine learning techniques have been increasingly used in recent decades in the medical field [1-3]. As a subdomain of Machine Learning, text classification is a methodology for structuring, organizing, and tagging a topic based on texts. This methodology is utilized in the medical field, including diagnosis, prognosis, personalized medicine, etc. For instance, a disease could be diagnosed by using former patients' complaints, or by analyzing their sentiments on social media. All of these abilities make text classification more popular among researchers. Some of the studies presented by the researchers are briefly described below.

Liu [4] presented a high-quality classifier for supporting healthcare information support in Chinese disease-related information. The classifier was designed to help identify the cause, symptom, curing, side effects, and prevention of cancer. Billyan et al. [5] performed sentiment analysis with machine learning approaches for restaurant businesses. They used Fuzzy K-Nearest Neighbor as the classification method to predict whether the customer reviews are positive or negative. Pratama and Sarno [6] predicted the personality of individuals based on the text that they were written on Twitter. They classified English and Indonesian languages by using Naive Bayes (NB), K-Nearest Neighbors (KNN), and Support Vector Machine (SVM). Sulea et al. [7] investigated the text classification methods that can support law professionals. They applied several machine learning methods to predict the ruling and the law area. Olsson et al. [8] aimed to classify Czech documents using cross-language text classification with English training data.

In addition to those studies, researchers have investigated the implementation and combination of machine learning algorithms to improve the effectiveness of text classification. Some of the studies related to this

* Corresponding author. Tel.: +0-232-311-1475; Fax: +0-232-388-7599.
E-mail addresses: duygu.bagci.das@ege.edu.tr
ORCID: 0000-0003-4519-3531
DOI: 10.35860/iarej.1495330

topic are as follows. Li and Park [9] presented a novel method that helps to classify documents effectively. They utilized the learning phase evaluation back propagation neural network and singular value decomposition that improved the document classification efficiently. Tang et al. [10] proposed a Bayesian classification approach for automatic text classification. They used class-specific features by following Baggenstoss's PDF Projection Theorem to rebuild the PDF within the raw data space. Kumar et al. [11] investigated the text classification performance on machine learning by using the Back Propagating Artificial Neural Network (ANN) model. Shen et al. [12] presented an improved parallel Bayesian algorithm theoretically and experimentally to improve the speed of the classification on the Hadoop cloud platform. Dalal and Zaveri [13] proposed an enhanced hybrid classification method, which is the combination of NB and SVM for text document preprocessing.

Shokrpour et al. [14] investigated the best algorithm that classifies drug interactions. They used NB, Multinominal NB, Zero R, Jrip, LibSVM, j48, Random Forest, and Bagging algorithms to evaluate the classes. Chai et al. [15] used 25K tweets that describe drug use to obtain drug effectiveness by performing relation extraction. Aramaki et al. [16] investigated the extraction of adverse drug events and effects by using clinical records. They divided their study into determining the amount of information that existed in the files and automatic extracting of the Natural Language Processing (NLP) system. Graber et al. [17] used online reviews of drugs related to five disorders to perform aspect-based sentiment analysis, applying cross-domain, and cross-data learning. They used two datasets, namely, Drugscom and Druglib. Lavecchia [18] investigated machine-learning approaches within the scope of drug discovery. Five different machine learning algorithms are compared with each other in terms of classification error, computational cost, memory requirements, complexity for implementation, on/offline application, interpretation, advantages, and disadvantages.

Abada et al. [19] investigated the relationships between substance use and mental health conditions (alcohol, opioids, tobacco, anxiety, depression, insomnia) in addiction. They identified patterns and correlations across these categories using five Machine Learning algorithms and Principal Component Analysis (PCA). Elahi et al. [20] developed an attention-based graph network, a recommendation framework that combines both relational and contextual information to improve recommendation systems. Their model addresses challenges in large, sparse datasets, specifically in health informatics, by using a user-specific attention mechanism to personalize recommendations.

This research proposes a predictive model for drug usage intentions, which explores how drugs may be used for conditions beyond their intended purpose whereas most of the studies in this field generally focus on drug-based adverse effects and sentiment analysis. This study investigated the prediction of drug usage intentions using machine learning-based text classification from an online review dataset by using the Python 3.7 NLTK tool. The Stochastic Gradient Descent (SGD) classifier with TF-IDF (Term Frequency-Inverse Document Frequency) and bigram feature extraction techniques is used for the first time for predicting drug usage intentions.

The rest of the paper is arranged as follows: Section 2 explains the necessary preparations, preprocessing, and feature extraction methods to perform machine learning-based text classification. Section 3 presents the effects of the preprocessing techniques on the model performance and the classification results. Finally, the discussion about the outcomes is given in Section 4.

2. Material and Method

2.1 The Dataset and Preprocessing

Drugs.com dataset, which contains user reviews on specific medical drugs, is used to evaluate an effective method for the prediction of drug usage intentions. The dataset contains 215063 reviews of 6345 drugs [17]. The top fifteen usage based on the reviews are selected because the dataset is unbalanced (e.g., there are 2 reviews for only one drug condition, whereas there are 28788 for another drug condition). Table 1 shows the dataset summary and Table 2 contains some example reviews in the pharmaceutical field. For all experiments, the dataset is split into training and testing sets at a ratio of 75% - 25%.

Table 1. Dataset summary [17]

Abb.	Condition Name	Number of Reviews
C1	Birth Control	28788
C2	Pain	6145
C3	Acne	5588
C4	Insomnia	3673
C5	Obesity	3568
C6	Diabetes Type 2	2554
C7	High Blood Pressure	2321
C8	Abnormal Uterine Bleeding	2096
C9	Depression	9069
C10	Anxiety	5904
C11	Bipolar Disorder	4224
C12	Weight Loss	3609
C13	ADHD	3383
C14	Emergency Contraception	2463
C15	Vaginal Yeast Infection	2274

Table 2. Example reviews [17]

This drug has turned down the volume on a lot of my voices. Which is great. I sleep better and take more naps during the day. Also notice my appetite increased which is where I think people mean they gain weight on this med. I just exercise an hour a day. My mood is kinda flat lined.
I used them and within 6 hours my eyes swelled almost shut and cheeks puffed up 2 weeks later. I still have red watery eyes but thankfully the swelling is finally gone. I will never use this product again obviously but it is also incredibly expensive. I have never had an allergic reaction to any medication before so this was very unexpected.

Figure 1 depicts the steps of a machine learning-based text classification procedure. In the first step, the corpus is purified from unnecessary data by using various pre-processing techniques on the corpus data as illustrated in Figure 2. This is a critical process since it has a direct impact on the model performance. Then, feature extraction is performed and a feature vector is created. The created feature vectors are associated with labels and the classifier model is trained with this data. The trained model is tested with new unseen data.

Many stop words in English are used in Natural Language Processing. Table 3 shows a list of the used stop words existing in NLTK library.

Figure 1. Machine learning-based text classification

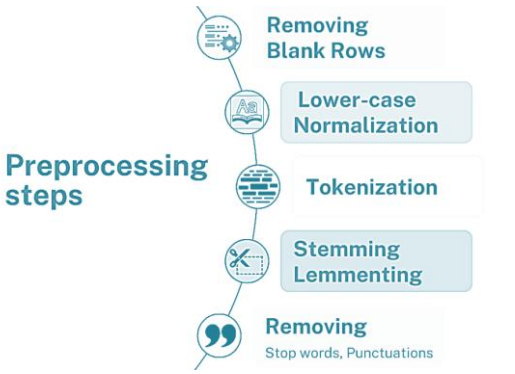

Figure 2. Preprocessing steps for the proposed text classification model

Table 3. Stop words list

i	they	a	in	own	doesn
me	them	an	out	same	doesnt
my	their	the	on	so	hadn
myself	theirs	and	off	than	hadnt
we	themselves	but	over	too	hasn
our	what	if	under	very	hasnt
ours	which	or	again	s	haven
ourselves	who	because	further	t	havent
you	whom	as	then	can	isn
youre	this	until	once	will	isnt
youve	that	while	here	just	ma
youll	thatll	of	there	don	mightn
youd	these	at	when	dont	mightnt
your	those	by	where	should	mustn
yours	am	for	why	shouldve	mustnt
yourself	is	with	how	now	needn
yourselves	are	about	all	d	neednt
he	was	against	any	ll	shan
him	were	between	both	m	shant
his	be	into	each	o	shouldn
himself	been	through	few	re	shouldnt
she	being	during	more	ve	wasn
shes	have	before	most	y	wasnt
her	has	after	other	ain	weren
hers	had	above	some	aren	werent
herself	having	below	such	arent	won
it	do	to	no	couldn	wont
its	does	from	nor	couldnt	wouldn
its	did	up	not	didn	wouldnt
itself	doing	down	only	didnt	

2.2 TF-IDF and Bigram methods

In this study, feature extraction procedure is performed by using the TF-IDF, and the bigrams. The SGD is used to classify drug usage intentions.

The TF-IDF and the bigram calculations are frequently used techniques in text classification processes. TF-IDF is derived from Term Frequency (TF) and Inverse Document Frequency (IDF). TF refers to the number of times a term occurs in a document. Generally, the frequency of a term in a document indicates the importance of such a term in that document. IDF is a metric indicating how common or rare a term is. If a term is very common, its IDF value will be low; if it is rare, the IDF value will be high. This shows the importance of a term existing in the corpus of text [21].

TF and IDF are utilized to evaluate the importance of a specific term in a text.

The multiplication of TF and IDF values of a term gives the importance of that term in both the document and the overall collection. The mathematical expressions of TF, IDF, and TF-IDF are briefly given as follows.

$$TF(i,d) = \frac{n_{i,d}}{\sum_{i' \in d} n_{i',d}} \quad (1)$$

$$IDF(i,C) = log \frac{N_c}{|\{d \in C : i \in d|} \quad (2)$$

$$TF\text{-}IDF(i,d) = TF(i,d) \; x \; IDF(i,C) \quad (3)$$

where $n_{i,d}$ is number of the word *i* shows up in the document *d*, $\sum_{i' \in d} \boldsymbol{n_{i',d}}$ is the total word count in document *d*, N_c is the number of documents in a Corpus, and $|\{\boldsymbol{d} \in \boldsymbol{C}: \boldsymbol{i} \in \boldsymbol{d}|$ represents the number of documents where the word *i* exists. N-grams can take different forms, such as single words (unigrams), pairs of words (bigrams), trios of words (trigrams), or sequences of any length. Here *n* indicates the number of consecutive words. N-grams are often used to extract unique patterns in a text, obtaining meaningful data from textual data.

In this study, the bigrams are denoted in texts as follows. For example, “side effects” or “allergic symptoms” are some bigrams due to the frequent use of these two words together, and such bigrams hold representative characteristics for understanding pharmaceutical text data regarding the use of drugs.

2.3. Stochastic Gradient Descent (SGD) Classifier

SGD Classifier is a linear classifier a classification model (such as SVM or logistic regression) optimized by the SGD. As a type of SVM, SGD is defined as a classification approach whose goal is finding the optimal decision boundary in order to distinguish instances of different classes [22]. SGD is an effective technique to be implemented in large datasets since it iteratively updates the model parameters by calculating gradients on randomly chosen mini-batches of the train data instead of considering the entire dataset. Owing to this positive aspect, its training procedure is fast and it is scalable for large datasets. Mathematically, SGD can be expressed as follows.

$$O(w) = 1\frac{1}{n}\sum_{i=1}^{n} L(y_i \hat{y}_i) + \mu \|w\|^2 \quad (4)$$

where *O(w)* represents the objective function while *n* is the number of training samples. $L(y_i \hat{y}_i)$ is the loss function and μ is the regularization parameter depending on *w* representing the weight vector. In this paper, the modified Huber loss function and L2 regularizer are considered.

The success of the considered approach is determined by interpreting the accuracy results of the classification.

2.4 One-vs-Rest (OvR) approach

One-vs-Rest (OvR) is a method in multi-class classification that converts the problem into binary classification problems. A separate binary classifier is trained for each class, and each classifier tries to distinguish that class (positive instances) from all other classes (negative instances). The test data is then applied to all classifiers, and each classifier makes a prediction. The ultimate decision is based on the classifier with the highest score. The evaluation of the SGD model is performed based on the OvR approach within the study.

3. Results

The analysis results of the different text classification processes by using machine learning algorithms are evaluated for the bigram and the TF-IDF methods. The assessment of the classifier is made considering accuracy, precision, recall, and F1 scores.

Figure 3 shows the performance metrics for the bigram considering NB (Clf-1), SVM (Clf-2), KNN (Clf-3, and RF (Clf-4) classifiers as basic classifiers. As seen in Figure 3, Clf-2 that used the bigrams had the highest performance owing to its accuracy (81%), precision (0.85), recall (0.71), and f1 score (0.81) values whereas Clf-1 classifier had the lowest performance when used Bigrams.

Figure 4 presents the performance metrics for the same classifiers where they are utilized with the Bigrams and the TF-IDF. According to the results given in Figure 4, it is observed that Clf-2 classifier shows the best performance due to its accuracy (89%), precision (0.90), recall (0.85), and f1 score (0.87). On the other hand, Clf-1 classifier has the worst performance when considering the same text processing combination.

Regarding both Figures 3 and 4, Clf-3 is placed second and Clf-4 is the third best approach in classifying other purposes of drug use. Comparing the text processing techniques, it is observed that using the TF-IDF with the bigrams as a combination increased the accuracy by 8%, meaning that it is beneficial to use such text processing methods together. On the other hand, the performance metrics did not reach the desired level using Clf-1, Clf-2, Clf-3, and Clf-4. Due to its promising performance in handling large datasets as expressed in Section 2.3 the SGD classifier, as an improved version of Clf-2 (SVM), is employed to leverage the classification performance to a higher level.

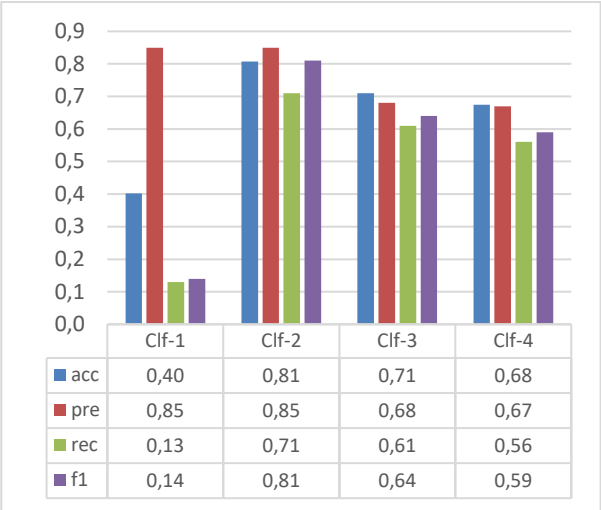

Figure 3. The performance metrics of different base classifiers for the Bigram technique

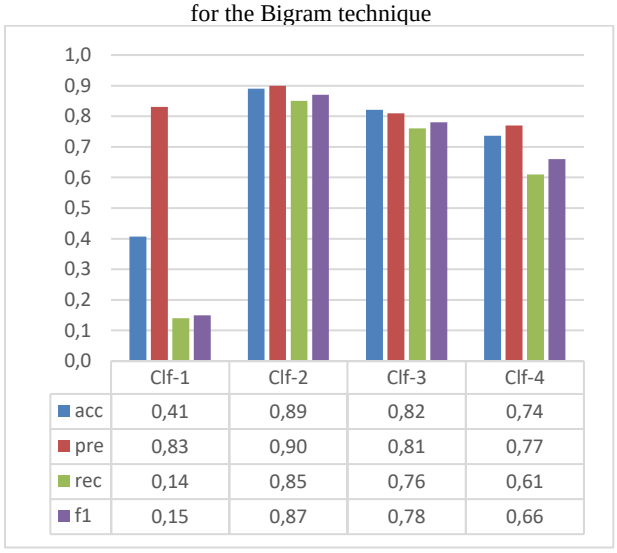

Figure 4. The performance metrics of different base classifiers for the Bigram and TF-IDF techniques

The classification results using the SGD (Clf-5) classifier and the bigrams – TF-IDF text processing combination are presented in Table 4. As seen in Table 4, Clf-5 significantly increased the accuracy from 89% to 98.42%. Owing to its high precision (0.98) and recall (0.98) values given in Table 5 indicate the robustness and responsiveness of the model meaning that it can deal with distorted and different data effectively.

Class-based results given in Table 5 show that classes C9 (Depression) and C14 (Emergency Contraception) are perfectly associated with the corresponding drug. The use of drugs for Diabetes Type 2 and High Blood Pressure are classified as less accurate than others, with accuracy values of 96% and 97%, respectively. All other medical drug usage conditions are successfully classified with accuracy values between 97% and 100%, meaning that Clf-5 with the bigrams and TF-IDF text processing can be utilized as an effective tool for understanding the effect of the drugs in treating diseases or conditions different from that they are developed for.

Table 4. Accuracy Metrics of the Bigram-TF-IDF/SGD

Class No	Accuracy	Class No	Accuracy
C1	98.26%	***C9***	99.84%
C2	99.01%	***C10***	99.30%
C3	99.47%	***C11***	98.97%
C4	96.62%	***C12***	97.79%
C5	98.23%	***C13***	99.07%
C6	97.00%	***C14***	99.87%
C7	95.71%	***C15***	97.90%
C8	99.31%	***AVG***	**98.42%**

Table 5. Weighted average performance metrics of the Bigram-TF-IDF/SGD Method

Class No.	Precision	Recall	F1 Score
C1	0.98	0.98	0.98
C2	0.99	0.99	0.99
C3	0.99	0.99	0.99
C4	0.96	0.97	0.96
C5	0.98	0.98	0.98
C6	0.97	0.97	0.97
C7	0.96	0.96	0.96
C8	0.99	0.99	0.99
C9	1.00	1.00	1.00
C10	0.99	0.99	0.99
C11	0.99	0.99	0.99
C12	0.98	0.98	0.98
C13	0.99	0.99	0.99
C14	1.00	1.00	1.00
C15	0.98	0.98	0.98
AVG	***0.98***	***0.98***	***0.98***

Some deep learning-based approaches are proposed in the related field. For example, Al-Hadhrami et al. [23] evaluated the bidirectional long short-term memory and convolutional neural network (BiLSTM-CNN) models for sentiment analysis of patient drug reviews. They considered two different datasets where the BiLSTM-CNN model achieved an accuracy of 96%. Dandala et al. [24] studied adverse drug events based on Deep learning techniques. They employed a combined BiLSTM and conditional random fields (CRF) model for medical entity detection and a BiLSTM-attention network to understand the relationship between drugs and symptoms. The F-measure values of the proposed combined approach are 0.83 for entity detection and 0.87 for relation detection. Colon-Ruiz and Segura-Bedmar [25] compared different Deep learning architectures for sentiment analysis of drug reviews. They considered CNN, LSTM, and the

combinations of these models. Additionally, they investigated the impact of pre-trained word embeddings, including Bidirectional Encoder Representations from Transformers (BERT) combined with Bi-LSTM. They found that BERT achieved the best results with an accuracy of 90%, although it required a significant amount of training time. On the other hand, CNN achieved acceptable results with a shorter training time.

This study offers an alternative model for predicting medical drug usage conditions, and intentions are successfully classified with accuracy values between 97% and 100%.

4. Conclusions

This study investigated the prediction of the use of drugs for different purposes than their main target condition using machine learning-based text classification from an online review dataset. The conclusions of the study are presented as follows:

- The proposed technique, SGD, TFIDF-Bigrams is effective for the prediction of the use of medical drugs for different conditions than they are developed to treat.
- Preprocessing (stemming, lemmatizing, tokenizing, removing stop words and punctuations, methods affected the performance positively and therefore, should be considered meticulously.
- It is seen from the results that using the bigram and the TF-IDF in combination improved the classification regardless of the classifier.
- The best result is obtained for the SGD – TF-IDF & Bigrams method by an accuracy value of 98.42%. In addition, owing to its high precision (0.98), recall (0.98), and F1 score (0.98), it can be concluded that it is a robust and responsive technique.
- Similar conditions are not recognized during classification. For instance, Acne and Birth Control, which are related to hormone treatment, are poorly classified. A similar situation is observed for Anxiety and Depression. Taking this conclusion into account may improve the model's accuracy in future works.
- The findings of this study may be beneficial in pharmaceutics or medicine considering drug design, reducing side effects, health management, treatment adherence and process design, and personalized medicine.

Declaration

The author(s) declared no potential conflicts of interest with respect to the research, authorship, and/or publication of this article. The author(s) also declared that this article is original, was prepared in accordance with international publication and research ethics, and ethical committee permission or any special permission is not required.

Author Contributions

Duygu Bagci Das developed the methodology, performed the analysis, supervised and improved the study, wrote the manuscript, and proofread the manuscript.

References

1. Şen Ö., S.Bozkurt Keser, and K. Keskin, *Early stage diabetes prediction using decision tree-based Ensemble Learning Model.* International Advanced Researches and Engineering Journal, 2023. **7**(1): p. 62-71.
2. Jahan S., *Major depressive disorder diagnosis from electroencephalogram data and potential treatment with dimethyltryptamine.* International Advanced Researches and Engineering Journal, 2023. **7**(2):p. 90–96.
3. Tuncer T., E. Aydemir, F. Özyurt, S. Dogan, S. B. Belhaouarı, and E. Akbal, *An automated COVID-19 respiratory sound classification method based on novel local symmetric Euclidean distance pattern and Relieff Iterative MRMR feature selector*. International Advanced Researches and Engineering Journal, 2021. **5**(3): p.334–343.
4. Liu R.-L., *Text classification for healthcare information support*, in 20th International Conference on Industrial, Engineering, and Other Applications of Applied Intelligent Systems. 2007. Kyoto, Japan: p. 44–53.
5. Billyan B., R. Sarno, K.R. Sungkono, and I.R. Tangkawarow, *Fuzzy k-nearest neighbor for restaurants business sentiment analysis on TripAdvisor*, in 2019 International Conference on Information and Communications Technology. 2019. Kuala Lumpur, Malaysia: p. 543-548.
6. Pratama B. Y. and R. Sarno, *Personality classification based on Twitter text using naive Bayes, KNN and SVM*, in 2015 International Conference on Data and Software Engineering (ICoDSE), 2015. Yogyakarta, Indonesia: p. 170-174.
7. Suela O-M., M. Zampieri, S. Malmasi, M. Vela, L.P. Dinu, and J. van Genabith [cited 2024 1 Jun]; Available from: https://arxiv.org/abs/1710.09306
8. Olsson J. S., D. W. Oard, and J. Hajič, *Cross-language text classification*, in Proceedings of the 28th annual international ACM SIGIR conference on Research and development in information retrieval, 2005. Salvador Brazil: p.645-646.
9. Li C.H. and S.C. Park, *An efficient document classification model using an improved back propagation neural network and singular value decomposition*. Expert Systems with Applications, 2009. **36**(2): p.3208–3215.
10. Tang B., H. He, P. M. Baggenstoss, and S. Kay, *A bayesian classification approach using class-specific features for text categorization.* IEEE Transactions on Knowledge and Data Engineering, 2016, **28**(6):p. 1602–1606.
11. Kumar R. R., M. B. Reddy, and P. Praveen, *Text Classification Performance Analysis on Machine Learning.* International Journal of Advanced Science and Technology, 2019. **28**(20): p. 691–697.
12. Shen P., H. Wang, Z. Meng, Z. Yang, Z. Zhi, R. Jin, and A. Yang, *An Improved Parallel Bayesian Text Classification Algorithm.* Review of Computer Engineering Studies, 2016. **3**(1): p. 6–10.
13. Dalal M. K. and M.A. Zaveri, *Automatic text classification: A technical review*. International Journal of Computer

Applications, 2011. **28**(2): p. 37–40.
14. Shokrpour N., R. Rezaee, R. Akbari, M. Nasiri, and F. Foroughinia, *An evaluation of classification algorithms for prediction of drug interactions: Identification of the best algorithm.* International Journal of Pharmaceutical Investigation, 2018. **8**(2): p. 92-99.
15. Chai Z., X. Wan, Z. Zhang, and M. Li, *Harvesting drug effectiveness from social media*, in Proceedings of the 42nd International ACM SIGIR Conference on Research and Development in Information Retrieval, 2019. Paris, France: p.55-64.
16. Aramaki E., Y. Miura, M. Tonoike, T. Ohkuma, H. Masuichi, K. Waki, and K. Ohe, *Extraction of adverse drug effects from clinical records.* Studies in health technology and informatics, 2010. **160**(1): p.739–743.
17. Gräßer F., S. Kallumadi, H. Malberg, and S. Zaunseder, *Aspect-based sentiment analysis of drug reviews applying cross-domain and cross-data learning*, in Proceedings of the 2018 International Conference on Digital Health, 2018. Lyon France: p.121-125.
18. Lavecchia A., *Machine-learning approaches in drug discovery: Methods and applications.* Drug Discovery Today, 2015. **20**(3): p.318–331.
19. Abada W., A. Bouramoul, and M. S. Kahil, *How machine learning algorithms can examine patterns in multiple substance addictions: Predicting the effects and interactions of psychoactive substances*. International Journal of Computers and Applications, 2024. **46**(11): p.1045–1055.
20. Elahi E., E. Elahi, S. Anwar, B. Shah, Z. Halim, A. Ullah, I. Rida, M. Waqas, *Knowledge graph enhanced contextualized attention-based network for responsible user-specific recommendation.* ACM Transactions on Intelligent Systems and Technology, 2024. **15**(4): p. 1–24.
21. Korkmaz T., A. Çetinkaya, H. Aydin, and M. A. Barişkan, *Analysis of whether news on the internet is real or fake by using deep learning methods and the TF-IDF algorithm.* International Advanced Researches and Engineering Journal, 2021. **5**(1): p. 31–41.
22. Zhang T., *Solving large scale linear prediction problems using stochastic gradient descent algorithms*, in Twenty-first international conference on Machine learning- ICML '04, 2004.
Banff, Alberta, Canada: p.116-124.
23. Al-Hadhrami S., T. Vinko , T. Al-Hadhrami, F. Saeed, and S.N. Qasem, *Deep learning-based method for sentiment analysis for patients' drug reviews*. PeerJ Computer Science, 2024. **10**: p. e1976.
24. Dandala B., V. Joopudi, and M. Devarakonda, Adverse *Drug Events Detection in clinical notes by jointly modeling entities and relations using Neural Networks.* Drug Safety, 2019. **42**(1): p.135–146.
25. Colón-Ruiz C. and I. Segura-Bedmar, *Comparing deep learning architectures for sentiment analysis on drug reviews.* Journal of Biomedical Informatics, 2020. **110**: p.103539.

Available online at www.dergipark.org.tr/en

INTERNATIONAL ADVANCED RESEARCHES and ENGINEERING JOURNAL

Journal homepage: www.dergipark.org.tr/en/pub/iarej

e-ISSN: 2618-575X

International Open Access

Volume 08
Issue 03

December, 2024

Research Article

Evaluation of Tawa Khana as a vernacular floor heating system for enhancing building energy efficiency: A case study of Kabul City, Afghanistan

Ahmad Walid Ayoobi [a,b,*], ***Mehmet Inceoğlu*** [c] ***and Fazalrahman Ikhlas*** [a]

[a]*Kabul Polytechnic University, Faculty of Construction, Department of Architecture, Kabul Afghanistan*
[b]*Eskisehir Technical University, Graduate School of Sciences, Department of Architecture, Eskisehir, Turkey*
[c]*Eskisehir Technical University, Faculty of Architecture & Design, Department of Architecture, Eskisehir, Turkey*

ARTICLE INFO

Article history:
Received 05 June 2024
Accepted 03 October2024
Published 20 December 2024

Keywords:
Tawa Khana (Ondol)
Vernacular architecture
Energy efficiency
Simulation
Kabul city

ABSTRACT

This study investigates the potential of Tawa Khana, a vernacular heating system used in Asian countries, particularly Afghanistan, to improve building energy efficiency. Tawa Khana utilizes radiant floor heating, drawing warmth from a cooking stove or fireplace to heat the floor and subsequently the room. However, it is neglected in contemporary designs, and there is a predicted risk of losing this valuable knowledge entirely within the next few decades. This study aims to evaluate Tawa Khana's features, including its design and construction methods, with the goal of establishing a design manual for Tawa Khana. Furthermore, it analyzes the multifaceted contributions of Tawa Khana to building energy efficiency. For this purpose, a case study evaluation with comprehensive simulations analysis through the DesignBuilder program was conducted. The results indicate that Tawa Khana is applicable with minimal additional technology, increasing room temperature by 4 degrees Celsius, demonstrating its effectiveness as a sustainable heating strategy. This vernacular technique efficiently utilizes waste heat from cooking activities, reducing reliance on conventional heating systems and promoting energy conservation.

1. Introduction

The relationship between architecture and the environment is intrinsically intertwined, mirroring the interconnectedness of humans and nature. Vernacular architecture exemplifies this dynamic interaction across various cultures [1]. However, the construction sector raises significant concerns in contemporary society due to human activities like deforestation, land-use changes, urbanization, and building development [2]. With nearly half of the global population residing in urban areas [3], the building sector emerges as a critical contributor to resource consumption, energy use, and greenhouse gas (GHG) emissions [4]. Studies indicate that buildings account for approximately 40% of resource utilization, 30% of total energy consumption, and 30% of global carbon emissions [5–10]. Air pollution represents a pressing challenge, particularly in Kabul, the capital of Afghanistan [11]. This problem primarily stems from urban expansion and energy consumption within buildings, with pollutants like NO_2, SO_2, and CO being the most significant concerns. Kabul's poor air quality and overpopulation place it among the world's most polluted cities, alongside metropolises like New Delhi and Beijing [11]. Research suggests that coal power generation, wood and gas burning, and biomass use for heating during winters are the main sources of these pollutants in Kabul [12]. The concentration of NO_2, CO, and SO_2 in the troposphere demonstrably decreases from winter to summer. Existing data indicates that Kabul's residential buildings rely on electricity and natural gas for energy during warmer seasons, while colder months necessitate wood, coal, charcoal, and natural gas [13]. Furthermore, rapid urbanization and the construction of buildings that deviate from established standards contribute to environmental degradation and resource depletion [14]. In conclusion, implementing energy-efficient strategies in building design and construction, along with a comprehensive integration of renewable energy sources, presents a viable solution to reduce air pollution levels associated with energy consumption [15].

In contrast, vernacular architecture prioritizes the efficient utilization of minimal resources and energy,

* Corresponding author. Tel.: *+90-552-268-2274* .
E-mail addresses: a_w_a@ogr.eskisehir.edu.tr *(AW.Ayoobi)*, mehmeti@eskisehir.edu.tr *(M. Inceoğlu)*, fazalrahman.ikhlas@kpu.edu.af *(F.Ikhlas)*
ORCID: 0000-0001-6623-7682 *(AW.Ayoobi)*, 0000-0001-5264-8755 *(M. Inceoğlu)*, 0009-0002-2473-1943 *(F.Ikhlas)*
DOI: 10.35860/iarej.1496059

while simultaneously serving as an embodiment of cultural and social values. Research suggests that neglecting the principles and resources employed in vernacular architecture poses a significant challenge in addressing contemporary urban housing issues [16]. Modern buildings are responsible for a substantial portion of global energy consumption and greenhouse gas emissions, exceeding 40% and 30% respectively [17]. When compared to modern designs, vernacular architecture demonstrates a greater degree of environmental adaptability due to principles honed over generations [17]. Multiple studies conducted across diverse regions and time periods have consistently corroborated the energy efficiency and sustainability of vernacular architectural techniques [18]. Notably, the past decade has witnessed a surge in interest towards vernacular design principles for heating and cooling purposes, aligning with the growing movement of energy-efficient architecture [19]. However, despite this recent upsurge in interest [20], the comprehensive potential and benefits of vernacular architecture remain underrecognized and insufficiently integrated into modern design practices.

Currently, Kabul residences experience a significant increase in energy consumption during winter due to reliance on coal and wood for space heating [12]. Wood, charcoal, and coal remain the primary heating sources for homes throughout Kabul's cold seasons. Therefore, incorporating vernacular design principles into building practices becomes crucial for reducing energy demand, particularly during winters. However, contemporary building design in Kabul City often fails to capitalize on these energy-efficient vernacular strategies. Traditional Afghanistan's techniques, often implemented in their basic form for rural dwellings, are rarely incorporated or entirely disregarded in most urban constructions, particularly in Kabul. This trend is particularly concerning for Tawa Khana, a vernacular heating system. Its application is diminishing even in rural areas due to its exclusion from contemporary design practices. The continued neglect of Tawa Khana in contemporary architecture, coupled with a lack of research on its adaptation for modern buildings, suggests a potential risk of losing this valuable knowledge entirely within the next few decades. Existing studies on Tawa Khana primarily focus on its discussion rather than providing substantial information about its design methods and contributions to reducing building energy demand [21,22].

This research delves into the potential of Tawa Khana, a traditional Afghanistan's heating system. By thoroughly evaluating its thermal efficiency and design principles, the study aims to breathe new life into this neglected energy-saving technique. The study seeks to establish a replicable design manual for Tawa Khana, promoting its use in contemporary building practices to enhance energy efficiency. Furthermore, the research will utilize comparative simulations to showcase the applicability and energy-saving benefits of Tawa Khana within Kabul's building design.

This research significantly contributes to the existing body of knowledge on Tawa Khana as a vernacular technique that effectively utilizes waste heat from cooking to reduce reliance on traditional heating systems, thereby promoting energy conservation. Furthermore, the study revitalizes this valuable cultural heritage by providing a detailed manual for the design and construction of this strategic system. Through rigorous investigation, the study unveils the diverse benefits of Tawa Khana for sustainable building design. Ultimately, this research offers a practical framework for architects and policymakers to integrate this approach into their designs and policies, thereby significantly enhancing building energy efficiency.

2. Material and Methods

Vernacular design solutions have historically adapted to specific environments and purposes, often employing a variety of techniques to achieve thermal comfort throughout the year, providing warmth during winters and coolness during summers [23]. This body of knowledge represents a valuable resource, accumulated over generations, that offers valuable lessons for contemporary architecture [24]. Notably, vernacular architecture prioritizes passive environmental control techniques, demonstrably achieving high levels of energy efficiency [24]. These techniques encompass maximizing natural ventilation, incorporating insulation, strategically utilizing shading, and employing thermal mass for heat storage and release. Within the context of this study, Tawa Khana (Ondol) is identified as the most prominent vernacular strategy for building heating. To analyze its contribution to building heating demand, DesignBuilder, a well-established building energy modeling tool, will be employed.

2.1. Tawa Khana (Ondol)

Tawa Khana (Ondol) exemplifies its environmental commitment through its promotion of energy efficiency and its sensitivity to site-specific factors. This vernacular heating system, primarily found in Afghanistan, shares similarities with other historical approaches. Notably, the Korean Ondol floor heating system, dating back to 400 B.C., also utilizes a fire pocket for both cooking and heating, promoting energy efficiency [25]. Furthermore, Anatolian Seljuk architecture employed a similar central heating method, where smoke from a hypocaust (an underfloor heating system) in a nearby bath traveled through terracotta pipes laid underground, distributing heat throughout connected rooms [26]. These historical examples demonstrate the cross-cultural application of similar principles for efficient space heating.

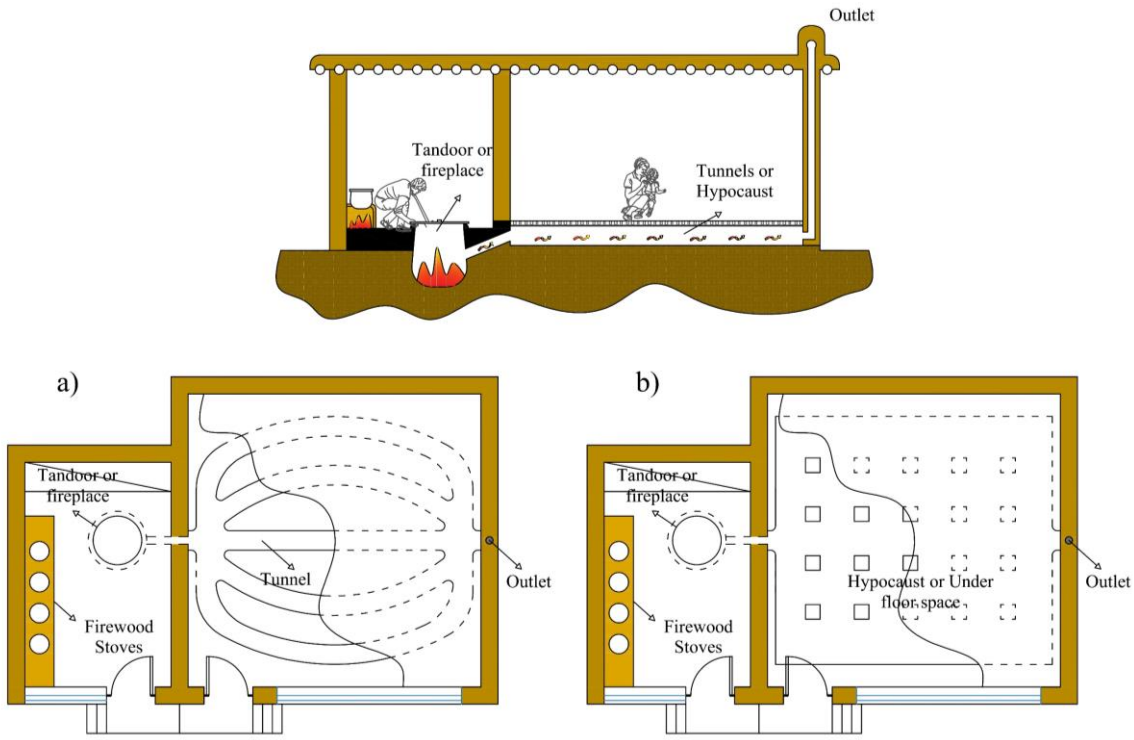

Figure 1. Plan and cross-section of a living space and kitchen featuring a Tawa Khana (Ondol), a) Tawa Khana featured tunnel structures, b) Tawa Khana featured hypocaust structures.

Tawa Khana functions as a radiant heating system. The heat source originates from a clay oven, known as the Tandoor, typically situated in the kitchen. This primary heat source can be supplemented by stoves, ovens, wood, or charcoal heaters located either within the kitchen or externally. As the heat source is used, particularly during cooking processes, residual warmth is circulated through a network of interconnected heating tunnels constructed beneath the building's floors (Figure 1). This design facilitates the transfer of heat through radiation, warming the floor surfaces and occupants by contact or thermal radiation.

The combustion process within the Tandoor generates hot air that travels through the tunnel or hypocaust, a network of channels constructed beneath the room's floors [27]. This network of tunnels guides the warmed air throughout the designated rooms. Upon reaching the end of the circulation path, the heated air, containing smoke, is expelled through a designated outlet situated on the opposing wall [28]. The interior surfaces of these tunnels are lined with flat stones, functioning as radiant heat emitters that effectively warm the surrounding spaces. These flat stones possess a high thermal mass, a property that allows them to store significant amounts of heat. This stored thermal energy is then gradually released over a period of six to eight hours, contributing to the sustained warmth within the building.

The residual heat stored within the flat stones of the Tawa Khana system radiates upwards, warming the floor surfaces and subsequently the occupants of the room through thermal radiation. This passive heating system is typically operated two to three times a day, often coinciding with meal preparation times like breakfast and dinner. The height of the tunnels within the floor structure plays a crucial role in optimizing heat transfer. Studies have shown that the typical range for tunnel height in both Tawa Khana and Ondol systems falls between 0.15 and 0.4 meters. This specific height range facilitates the efficient circulation of the heated air and ensures the floor reaches a comfortable temperature for occupants. It is important to note that the optimal height may vary depending on factors such as the local climate and the specific heating system design.

Figure 2. Tawa Khana components: a) mud as a construction material, b) mud brick for tunnel construction, c) tandoor or fireplace, d) underfloor space and connector hole, e) tunnels f) network of tunnels, g) ventilation outlet.

A comprehensive survey of existing Tawa Khana systems in rural Afghanistan villages, as illustrated in Figure 2, sheds light on their construction practices. The underfloor spaces, or tunnels, are not built with a uniform height, but rather optimized for both the local climate and the specific function of the Tawa Khana within the dwelling. Notably, these tunnels are designed with a 4% incline to ensure efficient air circulation throughout the system. In some rare instances, a single, wider hypocaust tunnel can be used instead of multiple smaller tunnels, serving as the entire underfloor space. However, for larger rooms, multiple tunnels of specific widths are employed to ensure even heat distribution throughout the floor surface. Local flat stones are used to cover all the tunnels, facilitating effective heat transfer from the warm air to the floor above. These tunnels are strategically positioned beneath the room's floor and interconnected at both their entry and exit points within the designated space. On one end, the underfloor space connects to a fireplace or Tandoor through a clay pipe or dedicated tunnel for receiving heat. On the opposite side, an outlet on the wall allows for smoke to escape during operation but remains closed at other times to minimize heat loss. The design of the fireplace or Tandoor incorporates specific dimensions to enable simultaneous cooking and space heating. Constructed with special clay and precise measurements, the Tandoor typically features a bottom surface positioned 1.2 meters below the main room level. Furthermore, an exhaust system positioned 0.5 to 1.0 meters from the fireplace is incorporated into the Tandoor design to enhance its efficiency. A detailed breakdown of Tawa Khana dimensions, based on the aforementioned survey of existing structures, can be found in Table 1. The utilization of readily available materials and minimal financial investment associated with Tawa Khana construction makes it a suitable heating solution for various locations, particularly in regions with similar resource constraints.

Despite the current decline in urban application, the Tawa Khana concept presents a valuable opportunity for revitalization. Through targeted optimization of design and construction methods, these traditional heating systems can be further enhanced in terms of efficiency, paving the way for their reintroduction into contemporary building practices.

Table 1. Key dimensions of Tawa Khana elements, including heating sources (Tandoor) and underfloor spaces (Tunnels).

Tawa Khana features	Height (m)	Width (m)	Diameter (m)	Outlet diameter (m)
Tandoor or fireplace	1.2	-	1.2	0.1 – 0.15
Tunnel or hypocaust	0.4 – 0.5	0.4		0.15
Connector (Clay pipe)	-	-	0.1 – 0.2	

Therefore, this research examines the potential of Tawa Khana as a sustainable heating strategy, aiming to bridge the gap between its historical significance and its future applicability in modern building designs.

2.2. Simulation and Analysis

To effectively simulate and analyze the performance of Tawa Khana, a representative test room located within Kabul City, Afghanistan, was chosen as the primary model. Kabul, the nation's capital and most populous city, occupies the eastern region of the country at approximately 34°31′31″ North latitude and 69°10′42″ East longitude. The city encompasses 22 districts spread across a land area of 1,049 square kilometers and houses an estimated 396,095 dwelling units [14,29]. Kabul experiences a well-defined four-season climate featuring distinct dry periods. Spring encompasses the months of March, April, and May; summer spans from June to August; fall consists of September, October, and November; and winter unfolds from December to February. The overall climate of Kabul can be categorized as arid to semi-arid, with hot summers and cold winters. Winter temperatures can plummet to as low as -10°C, while summer temperatures can soar to 40°C [30,31]. The design of the test room was meticulously adjusted to conform to the established specifications for residential buildings in Kabul City, as detailed in Table 2. This ensures the model accurately reflects the typical dwelling unit where Tawa Khana would be implemented.

Table 2. Description of a test room for simulation input in the DesignBuilder program.

Test room	Description
Location	Kabul city, Afghanistan
Residential space	Living room
Ventilation type	Natural ventilation
HVAC	Cooling COP 3/ Heating COP 0.8
Heating set point	22 Co
Cooling set point	24 Co
Infiltration	Good
Room dimensions	6m x 6m = 36 m2
Room height	3 m
Window type	South-facing single window
Window to wall ratio	60 %
Glazing type	Trp Clr 3mm/13mm Arg
Wall	Outside Plaster + EPS +Brick-burned + Inside Plaster
Roof	Bitumen sheet + Cement mortar + EPS + Slap (Co-Reinforced) +Plaster
Floor	Carpet + Tiles + Mortar + Concrete + Gravel

DesignBuilder, a well-established Building Energy Modeling (BEM) tool, was chosen to simulate and analyze the performance of Tawa Khana. This software offers a comprehensive suite of functionalities for simulating various building elements during the design phase, promoting the development of energy-efficient building practices [32]. The decision to employ DesignBuilder in this study stemmed from its robust capabilities in conducting whole-building energy analyses and its ability to evaluate diverse aspects of a building's performance. Furthermore, DesignBuilder serves as a versatile platform, integrating functionalities for building performance simulation that encompass Computational Fluid Dynamics (CFD) analysis. Within DesignBuilder, CFD simulations are particularly useful for analyzing airflow patterns, temperature distribution, and contaminant transport within and surrounding buildings. This comprehensive approach to building performance simulation proved instrumental in analyzing the impact of various energy-saving strategies, particularly focusing on Tawa Khana. In this context, CFD analysis of Tawa Khana was employed to gain a deeper understanding of its airflow patterns, temperature distribution, and other critical performance metrics.

3. Results

The Tawa Khana system's performance was simulated under winter conditions at 9:00 am, representing the coldest time of day when the external temperature reaches -6°C. Previous research suggests that floor surface temperatures for radiant heating systems ideally fall within a range of 19°C to 29°C [25]. The simulation results demonstrate that the Tawa Khana system, operating at a high temperature, successfully elevated the floor surface temperature to 29°C. To ensure the accuracy of the findings, a comparative analysis was conducted. This analysis compared a baseline test room without Tawa Khana to a test room incorporating the Tawa Khana system. Detailed specifications of these test room configurations are provided in Table 3.

Table 3. Results obtained from simulating the test room with Tawa Khana and without Tawa Khana.

	Air Temperature		Surfaces Temperature						
Test room description	Outside	Inside (Room)	Floor Surface	Roof	North facing	North face Wall	East face wall	South face wall	West face wall
Baseline	-6	12.5	13.7	13	8	13	13	13	13
Tawa Khana		*16.5*	29						

The simulation results for the baseline test room, which does not incorporate a Tawa Khana system (as depicted in Figure 3), indicate a room temperature of 12.5°C. This temperature distribution is observed to be relatively uniform throughout space, with the exception of minor variations near the window. These variations likely stem from heat transfer processes occurring at the window due to its thermal properties. The simulation also revealed low airflow velocities within the baseline test room, ranging from 0 to 0.07 meters per second. This minimal air movement can be attributed to the absence of a heating system in the room.

The simulation results for the test room incorporating the Tawa Khana system (as depicted in Figure 4) reveal a significantly improved room temperature of 16.5°C. A notable difference in temperature is observed between the room air and the floor surface. The floor temperature reaches 29°C, effectively contributing to space heating through radiant heat transfer. Furthermore, the airflow patterns within the room exhibit greater variation compared to the baseline test room. Airflow velocities range from 0 to 0.22 meters per second, with noticeably higher velocities near the floor surfaces. This increased air circulation is a consequence of the Tawa Khana system's operation and contributes to improved heat distribution throughout the space.

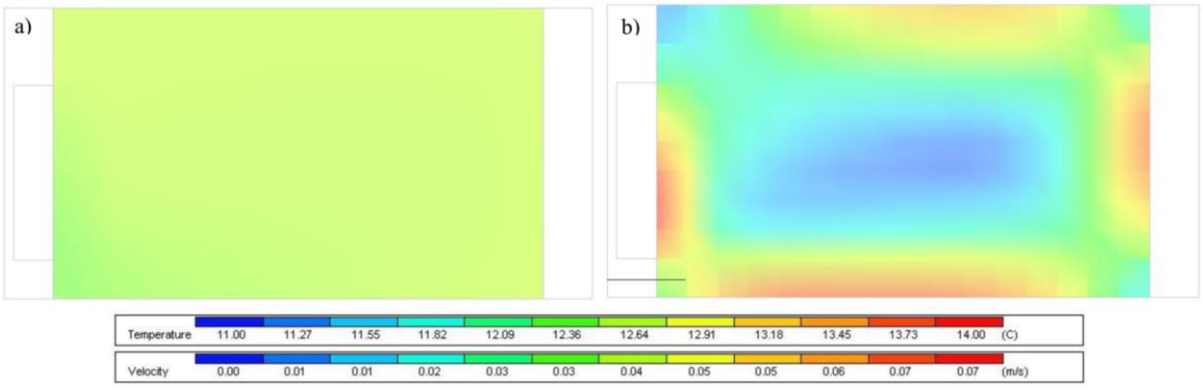

Figure 3. Temperature and airflow velocity of the test room surfaces in the absence of Tawa Khana (Baseline). a) Depiction of temperature distribution across the room section. b) Visualization of airflow velocity patterns within the room section.

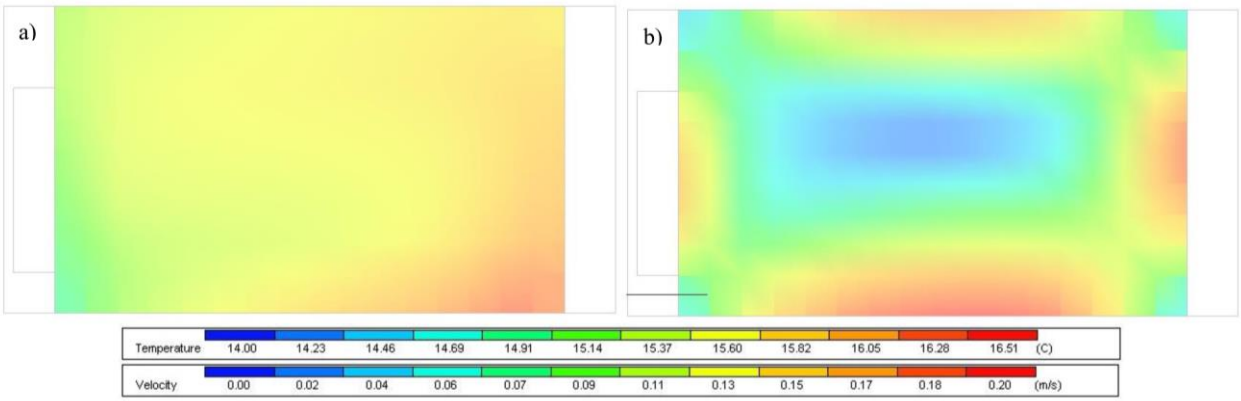

Figure 4. Temperature and airflow velocity of the test room surfaces with Tawa Khana. a) Depiction of temperature distribution across the room section. b) Visualization of airflow velocity patterns within the room section.

The simulation results demonstrate the effectiveness of Tawa Khana in achieving space heating. The floor surface temperature within the test room equipped with Tawa Khana reached 29°C, representing a significant increase of up to 16.5 degrees compared to the baseline model. This translates to a room temperature increase of approximately 4°C. This finding highlights the potential of Tawa Khana to utilize heat generated by household activities, such as cooking, for space heating purposes. By effectively capturing and distributing this waste heat, Tawa Khana offers an opportunity to conserve and utilize existing thermal energy for practical applications, potentially reducing the reliance on conventional heating systems.

4. Discussion

Vernacular architecture, encompassing the traditional building techniques and styles developed over generations by local communities, offers a rich repository of knowledge concerning energy-efficient design strategies. This body of knowledge emphasizes the importance of passive design principles, which involve the strategic design of buildings to leverage natural environmental resources for temperature regulation within the built environment. In warm climates, vernacular architecture often employs design features that promote shading and ventilation to achieve natural cooling effects. Conversely, buildings in cooler climates may incorporate design elements that facilitate solar heat gain and storage to maintain comfortable indoor temperatures. As a general principle, vernacular buildings frequently integrate features that promote the utilization of locally available and renewable energy sources, ultimately aiming to minimize reliance on non-renewable energy resources.

The Tawa Khana, a traditional Afghanistan's heating system, exemplifies the ingenuity of vernacular architecture in achieving thermal comfort. This system utilizes a network of subterranean tunnels and a central Tandoor oven to efficiently distribute heat throughout a dwelling. Notably, the construction of Tawa Khana is characterized by its relative simplicity and affordability, primarily relying on locally available materials. However, despite these advantages, the application of Tawa Khana appears to be diminishing, primarily concentrated in rural areas. This study posits that through strategic design optimization and implementation, Tawa Khana can be revitalized as a viable and energy-efficient heating solution for contemporary buildings. The inherent merits of the Tawa Khana design offer several advantages. First, its dependence on local materials minimizes construction costs, making it a particularly attractive option for communities with limited resources. Second, the network of underground tunnels effectively captures and distributes heat generated by the Tandoor, promoting efficient fuel utilization. Furthermore, the inherent thermal mass of the earthen materials used in construction contributes to a long-lasting and stable heating effect. While the Tawa Khana system boasts these strengths, its potential for efficiency can be further amplified through targeted optimizations. Modern advancements in materials and technology can be strategically applied to refine the design of the underground tunnels. These refinements could focus on optimizing heat transfer efficiency while minimizing heat loss from the system. Additionally, the incorporation of readily available insulation materials presents another avenue for enhancing the overall thermal performance of the system. Furthermore, exploring alternative fuel sources for the Tandoor oven, such as biogas or solar power, holds promise for improving the system's sustainability and overall energy efficiency. Beyond its functional merits, the Tawa Khana represents a significant element of Afghanistan cultural heritage. By revitalizing and optimizing this traditional system, a twofold benefit can be achieved. This approach not only safeguards this cultural heritage but also offers a potential solution to the contemporary challenges faced by Kabul City, particularly regarding air pollution and energy consumption during winter months. A renewed focus on the Tawa Khana system, coupled with capacity-building initiatives for local craftspeople, can ensure the continued existence of this sustainable heating solution while fostering its integration

into contemporary building practices.

5. Conclusions

Tawa Khana (Ondol) exemplifies a vernacular approach to heating that prioritizes environmental sustainability through its promotion of energy efficiency and sensitivity to site-specific factors. This radiant heating system utilizes heat generated from an underfloor furnace, fueled by various options such as wood, coal, or natural gas. A key advantage of Tawa Khana lies in its ability to efficiently capture and utilize waste heat produced during cooking activities. This reduces reliance on conventional heating systems, thereby promoting energy conservation within the dwelling. Furthermore, by directly heating the floor surface, Tawa Khana minimizes heat loss through convection and radiation mechanisms. This targeted heating approach contributes to superior energy efficiency compared to traditional heating systems that rely on air circulation for heat distribution.

The simulation results convincingly demonstrate the effectiveness of Tawa Khana in enhancing thermal comfort within space. By elevating the floor surface temperature from 13.7°C to 29°C, the system contributes to a notable increase in room temperature, rising from 12.5°C to 16.5°C. This translates to an approximate 4°C increase in room temperature, with the floor surface temperature playing a significant role in achieving occupant thermal comfort through radiant heat transfer. These findings highlight Tawa Khana's potential as a sustainable heating strategy. The system leverages locally generated heat from cooking activities to raise the room temperature effectively. The accompanying Figures 3 and 4 visually represent the distribution of thermal velocity and surface temperatures within the test room. The data suggests a clear trend of increasing temperature and air velocity emanating from the floor surface upwards through the Tawa Khana system, ultimately heating the room air. With the system typically activated two to three times a day, coinciding with meal preparation times, it is expected that continuous operation will lead to a further rise in room temperature, potentially reaching a comfortable set point of 22°C. This approach offers a promising avenue for achieving energy efficiency by addressing the building's heating demands while simultaneously ensuring the thermal comfort of its occupants.

This research underscores the potential of Tawa Khana, a traditional Afghanistan’s heating system, as a viable and sustainable strategy for achieving energy-efficient buildings. The system's reliance on fundamental technologies and readily available resources aligns well with the principles of sustainable design. However, contemporary building practices often disregard this valuable approach, jeopardizing its continued existence. This study offers a comprehensive analysis of Tawa Khana, drawing upon evaluations of existing installations and building energy simulations. Table 1 details the design principles underlying this strategy and its potential to enhance building energy efficiency. By strategically optimizing these design principles and integrating advancements in modern technology, the performance of Tawa Khana can be significantly improved. This optimization process has the potential to position Tawa Khana as a compelling alternative to conventional heating systems employed in contemporary buildings.

Declaration

The authors declared no potential conflicts of interest with respect to the research, authorship, and/or publication of this article. The authors also declared that this article is original, was prepared in accordance with international publication and research ethics, and ethical committee permission or any special permission is not required.

Author Contributions

A.W.A. conceived the overall research design and methodology, conducted formal data analysis, and drafted the initial manuscript. M.I. provided supervision, guidance, and critical review of the manuscript. A.W.A. and F.I. contributed to data collection through on-site fieldwork and photography.

Acknowledgment

This research was conducted as part of the doctoral dissertation of the first author, Ahmad Walid Ayoobi.

References

1. Ozorhon G., Ozorhon I. *Learning from Mardin and Cumalıkızık: Turkish Vernacular Architecture in the Context of Sustainability*. Arts, 2014. **3**(1): p. 175–89.
2. Ching FD., Shapiro IM. *Green building illustrated*. New Jersey: John Wiley & Sons; 2020.
3. Castellano J., Ribera A., Ciurana J. *Integrated system approach to evaluate social, environmental and economics impacts of buildings for users of housings*. Energy and Buildings, 2016. **123**: p. 106–18.
4. Arslan M., Kunt M., Yılmaz C. *Design and optimization of a computer simulation model for green hydrogen production by waste heat recovery from Afyon biogas plant*. International Advanced Researches and Engineering Journal, 2023. **7**(3): p. 157–64.
5. Shen J., Krietemeyer B., Bartosh A., Gao Z., Zhang J. *Green Design Studio: A modular-based approach for high-performance building design*. Building Simulation, 2021. **14**(2): p. 241–68.
6. Khakian R., Karimimoshaver M., Aram F., Benis SZ., Mosavi A., Varkonyi-Koczy AR. *Modeling nearly zero energy buildings for sustainable development in rural areas*. Energies, 2020. **13**(10).
7. Sameer H., Bringezu S. *Life cycle input indicators of material resource use for enhancing sustainability assessment schemes of buildings*. Journal of Building Engineering, 2019. **21**: p. 230–42.

8. Invidiata A., Lavagna M., Ghisi E. *Selecting design strategies using multi-criteria decision making to improve the sustainability of buildings*. Building and Environment, 2018. **139**: p. 58–68.
9. Saadatian O., Haw LC., Sopian K., Sulaiman MY. *Review of windcatcher technologies*. Renewable and Sustainable Energy Reviews, 2012. **16**(3): p. 1477–95.
10. Harish VSKV., Kumar A. *A review on modeling and simulation of building energy systems*. Renewable and Sustainable Energy Reviews, 2016. **56**(1): p. 1272–92.
11. Waseq WM. *The impact of air pollution on human health and Environment with mitigation Measures to reduce Air Pollution in Kabul Afghanistan*. International Journal of Healthcare Sciences, 2020. **8**(1): p. 1–12.
12. Ayoobi AW., Ahmadi H., Inceoglu M., Pekkan E. *Seasonal impacts of buildings' energy consumption on the variation and spatial distribution of air pollutant over Kabul City: application of Sentinel—5P TROPOMI products*. Air Quality, Atmosphere and Health, 2022. **15**(1): p. 73–83.
13. Mehrad AT. *Causes of air pollution in Kabul and its effects on health*. Indian Journal of Ecology, 2020. **47**(4): p. 997–1002.
14. Wafa W., Hairan MH., Waizy H. *The Impacts of Urbanization on Kabul City ' s Groundwater Quality*. International Journal of Advanced Science and Technology, 2020. **29**(4): p. 10796–809.
15. BAŞARAN A. *A study on the renewable energy potential of incineration of municipal solid wastes produced in Izmir province*. International Advanced Researches and Engineering Journal, 2022. **6**(2): p. 123–31.
16. Sonaiya OA., Dincyurek O. *Tradition and Modernism in Yoruba architecture: Bridging the Chasm*. Open House International, 2009. **34**(4): p. 74–81.
17. Miri EM. *Ecoloical Building Design: A Proof of Concept and Identifying the Factors which deter the use of Iranian Vernacular Principles in Modern architecture*. London South Bank University; 2016.
18. Algburi OHF. *An Energy Simulation Study: Reducing Cooling Energy of Residential buildings Based on Vernacular and Passive Cooling Techniques*. Gazi University; 2018.
19. Taleb HM. *Using passive cooling strategies to improve thermal performance and reduce energy consumption of residential buildings in U.A.E. buildings*. Frontiers of Architectural Research, 2014. **3**(2): p. 154–65.
20. Dabieh M. *A future for the past of spectacular desert vernacular*. Lund University; 2011.
21. Kazimee BA. *Urban/rural dwelling environments : Kabul, Afghanistan*. (Doctoral dissertation, Massachusetts Institute of Technology); 1977.
22. Kazimee BA. *Sustainable reconstruction and planning strategies for Afghan cities: Conservation in cultural and environmental heritage*. WIT Transactions on Ecology and the Environment, 2006. **93**: p. 49–59.
23. Lamantia R. *Versae : A Method For Developing Sustainable , Affordable and Energy Efficient Net-Zero Housing Linking Back to Vernacular Architecture*. University of Arizona; 2016.
24. Al-Sallal KA., Rahmani M. *Vernacular Architecture in the MENA Region: Review of Bioclimatic Strategies and Analysis of Case Studies*. In: Sustainable vernacular architecture, 2019. p. 23–53.
25. Song GS. *Buttock responses to contact with finishing materials over the ONDOL floor heating system in Korea*. Energy and Buildings, 2005. **37**(1): p. 65–75.
26. Dişli G., Özcan Z. *An evaluation of heating technology in Anatolian Seljuk period hospitals (Darüşşifa)*. Metu Journal of the Faculty of Architecture, 2016. **33**(2): p. 183–200.
27. Lee KH., Han DW., Lim HJ. *Passive design principles and techniques for folk houses in Cheju Island and Ullūng Island of Korea*. Energy and Buildings, 1996. **23**(3): p. 207–16.
28. Kazimee BA. *Sustainable reconstruction and planning strategies for Afghan cities: Conservation in cultural and environmental heritage*. WIT Transactions on Ecology and the Environment, 2006. **93**: p. 49–59.
29. UN-Habitat. *State of Afghan Cities 2015*. 2015. Available from: https://reliefweb.int/report/afghanistan/state-afghan-cities-2015-volumes-one-two
30. Qutbudin I., Shiru MS., Sharafati A., Ahmed K., Al-Ansari N., Yaseen ZM., et al. *Seasonal drought pattern changes due to climate variability: Case study in Afghanistan*. Water (Switzerland), 2019. **11**(5): p. 1096.
31. Houben G., Niard N., Tünnermeier T., Himmelsbach T. *Hydrogeology of the Kabul Basin (Afghanistan), part I: Aquifers and hydrology*. Hydrogeology Journal, 2009. **17**(3): p. 665–77.
32. DesignBuilder. *DesignBuilder 2.1 User's Manual*. 2009 [cited 2023 Sep 27]. Available from: http://www.designbuildersoftware.com/docs/designbuilder/DesignBuilder_2.1_Users-Manual_Ltr.pdf

Available online at www.dergipark.org.tr/en

INTERNATIONAL ADVANCED RESEARCHES and ENGINEERING JOURNAL

Journal homepage: www.dergipark.org.tr/en/pub/iarej

e-ISSN: 2618-575X

International Open Access

Volume 08
Issue 03

December, 2024

Research Article

Simulation of fuzzy logic and PI control methods on a bridgeless isolated SEPIC converter for electric vehicle chargers

Alperen Uğurluoğlu [a]* ***and Ahmet Karaarslan*** [a]

[a] *Ankara Yıldırım Beyazıt University, Institute of Science, Department of Electrical and Electronics, 6010, Keçiören/Ankara*

ARTICLE INFO

Article history:
Received 13 June 2024
Accepted 12 December 2024
Published 20 December 2024

Keywords:
BL SEPIC
Fuzzy controller
PFC
PI controller
THD

ABSTRACT

Studies in literature and the increasing trend of electrification show that electric vehicles (EVs) will become more widespread in the future. However, the growing demand for EV chargers causes an overload on the grid. Furthermore, EV chargers generate power factor distortion and harmonics, which contaminate the grid and lower the quality of power. Therefore, power factor correction (PFC) is applied by EV chargers to mitigate the harmonics. As defined in the IEC 61000-3-2 standard, the total harmonic distortion (THD) shall be less than 5%. In this study, a better PFC operation is achieved with the proposed bridgeless isolated single ended primary inductor converter (BL SEPIC) topology as an EV charger instead of conventional converter topologies that have diode bridge rectifiers (DBR). Also, the study has better THD outputs as compared with the similar bridgeless (BL) topologies in literature thanks to the simulated control methods of the proportion-integration (PI) and fuzzy control. Moreover, these control methods are compared with each other in terms of THD suppression performance, stability, robustness, and computational effort. The results showed that the fuzzy controller has advantages of stability and robustness against the transient conditions, input voltages and load changes for THD suppression while the PI controller has better THD results only for steady state operation with nominal input voltage and full load conditions. The implemented PI and fuzzy controllers are simulated in a MATLAB Simulink environment.

1. Introduction

Nowadays, the increasing amount of greenhouse gas emissions leads people to seek out greener fuels, such as electricity, instead of fossil fuels. Thus, electric vehicles have started to be popular instead of internal combustion engines. [1] Thanks to battery energy storage (BES) systems, it is possible to store electrical energy in transport vehicles. [2] However, BES systems require EV battery charging units, whether on-board or off-board. [3] Moreover, the increasing number of EV chargers burdens the power grid. Therefore, the grid power quality drops since the EV chargers produce harmonics and have a poor power factor. Hence, the EV charging system shall be designed to produce a high-power factor and low harmonics and provide clean power utilization when it is connected to the grid. [4-7]

The input power quality (PQ) indices shall be maintained by the charger in accordance with the IEC 61000-3-2:2018 standard. [8-9] Nevertheless, traditional EV battery chargers use a filtered output from a diode bridge rectifier (DBR), which produces harmonics, to draw power from an alternative current (AC) supply. [10-11] According to the reviews in the literature, the THD produced by the converters that use DBR is in the range of 15% to 80%. [12] The buck and boost topologies that use DBR are the most preferable solutions for low power applications due to low-cost effectiveness and simplicity. [13-14, 28] However, they have poor PFC operation and high conduction losses for high power applications because of the poor controller algorithm and the number of components in the circuitry. In contrast, the buck-boost topologies have better PFC operation since they have both step-up and step-down features to control the output, but these topologies are not sufficient to fully suppress the harmonics as well. [15]

Several other PFC topologies in the literature utilize DBR structures such as CUK, zeta and SEPIC converters. [16] These topologies have better PFC operation as compared with buck boost topologies, and their structure allows to reduce ripples. On the other hand, the size of these circuits is bulkier, especially in CUK and zeta converters due to the

* Corresponding author. Tel.: *+90-554-983-0402*.
E-mail addresses: alperen.ugurluoglu@gmail.com *(Alperen UĞURLUOĞLU)*, akaraarslan@gmail.com *(Ahmet KARAARSLAN)*
ORCID: 0000-0001-8038-5729 *(Alperen UĞURLUOĞLU)*, 0000-0001-6475-4539 *(Ahmet KARAARSLAN)*
DOI: 10.35860/iarej.1501059

extra filtering stage and the need for high voltage DC link capacitors. [17] Also, the current and voltage stresses are high due to their single stage and non-interleaved structures, especially for the SEPIC converter. [18] Beside that, the full bridge and inductor-inductor-capacitor (LLC) converter topologies in the literature are preferable due to their high-power density, high efficiency and low electromagnetic interference (EMI). [19-21] However, the cost effectiveness of these topologies is very low, and these topologies offer complex control systems for PFC operation. In addition, the LLC topologies are used with DBR or other PFC converters. If the DBR structure is used, the LLC topology becomes simpler and smaller in size, but the power loss increases. If another PFC converter is used, the power loss drops remarkably, but the cost and size also increase. [22]

On the other hand, high harmonic suppression, low EMI and better PFC operation can be achieved by interleaved AC to direct current (DC) PFC converter topologies such as boost, SEPIC and flyback. [22-23] In addition, the losses and heating problems are reduced since each switching component handles only the half cycle of the ac mains. However, the reduction of losses, heat problems and THD is limited due to the existence of DBR in the topologies.

In literature, interleaved converters without DBR are found such as isolated interleaved Luo and SEPIC converters. [16] The synchronous rectifier and interleaved structure provide lower voltage and current stresses with high efficiency. In addition, higher PFC performance, low THD and unity PF are obtained without any extra filtering circuit. However, the component and switching element counts require complex control methods and cause large size. In literature, several topologies with reduced component count are found. [24] These topologies have features of less component count, simpler control with high efficiency and low THD. The BL SEPIC topologies among these converters are found to be a good solution due to their lower component count, simple control, high efficiency and low THD performance. [27,38]

Furthermore, the controller methods of EV chargers are investigated to provide better PFC operation to suppress the THD that reduces the power quality of the grid, as given in Figure 1. [28-30] It is seen that there are two groups of control methods, which are linear and non-linear methods. The linear methods of PI and proportion-integration-derivation (PID) controllers are the widely used and conventional methods in literature due to their simplicity and applicability. [31-32] On the other hand, the tuning process of these linear controllers requires difficult techniques such as assumption based algorithms, mathematical model calculations or intelligent tuning algorithms. The Ziegler-Nichols method, state space modeling, genetic algorithm or neural network algorithms are several techniques for tuning a linear controller. [29, 33-34] In addition, the linear controllers have deficiencies while controlling the converters in different working conditions such as transient operations, different input voltage levels and output load changes. The stability and robustness of the linear controllers decrease as getting away from the tuned region. At that point, the non-linear control methods have better performance for changing conditions such as sliding mode, model predictive and fuzzy logic controllers. [35] However, sliding mode and model predictive control methods still require mathematical models of the controlled topology, whereas the fuzzy logic controller provides a linguistic base control method while the non-linear feature is preserved. [36-37]

In this study, a BL SEPIC converter is proposed for better PFC operation and lower THD performance. [38] The proposed converter is controlled with PI and fuzzy controllers to compare their PFC operation and THD mitigation performance. The low THD performance is achieved excellently with both linear PI control and the nonlinear method of fuzzy control. [39] Even if the PI controller has better performance for its tuned steady state operation of nominal input voltage and full load condition, the fuzzy controller shows better PFC operation when transient operations, input voltage and output load changes are simulated. Therefore, the fuzzy controller has better stability and robustness for a wide operating condition such as input voltage swings and output load changes. By using MATLAB Simulink, controller systems are implemented and simulated on the BL SEPIC converter.

The theoretical calculations and the operating principle are described in part 2. In part 3, the transient and steady state operations of the BL SEPIC are observed using the PI and fuzzy controller.

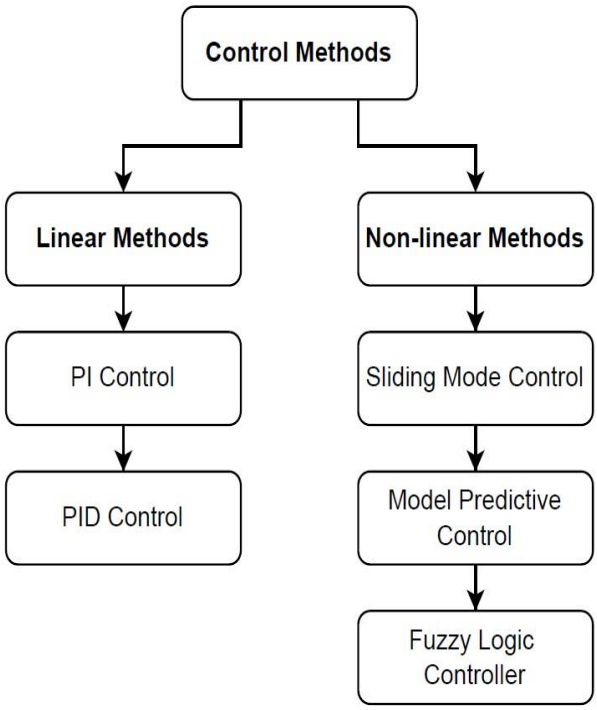

Figure 1. Classification of control methods

In addition, the BL SEPIC topology is also simulated with cases of input voltage and output load fluctuations to obtain the transient performance of the PI and fuzzy controllers. The input voltage fluctuation range is determined as 230±10% V_{rms} according to the standard of IEC 60038:2009 [40]. The operating principle of the PI controller is detailed, and the simulation results are shown in part 3.1. On the other hand, the operating principle and the simulation results of the fuzzy controller are described in part 3.2. The summary of this paper are given in the conclusion chapter.

2. Proposed Topology

The proposed topology is shown in Figure 2. The BL SEPIC topology includes two individual isolated SEPIC topologies. One of them regulates the positive half cycles of the AC input voltage, and the other regulates the negative half cycles. The average of one period of the positive or negative cycle of input voltage, V_{inav}, is obtained with Equation (1). Then, the dc output voltage, V_{dc}, is obtained with Equation (2).

$$V_{inav} = \frac{2\sqrt{2} * V_{in}}{\pi} \quad (1)$$

$$V_{dc} = \frac{n * V_{inav} * D}{(1-D)} \quad (2)$$

The BL SEPIC converter has two transformers (L_{m1}, L_{m2} = 155 µH, also with turns ratio $n = N_2/N_1$ = 1.305) and one inductor (L_i = 630 µH) for isolated energy transfer and storing energy, respectively. The magnetizing inductor values of the transformers, $L_{m1,2}$,are obtained with Equation (3). The input inductor, L_i, is calculated with Equation (4).

$$L_i = \frac{V_{in} * D}{2 * I_{in} * f} \quad (3)$$

$$L_{m1,2} = \left(\frac{N_1}{N_2}\right)^2 * \frac{V_{dc} * (1-D)^2}{2 * D * f_s * I_{dc}} \quad (4)$$

There are four switching elements (S_1, S_2, D_1 and D_2) to modulate the passive elements. Also, three capacitors (C_1, C_2 = 1 µF, C_{dc} = 5.8 mF) and a resistive load (R_{dc} = 5.6 Ω) are used in the BL SEPIC topology as passive elements. The primary capacitors, $C_{1,2}$, are calculated with Equation (5), while the output capacitor, C_{dc}, is calculated with Equation (6).

$$C_{1,2} = \frac{N_2 * V_{dc} * D}{N_1 * (\Delta V_{c1,2} * f_s * R_{dc})} \quad (5)$$

$$C_{dc} = \frac{I_{dc}}{2 * \omega * \Delta V_{dc}} \quad (6)$$

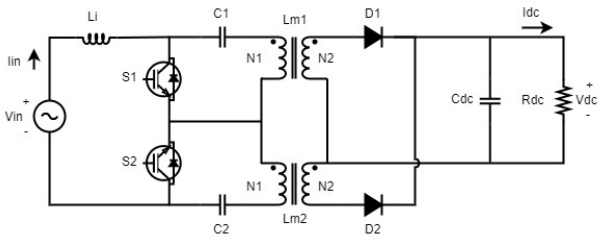

Figure 2. Proposed BL SEPIC topology

The converter is designed for 760 W output at 65 V_{dc} and 220 V_{rms} input voltage, while switching frequency is 50 kHz.

2.1. Operation Principle

Positive Half Cycle Operation:

The S_1 switch is initiated in the on state when the BL SEPIC is in the positive half-cycle of the AC supply. The L_i inductor and the transformer are charged in this state, while the output is fed by the C_{dc} Capacitor. Then, the BL SEPIC topology switches to the off state by turning off the S_1. The L_i inductor and the transformer are discharged in this state to feed the output. The on and off cycles are shown in Figure 3 (a) and Figure 3 (b), respectively.

Negative Half Cycle Operation:

The S_2 switch is initiated in the on state when the BL SEPIC is in the negative half-cycle of the AC supply. The L_i inductor and the transformer are charged in this state, while the output is fed by the C_{dc} Capacitor. Then, the BL SEPIC is altered from an on state to an off state by turning off the S_2. The L_i inductor and the transformer are discharged in this state to feed the output. The on and off cycles are shown in Figure 4 (a) and Figure 4 (b), respectively.

3. Results

BL SEPIC is set up in the Simulink environment. The passive components are adjusted to pre-calculated values. The THD of the input current is calculated with the help of the MATLAB Simulink fast fourier transform (FFT) analysis tool, which is based on Equation (7) for THD calculations. [41]

$$THD = \frac{\sqrt{\sum_{n=2}^{\infty}(I_n)^2}}{I_{fundamental}} \quad (7)$$

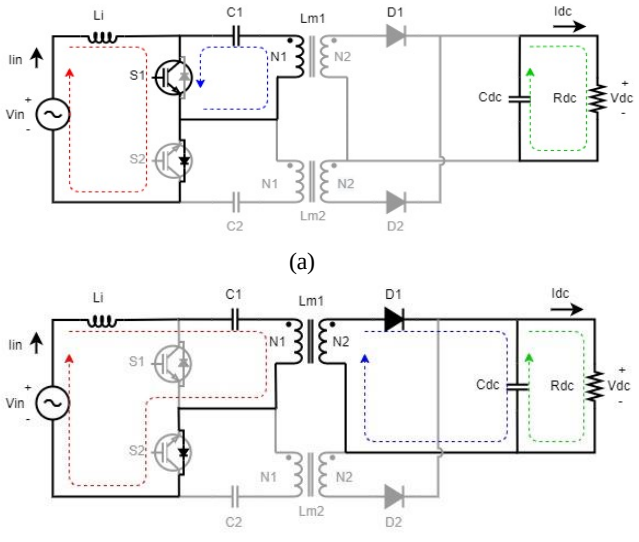

(a)

(b)

Figure 3. Positive half cycle operating states of BL SEPIC a) S1 switch is turned-on b) S1 switch is turned-off

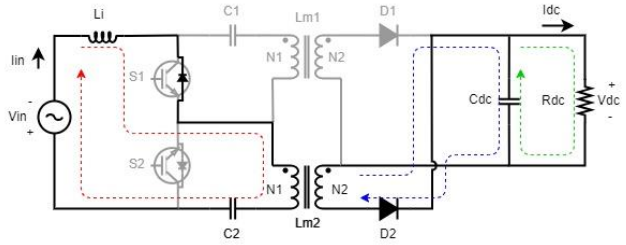

(a)

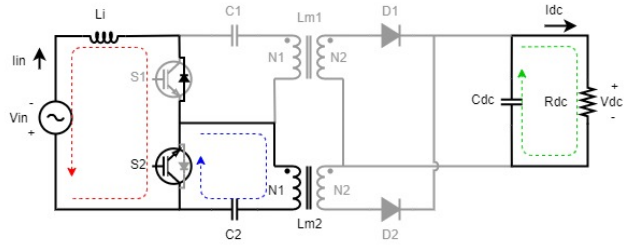

(b)

Figure 4. Negative half cycle operating states of BL SEPIC a) S2 switch is turned-on b) S2 switch is turned-off

3.1. PI Controller Method

The PI controller employs an error input and outputs a duty value. A proportional constant (K_p) is used to multiply the error, and a constant is used to integrate the error (K_i). The sum of multiplication and integration results is the duty output as seen in Equation (8). [43]

$$G_{pi} = K_p + \frac{K_i}{s} = \frac{K_p * s + K_i}{s} \tag{8}$$

As shown in Figure 5, the implemented PI controller block has one PWM output and three inputs: output voltage, V_{ofb}, input voltage, V_{infb}, and input current, I_{fb}. The PWM output of the controller drives two insulated gate bipolar transistor (IGBT) switches. Initially, a DC voltage error, V_{dce}, is calculated by comparing V_{ofb} to the reference output voltage, V_{oref}. The PI voltage controller amplifies the error to obtain the reference input current magnitude, I_{inref}. In the event of an overshoot case at the output, the PI voltage controller has a reset function to suppress the overshoots. The PI controller cannot react to instant load changes due to its integral coefficient. Therefore, the reset function provides a rapid decrease in the PI controller output. Thus, the overshoot is suppressed.

To synchronize I_{inref} with the grid voltage frequency, V_{infb} is filtered through a phase locked loop (PLL) block to have a grid frequency. In the next step, I_{fb} is compared with I_{inref} to get the current error, I_{inerr}. A duty magnitude is calculated from the I_{inerr} by using a PI current controller to produce a PWM signal by comparing it with a 50 kHz sawtooth signal.

The K_p and K_i parameters of both PI controllers need to be properly tuned for steady operation of the BL SEPIC. Therefore, the mathematical model of the BL SEPIC is obtained to find the proper PI controller parameters by applying the studies in the literature [33-34, 42]. Then, a transfer function (TF) is calculated and used for tuning the parameters.

On state equations:

$$\frac{dI_{L1}}{dt} = \frac{1}{L1}(V_{in}) \tag{9}$$

$$\frac{dV_{C1}}{dt} = \frac{1}{C1} * (-I_{Lm}) \tag{10}$$

$$\frac{dI_{Lm}}{dt} = \frac{1}{Lm}(V_{C1}) \tag{11}$$

$$\frac{dV_{Co}}{dt} = \frac{1}{Co}\left(-\frac{V_{Co}}{R}\right) \tag{12}$$

Off state equations:

$$\frac{dI_{L1}}{dt} = \frac{1}{L1}\left(V_{in} + \frac{V_{Co}}{n} - V_{C1}\right) \tag{13}$$

$$\frac{dV_{C1}}{dt} = \frac{1}{C1} * (I_{L1}) \tag{14}$$

$$\frac{dI_{Lm}}{dt} = \frac{1}{Lm}\left(-\frac{V_{Co}}{n}\right) \tag{15}$$

$$\frac{dV_{Co}}{dt} = \frac{1}{Co}\left(\frac{I_{L1} + I_{Lm}}{n} - \frac{V_{Co}}{R}\right) \tag{16}$$

At the start, only the positive half cycle operation is considered for transfer function calculation since the negative side has similar behavior. The transfer function is obtained by calculating the state space and output equations. The state space and output equations are obtained from the on state and off state equations given above. Then, these equations are represented in a matrix form. The state space equations are given in equations (18) and (20). The output equations are equal and given in equations (22).

$$x^* = A_1 * x + B_1 * u \tag{17}$$

$$\begin{bmatrix} I_{L1}^* \\ V_{C1}^* \\ I_{Lm}^* \\ V_{Co}^* \end{bmatrix} = \begin{bmatrix} 0 & 0 & 0 & 0 \\ 0 & 0 & -\frac{1}{C1} & 0 \\ 0 & \frac{1}{Lm} & 0 & 0 \\ 0 & 0 & 0 & -\frac{1}{RCo} \end{bmatrix} * \begin{bmatrix} I_{L1} \\ V_{C1} \\ I_{Lm} \\ V_{Co} \end{bmatrix} + \begin{bmatrix} \frac{1}{L1} \\ 0 \\ 0 \\ 0 \end{bmatrix} * V_{in} \tag{18}$$

$$x^* = A_2 * x + B_2 * u \tag{19}$$

$$\begin{bmatrix} I_{L1}^* \\ V_{C1}^* \\ I_{Lm}^* \\ V_{Co}^* \end{bmatrix} = \begin{bmatrix} 0 & -\frac{1}{L1} & 0 & \frac{1}{nL1} \\ \frac{1}{C1} & 0 & 0 & 0 \\ 0 & 0 & 0 & -\frac{1}{nLm} \\ \frac{1}{nCo} & 0 & \frac{1}{nCo} & -\frac{1}{RCo} \end{bmatrix} * \begin{bmatrix} I_{L1} \\ V_{C1} \\ I_{Lm} \\ V_{Co} \end{bmatrix} + \begin{bmatrix} \frac{1}{L1} \\ 0 \\ 0 \\ 0 \end{bmatrix} * V_{in} \tag{20}$$

The calculated output equations for both on and off states are equal.

$$y = C_1 * x + D_1 * u = C_2 * x + D_2 * u \tag{21}$$

$$\begin{bmatrix} Vo \\ Io \\ Iin \end{bmatrix} = \begin{bmatrix} 0 & 0 & 0 & 1 \\ 0 & 0 & 0 & \frac{1}{R} \\ 1 & 0 & 0 & 0 \end{bmatrix} * \begin{bmatrix} I_{L1} \\ V_{C1} \\ I_{Lm} \\ V_{Co} \end{bmatrix} + [0] * V_{in} \tag{22}$$

These matrix representations are used to obtain an average matrix model that also represents the large signal model of BL SEPIC. The average model is calculated with the equations from (23) to (26), and the calculated matrix forms are written in equation (27) and (28) format.

$$\mathrm{A} = [A_1 * (d) + A_2 * (1 - d)] \tag{23}$$

$$B = [B_1 * (d) + B_2 * (1-d)] \quad (24)$$

$$C = [C_1 * (d) + C_2 * (1-d)] \quad (25)$$

$$D = [D_1 * (d) + D_2 * (1-d)] \quad (26)$$

Moreover, the small signal model is obtained by applying the equation (27) and (28). The final model is used to calculate the transfer function of the BL SEPIC.

The small signal state space equation is given below.

$$\dot{\hat{x}} = A * \hat{x} + B * \hat{u} + [(A_1 - A_2)(X) + (B_1 - B_2)(U)] * (\hat{d}) \quad (27)$$

The small signal output equation is given below.

$$\hat{y} = C * \hat{x} \quad (28)$$

The final mathematical state space model of the system is given below. The obtained small signal model contains passive component equations and also input parameters of $\hat{v}_{in}$ and $\hat{d}$.

$$\begin{bmatrix} \dot{\hat{\imath}}_{L1} \\ \dot{\hat{v}}_{C1} \\ \dot{\hat{\imath}}_{Lm} \\ \dot{\hat{v}}_{Co} \end{bmatrix} = \begin{bmatrix} 0 & \frac{D-1}{L_1} & 0 & \frac{D-1}{nL_1} \\ \frac{1-D}{C_1} & 0 & \frac{-D}{C_1} & 0 \\ 0 & \frac{D}{L_m} & 0 & \frac{D-1}{nL_m} \\ \frac{1-D}{nC_o} & 0 & \frac{1-D}{nC_o} & -\frac{1}{RC_o} \end{bmatrix} \begin{bmatrix} \hat{\imath}_{L1} \\ \hat{v}_{C1} \\ \hat{\imath}_{Lm} \\ \hat{v}_{Co} \end{bmatrix} + \begin{bmatrix} \frac{1}{L_1} \\ 0 \\ 0 \\ 0 \end{bmatrix} \hat{v}_{in} + \begin{bmatrix} \frac{nV_{C1}-V_{Co}}{nL_1} \\ \frac{-I_{L1}-I_{Lm}}{C_1} \\ \frac{nV_{C1}+V_{Co}}{nL_m} \\ \frac{-I_{L1}-I_{Lm}}{nC_o} \end{bmatrix} \hat{d} \quad (29)$$

The mathematical output model of the system is given below. The output model contains Vo, Io and Iin parameters.

$$\begin{bmatrix} Vo \\ Io \\ Iin \end{bmatrix} = \begin{bmatrix} 0 & 0 & 0 & 1 \\ 0 & 0 & 0 & \frac{1}{R} \\ 1 & 0 & 0 & 0 \end{bmatrix} * \begin{bmatrix} I_{L1} \\ V_{C1} \\ I_{Lm} \\ V_{Co} \end{bmatrix} + [0] * V_{in} \quad (30)$$

The equations below are used to calculate the TF of the BL SEPIC PI controllers. Then, the MATLAB Sisotool application is used to obtain PI parameters.

$$G_{vod} = \frac{\widehat{v_o}}{\hat{d}} = C * [s * I - A]^{-1} * [B] = \frac{-3.859e8 * s^2 + 5.503e11 * s - 1.183e17}{s^4 + 96.62 * s^3 + 7.909e7 * s^2 + 7.381e9 * s + 6.11e14} \quad (31)$$

$$G_{iind} = \frac{\widehat{i_{in}}}{\hat{d}} = C * [s * I - A]^{-1} * [B] = \frac{4.787e5 * s^3 + 8.314e8 * s^2 - 8.939e13 * s - 5.788e15}{s^4 + 96.62 * s^3 + 7.909e7 * s^2 + 7.381e9 * s + 6.11e14} \quad (32)$$

The voltage and the input current PI controllers are tuned with the parameters given in Table 1.

Table 1. PI control parameters

Voltage Controller		Input Current Controller	
K_p	K_i	K_p	K_i
4.7118e-05	1.49269824	1.1093	6.26359234

As shown in Figure 6 (a) and Figure 6 (b), the rms of the AC input voltage is 230 V_{rms} and the output voltage, V_o, is 65 V. The peak of the AC input current is 5 A. The THD level is 1.08%, as is depicted in Figure 7, so the input current is nearly a pure sine wave. Also, the full load current of 12 A is set on the output.

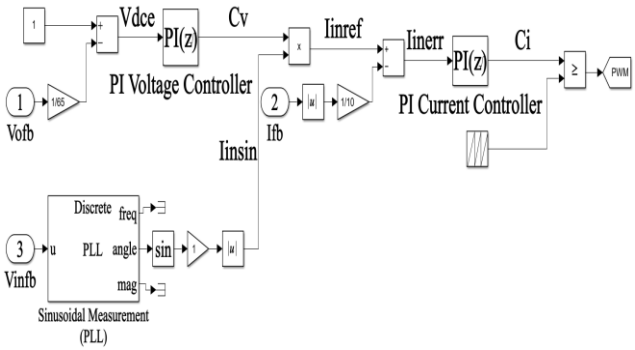

Figure 5. PI controller of the proposed study

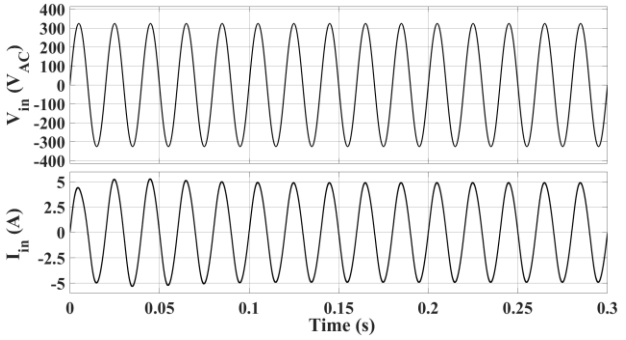

(a)

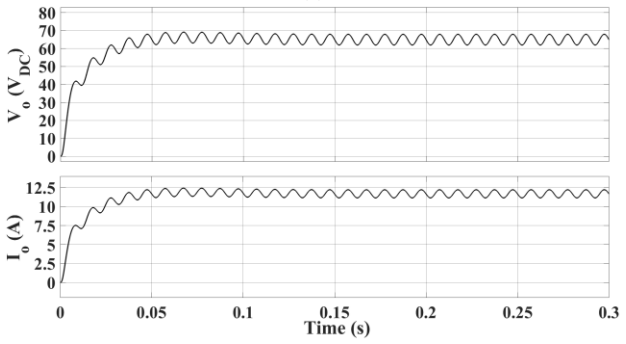

(b)

Figure 6. a) Steady state input voltage and current of PI controlled BL SEPIC, b) Steady state output voltage and current of PI controlled BL SEPIC.

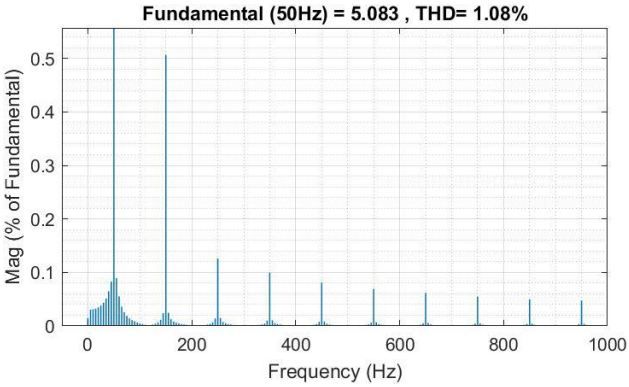

Figure 7. THD result of PI controller for a steady state operation

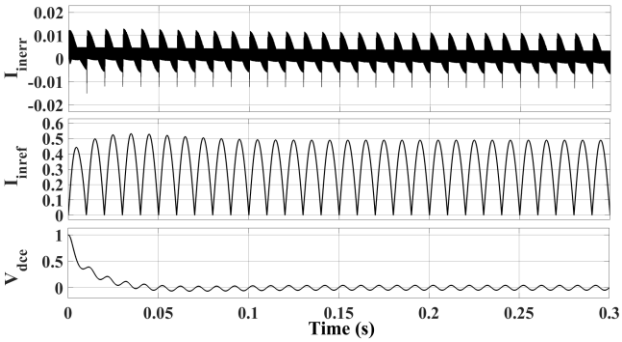

Figure 8. Current error, current reference, and voltage error signals of PI controller.

The PI controller signals are observed to understand the controller operation, as seen in Figure 8. The V_{dce} settled around zero by starting from one in 38 milliseconds. The rectified I_{inref} is obtained with a peak unit of 0.5 that corresponds to 5 A current at the input. In addition, the rectification is applied to I_{inref} because of the positive duty ratio. On the other hand, the deviation of the input current error, I_{inerr}, from zero is observed. The deviation is captured as 0 ± 0.015A. The obtained deviation also shows the magnitude of the harmonics.

The PI controller is simulated for both the input voltage and output load fluctuation cases. As shown in Figure 9, the input voltage fluctuation case is simulated within the previously established range, which is the maximum voltage of 253 V_{rms}, the minimum voltage of 207 V_{rms} and the nominal voltage of 230 V_{rms}, respectively. After the input voltage fluctuation range is applied to the BL SEPIC converter, the change in input current is observed as 4.5 A, 5.5 A and 5 A, respectively. As depicted in Figure 9 (b), the full load operation is applied at the output, and a steady state current of 12 A is obtained. At the instantaneous changes in input voltage, a drop of 11 A and a rise of 12.5 A are observed in the output current. On the other hand, the output voltage drops to 60 V_{dc} and increases up to 70 V_{dc}. In addition, it is seen that the output reaches the steady state within 50 milliseconds after each change, and any overshoot case is not observed by the PI voltage controller, therefore, the reset function is inactive.

The THD level of the PI controller is 1.98% when the input voltage is the maximum of 253 V_{rms}, as seen in Figure 10 (a). Also, the THD is 1.64% for the minimum of 207 V_{rms}, as seen in Figure 10 (b). As a result, the input voltage fluctuations are suppressed by the PI controller, and the THD is within the limits that are specified in the standard.

The output load fluctuation case is simulated for the PI controller, as shown in Figure 11. At the output voltage of 65 V_{dc}, the full load of 12 A, the quarter load of 3 A, and the half load of 6 A are applied, respectively. The rapid transition from the full load to the quarter load results in an overshoot at the output. After the predefined 72 V_{dc} overshoot level is exceeded, the reset feature of the PI voltage controller is triggered by the resultant overshoot, and the I_{inref} output is dropped to its initial state. Thus, the overshoot is suppressed, and the output reaches its steady state. Finally, the half load of 6 A is applied to the PI controller. As shown in Figure 11 (b), a drop of 60 V_{dc} at the output voltage is observed for less than 50 milliseconds, then reaches its steady state.

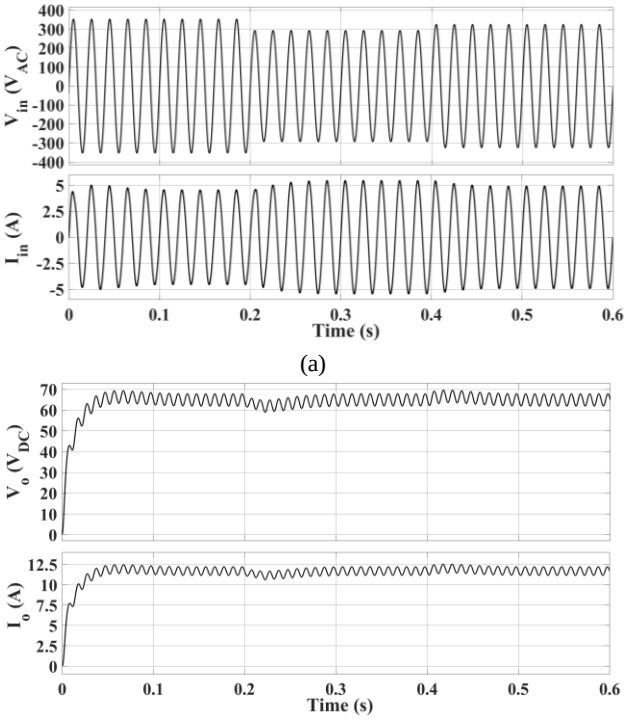

Figure 9. The input voltage fluctuation is applied to PI, a) Input voltage and current, b) Output voltage and current

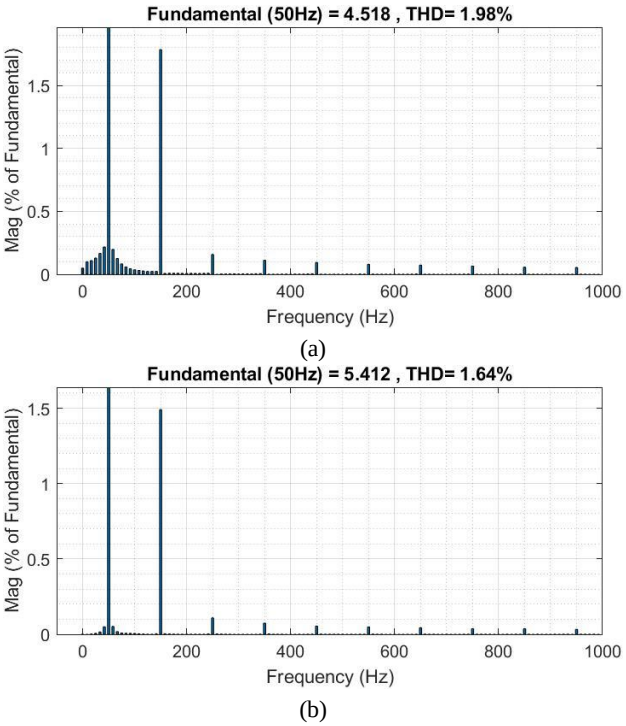

Figure 10. a) Transient THD when the input voltage is 253 V_{rms}, b) Transient THD when the input voltage is 207 V_{rms}

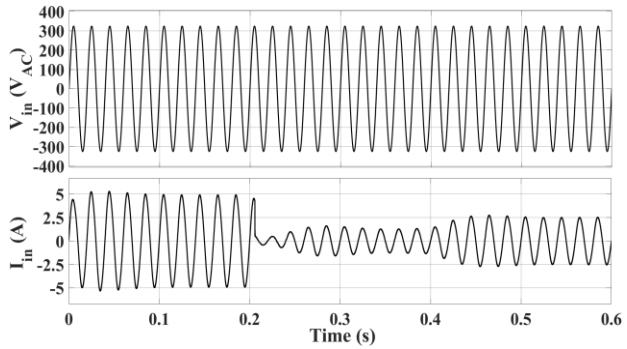

(a)

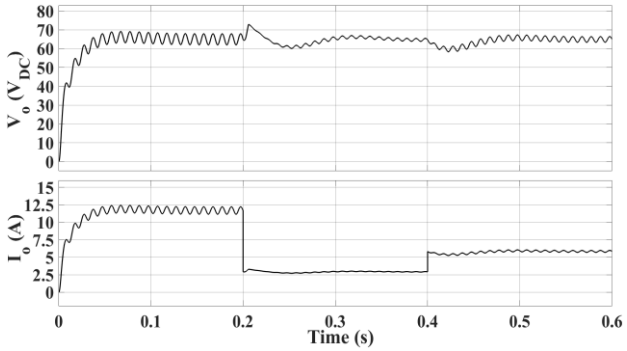

(b)

Figure 11. a) Input voltage and current results of PI controller when the output load fluctuation is applied, b) Output voltage and current results of PI controller when the output load fluctuation is applied

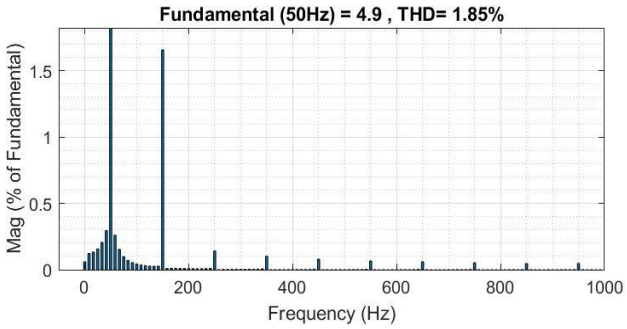

(a)

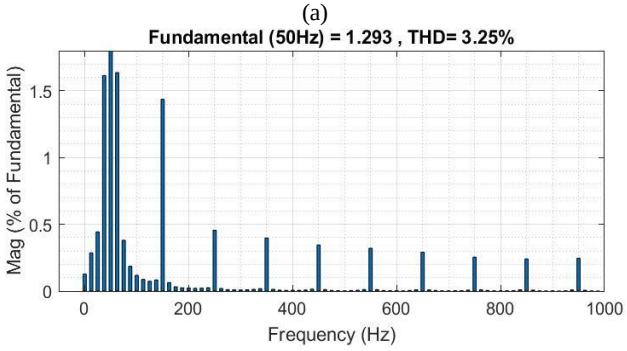

(b)

Figure 12. a) Transient THD result of PI controller at full load, b) Transient THD result of PI controller at quarter load

The THD results of the PI controller are given in Figure 12 (a) and Figure 12 (b). The full load application provides the minimum THD of 1.85%, while the quarter load application provides the maximum THD of 3.25%. As a result, the THD level is again compliant with the standard.

3.2. Fuzzy Controller Method

In the fuzzy controller, the input current PI controller is replaced with a fuzzy controller while the output voltage PI controller is the same, as shown in Figure 13. Since the fuzzy controller is based on linguistic qualifiers and has no system model, the studies in the literature are taken as initial references to define input and output membership (MS) functions. [36-37] Upon this, the input and output MS functions are tuned to get the optimal performance. Thus, each fuzzy controller input MS is defined on an error range in between -0.1 and 0.1 to make the system react faster to error changes, as shown in Figure 14. [44-45] Also, each output MS is defined over a duty output value range in between 0 and 1 to limit the duty output, as shown in Figure 15. The purpose is to set a proper duty output by relating the input and output MS functions to each other. Therefore, a rule table is assigned, and related memberships are given in Table 2. On the other hand, the defined input and output MS functions are adjusted with the system parameters, as shown in Table 2.

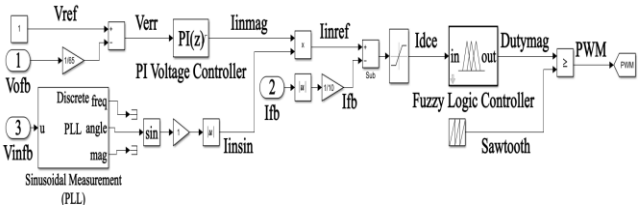

Figure 13. Fuzzy controller of proposed topology

Table 2. Rules table of fuzzy logic

Rules Table	
Input MS	Output MS
3L_N	3L
2L_N	2L
L_N	L
M	M
H_P	H
2H_P	2H
3H_P	3H

Table 3. Membership parameters of fuzzy logic

Fuzzy Membership Parameters			
Input MS		Output MS	
3L_N	[-0.16 -0.14 -0.015 0]	3L	[0 0.01 0.025]
2L_N	[-0.04 -0.005 0]	2L	[0.01 0.03 0.045]
L_N	[-0.015 -0.002 0]	L	[0.02 0.05 0.06]
M	[0 0.002 0.015]	M	[0.27 0.3 0.33]
H_P	[0 0.002 0.015]	H	[0.88 0.9 0.98]
2H_P	[0 0.005 0.04]	2H	[0.917 0.942 0.99]
3H_P	[0 0.02 0.17 0.19]	3H	[0.917 0.942 0.99]

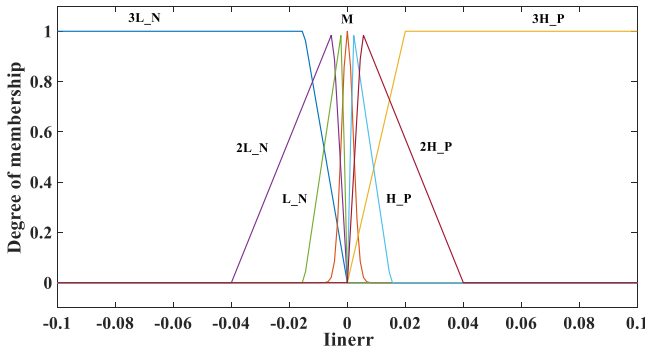

Figure 14. Input memberships of fuzzy controller

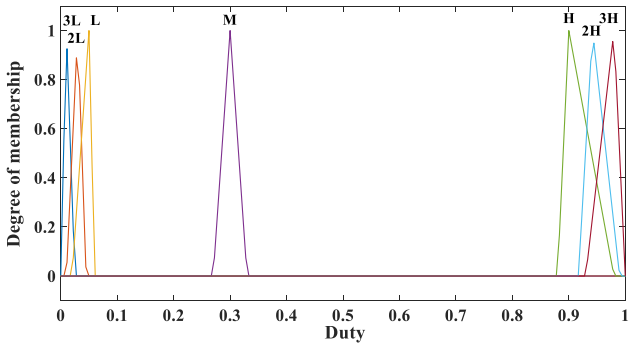

Figure 15. Output memberships of fuzzy controller

As shown in Figure 16 (a) and Figure 16 (b), The peak of the AC input voltage is 230 V_{rms}, and the output voltage, V_o, is 65 V. The peak of the AC input current is 5 A. The THD level is 1.33%, as depicted in Figure 17, so the input current is nearly a pure sine wave.

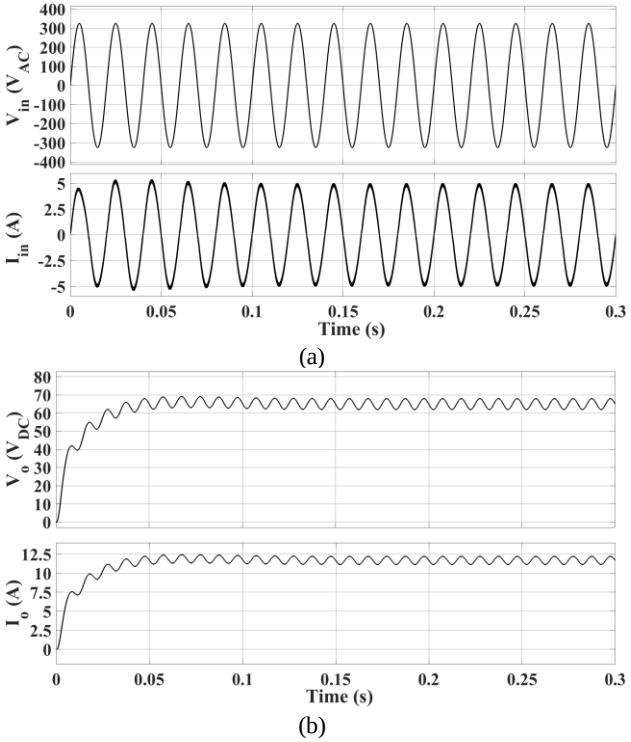

(a)

(b)

Figure 16. a) Steady state input voltage and current results of the fuzzy controlled topology, b) Steady state output voltage and current results of the fuzzy controller

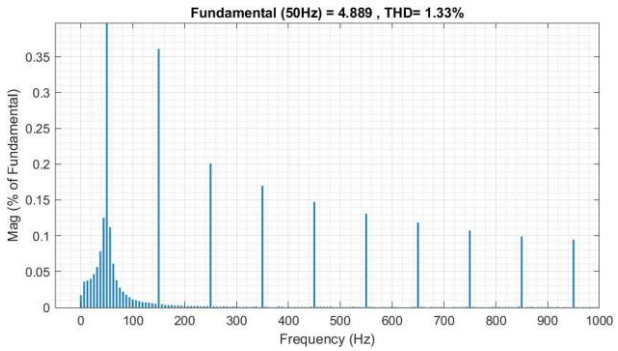

Figure 17. THD result of fuzzy method for a steady state operation

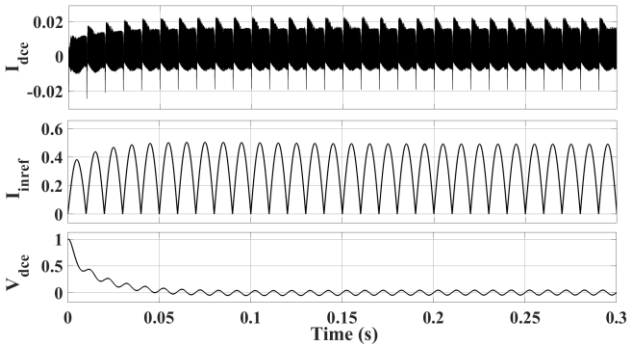

Figure 18. I_{dce}, I_{inref}, and V_{dce} signals of fuzzy controller.

The input current error, I_{dce}, the input reference current, I_{inref}, and the DC voltage error, V_{dce}, signals of the fuzzy controller are obtained, as shown in Figure 18. The V_{dce} reaches to steady state in 37 milliseconds. The I_{inref} signal is obtained with a peak of 0.5. The deviation of the I_{dce} signal is captured as 0 ± 0.02 A.

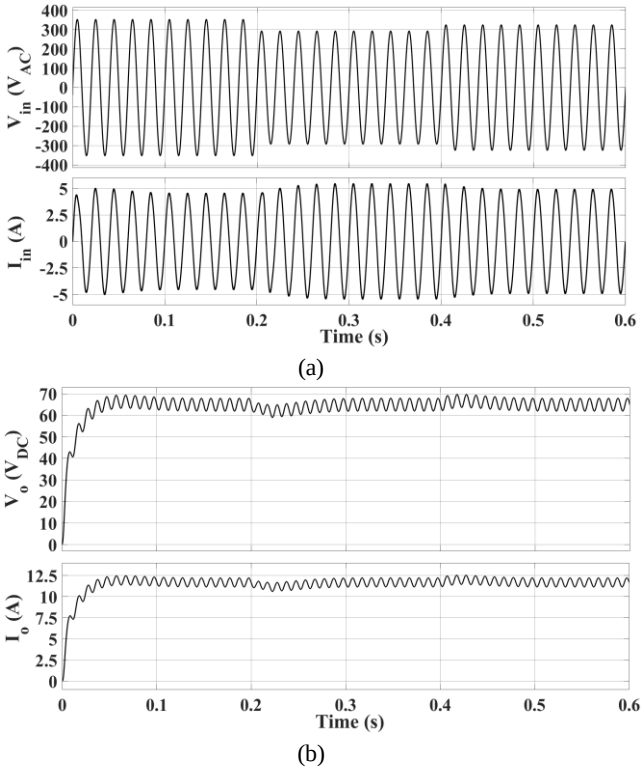

(a)

(b)

Figure 19. The input voltage fluctuation is applied to fuzzy, a) Input voltage and current, b) Output voltage and current

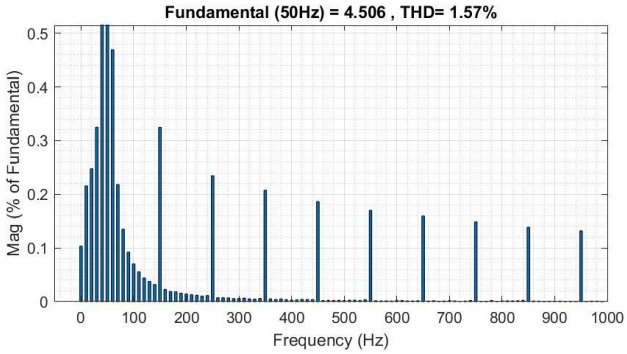

(a)

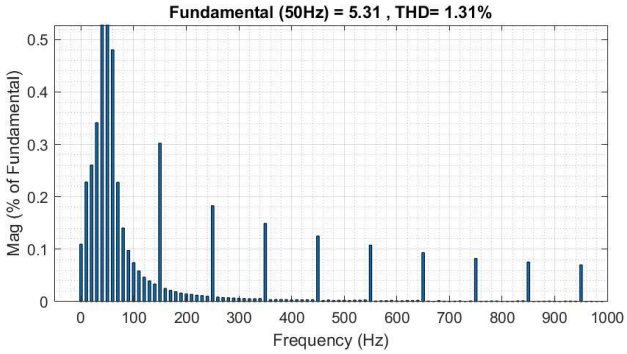

(b)

Figure 20. a) Transient THD when the input voltage is 253 V_{rms}, b) Transient THD when the input voltage is 207 V_{rms}

The fuzzy controller is also simulated for both the input voltage and output load fluctuation cases. The previously established range of input voltage fluctuation, which is in order of the maximum voltage of 253 V_{rms}, the minimum voltage of 207 V_{rms} and the nominal voltage of 230 V_{rms}, is implemented at the input of the BL SEPIC. The input current change is kept within the range of 5 ± 0.5 A by the fuzzy controller after the input voltage fluctuation range is applied. The full load of 12A is simulated at the output current. The output current fluctuation is observed in the range of 12 ± 1 A at the instant input voltage changes occurred. Furthermore, the output voltage is in the range of 65 ± 5 V, and the fluctuation at the output lasts less than 50 milliseconds. On the other hand, the reset function is inactive because no overshoot case is not observed by the PI voltage controller.

According to the input voltage fluctuation graphs, the maximum THD level of the fuzzy controller is 1.57 % when the input voltage is 253 V_{rms}. Also, the minimum THD is recorded as 1.31% for the 207 V_{rms}, as seen in Figure 20 (a) and Figure 20 (b). As a result, the input voltage fluctuations are suppressed by the PI controller, and the THD is within the limits that are specified in the standard.

The output voltage fluctuation case is simulated for fuzzy controller PFC operation as well. As shown in Figure 21, the BL SEPIC output is loaded with a full load of 12 A, a quarter load of 3 A and a half load of 6 A, respectively. After the full load is applied, the input current reaches 5 A of steady current within 50 milliseconds, as seen in Figure 21 (a). Then, an instant decrease of the output current from full load to quarter load is applied, and an overshoot is observed on the output voltage and current. However, the overshoot is suppressed by the PI voltage controller thanks to its reset feature. Because the output voltage exceeds the predefined 72 V_{dc} overshoot level, the reset feature is activated. Then, the half load of 6 A is applied to the fuzzy controller. Any overshoot is not observed as shown in Figure 21 (b), and a peak level of 2.5 A is observed at the input current.

The THD results of the fuzzy controller are given in Figure 22 (a) and Figure 22 (b). The minimum transient THD of 1.31% is obtained at the full load application. Moreover, the maximum transient THD of 3.10% is observed at the quarter load application. As a result, the controller again keeps the THD percents within the range of the standard.

By using the criteria shown in Table 4, both controller performances are compared with each other. The fuzzy controller reaches the targeted 65V output level faster than the PI controller, as shown in Figure 6 (b) and Figure 16 (b). The rise time of the PI controller is 28 milliseconds, and the output is settled at 38 milliseconds. Whereas the fuzzy has a 25 millisecond rise time, and the output is settled in 35 milliseconds. The PI controller overshoot is 1.34 % of the reference value. On the other hand, the fuzzy controller overshoots the reference output by 0.32 %.

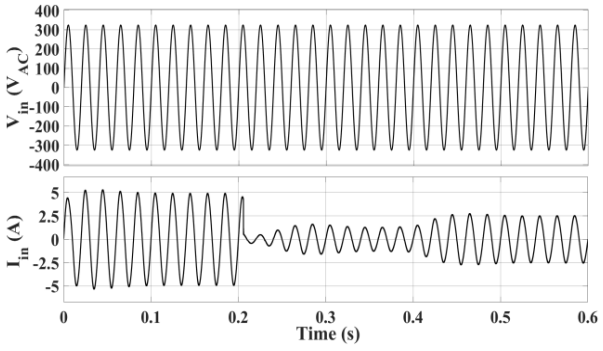

(a)

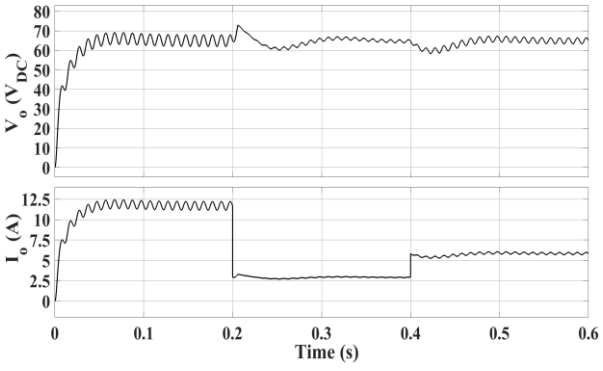

(b)

Figure 21. a) Input voltage and current of fuzzy controller when the output load fluctuation is applied, b) Output voltage and current of controller when the output load fluctuation is applied

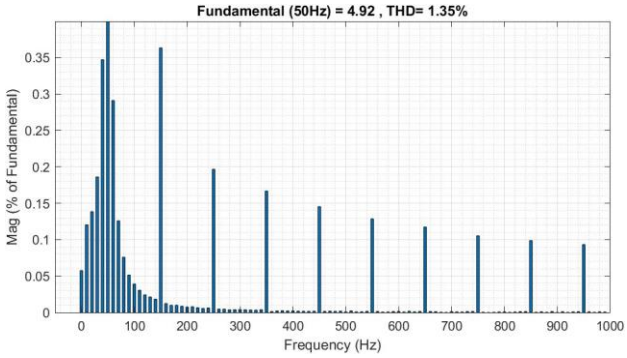

(a)

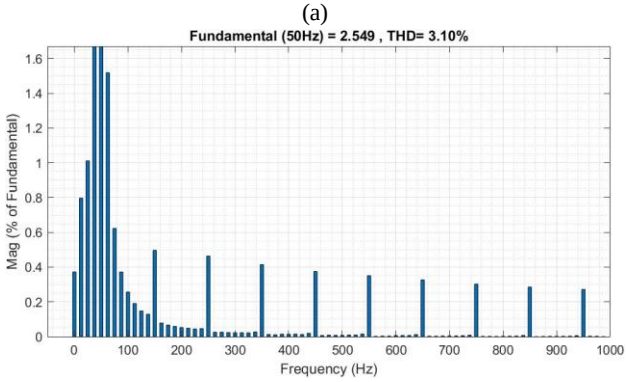

(b)

Figure 22. a) Transient THD result of fuzzy controller at full load, b) Transient THD result of fuzzy controller at quarter load

Even if the PI controller has better results for steady state operation with nominal input voltage and full load, the THD values of the fuzzy controller are better than the PI controller when simulating different input voltages and output loads. The THD results for output power changes are also given in Figure 24. The nonlinear structure of the fuzzy controller provides stable and robust control for the operational changes. The measured PF results that are given in Figure 25 are almost one for both PI and fuzzy controllers. As depicted in Figure 23, the maximum efficiencies of 93.5% and 93.4% are obtained with PI and fuzzy controllers, respectively.

The proposed topology features are also compared with similar BL topologies in the literature as given in Table 5 and Table 6. If the THD and PF performances of the topologies are compared, the BL CUK topology has the lowest steady state THD of 2.3 % with almost unity PF. The highest THD belongs to the BL Landsman topology with a unity PF. The minimum transient THD belongs to the BL zeta SEPIC with 1.8 %, and the maximum transient THD belongs to the BL boost converter. On the other hand, the proposed topology achieved steady state THD values of 1.08 % with the PI controller and 1.33 % with the fuzzy controller while the PF is almost unity. Moreover, the fuzzy controller has lower THD values for input voltage changes and the load changes. The proposed topology has also isolation, low input ripple and fewer complexity advantages. However, the proposed topology has medium efficiency among the compared topologies, high output ripple and discontinuous conduction mode (DCM) operation. The component counts of each topology are given in Table 6. The most complex topologies are the BL boost and BL landsman topologies due to their switching element and component numbers. In contrast, the BL CUK, BL totem pole and the proposed BL SEPIC are the least complex topologies.

Table 4. Comparison table of controllers

Properties	*PI*	*Fuzzy*
Rise time (ms)	28.08	24,96
Settling time (ms)	37.98	35,14
Overshoot (%)	1.34	0.32
Reaction	slower	faster
Simulation time	lower	higher
Calculation	complex	simple
Steady State THD (%)	1.08%	1.33%
Min transient THD (%)	1.64%	1.31%
Max transient THD (%)	3.25%	3.10%
Min power factor	0.999	0.999
Max efficiency (%)	93.5	93.4

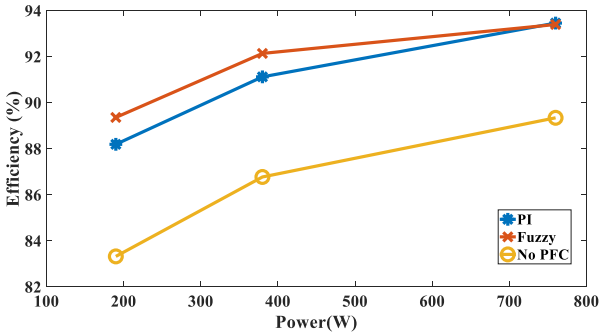

Figure 23. Efficiency results of PI, fuzzy and no PFC operation

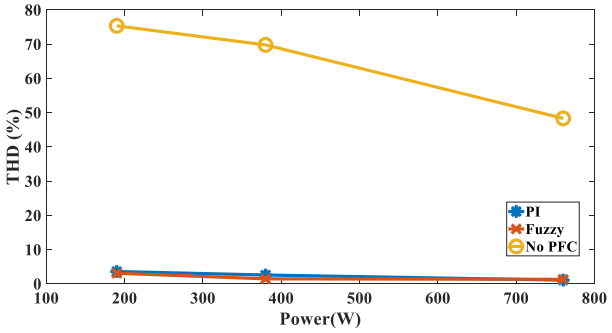

Figure 24. THD results of PI, fuzzy and no PFC operation

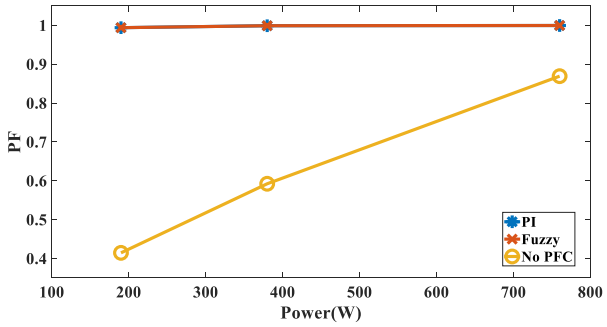

Figure 25. PF results of PI, fuzzy and no PFC operation

Table 5. Comparison table of different BL topologies

Topology	BL Boost [24]	BL Buck Boost [24]	BL Landsman [25]	BL CUK [24]	BL Zeta SEPIC [26]	BL SEPIC [27]	BL SEPIC [38]	Proposed With PI Controller	Proposed With Fuzzy Controller
MOSFET Voltage Stress	High	High	High	Low	High	Low	Low	Low	Low
MOSFET Current Stress	Low	High	High	High	Low	High	High	High	High
Input Ripple	Low	Low	Low	Low	Low	Low	Low	Low	Low
Output Ripple	Low	Low	High	Low	Low	High	High	High	High
Isolation	No	Yes	Yes	No	Yes	No	Yes	Yes	Yes
Operation Mode	CCM	DCM	CCM	DCM	DCM	DCM	DCM	DCM	DCM
Max Efficiency (%)	98.9	82	91	94	92	93.3	92.3	93.5	93.4
Rated Power (VA)	3400	856	885	1000	878	453	762	760	760
Steady State THD (%)	<5	3.5	4.8	3.49	2.3	4.0	1.55	1.08	1.33
Min Transient THD (%)	3.5	2.3	4.3	3.49	1.8	2.7	2.32	1.64	1.31
Max Transient THD (%)	41	3.5	4.8	3.88	<5	5.2	5,8	3.25	3.1
PF	0.99	1	1	0.9994	1	0.99	1	0.999	0.999

Table 6. Comparison table of different BL topologies

Topology	Number of Components						Total	Complexity	Cost
	L	Tr	C	Sw	D	Rl			
BL Boost [24]	4	0	1	4	4	0	13	Medium	~39.3$
BL Buck Boost [24]	3	1	3	3	5	0	15	High	-
BL Landsman [25]	5	1	5	3	5	0	18	High	~74.1$
BL CUK [24]	2	0	3	2	2	0	9	Low	~74.7$
BL Zeta SEPIC Flyback [26]	3	1	4	3	3	0	14	Medium	-
BL SEPIC [27]	3	0	2	2	4	0	11	Low	-
BL SEPIC [38]	1	2	3	2	2	0	10	Low	-
Proposed	1	2	3	2	2	0	10	Low	-

Note: L: Inductor, Tr: Transformer, C: Capacitor, Sw: Switch, D: Diode, Rl: Relay

4. Conclusion

In this study, BL SEPIC is introduced to reduce THD more effectively than traditional bridge rectifiers. Then, the PI and fuzzy controllers are compared using the BL SEPIC converter. Even if the fuzzy controller has a faster response time than the PI controller, simulating the fuzzy controller requires much more computational effort. However, the calculations for the fuzzy controller are less complex because a mathematical model of the system is required for the PI controller to calculate P and I coefficients correctly, whereas the fuzzy controller merely needs language qualifiers to create input and output relations.

The comparison of PFC operation for both controllers is obtained from the simulation results. The PI and fuzzy controllers have minimum steady state THD values of 1.08% and 1.33%, respectively. However, the BL SEPIC is also simulated to see the transient performance of the controllers. Initially, the input voltage fluctuations are applied to the controllers. The results show that the PI controller has a minimum of 1.64% transient THD, while the fuzzy controller has 1.31% transient THD. Finally, the output load variation is applied. It is seen that the PI controller has a maximum of 3.25% transient THD, while the fuzzy controller has 3.10% transient THD. As a result, the THD performance of controllers complies with IEC 61000-3-2:2018 requirements. On the other hand, the fuzzy controller demonstrated better operation for input voltage and load current changes. Therefore, the fuzzy controller is a more stable and robust method as compared with the PI controller method. Also, the obtained THD values are within the

standard voltage limits of < 5% that is specified in IEC 60038:2009. The THD and PF requirements in regulations and standards provide increasing power quality for grid connected devices such as EV chargers. The upcoming future may lead to up-to-date regulations such as more strict PFC operation, power efficiency, or device performance due to the increasing need for power. Therefore, the following studies are listed below as future scope of the proposed work.

- The fuzzy controller can be simulated with other BL converters to investigate their PFC performance with non-linear systems.
- The simulated results can also be implemented in a practical application to see the practical PFC performance. Also, efficiency can be increased by using GaN or SiC based semiconductors.
- Several other non-linear control methods such as sliding mode control and model predictive control can be implemented in the bridgeless topologies for further performance enhancement and comparisons.

Declaration

The author(s) declared no potential conflicts of interest with respect to the research, authorship, and/or publication of this article. The author(s) also declared that this article is original, was prepared in accordance with international publication and research ethics, and ethical committee permission or any special permission is not required.

Author Contributions

The study is supervised by A. Karaarslan. The control algorithms and the proposed topology are implemented and simulated in MATLAB Simulink by A. Uğurluoğlu. The manuscript was written by A. Uğurluoğlu and controlled by A. Karaarslan.

References

1. Drobnič, K., G. Grandi, M. Hammami, R. Mandrioli, A. Viatkin, and M. Vujacic, *A ripple-free dc output current fast charger for electric vehicles based on grid-tied modular three-phase interleaved converters.* In 2018 International symposium on industrial electronics (INDEL), 2018. p.1-7.
2. Ajanovic, A., and R. Haas, *Economic and environmental prospects for battery electric-and fuel cell vehicles: a review*. Fuel cells, (2019). **19**(5): p.515-529.
3. Rahman, S., I. A. Khan, and M. H. Amini, *A review on impact analysis of electric vehicle charging on power distribution systems.* In 2020 2nd International Conference on Smart Power & Internet Energy Systems (SPIES), IEEE, 2020, p. 420-425.
4. Koç, M., O. B. Tör, and Ş. Demirbaş, *Analysis the Effects of Electric Vehicles on Distribution Networks with Simulations Based on Probabilistic Methods.* Gazi University Journal of Science Part C: Design and Technology, 2021. **9**(1): p.95-107.
5. Akın, Ö., İ. Özer, and H. Ünlü, *Selective harmonic elimination in multi-level inverters by using neural networks.* International Advanced Researches and Engineering Journal, 2021. **5**(1): p.19-25.
6. Das, P., M. Pahlevaninezhad, J. Drobnik, G. Moschopoulos, and P. K. Jain, *A nonlinear controller based on a discrete energy function for an AC/DC boost PFC converter.* IEEE Transactions on Power Electronics, 2013. **28**(12): p.5458-5476.
7. Pena-Alzola, R., M. A. Bianchi, and M. Ordonez, *Control design of a PFC with harmonic mitigation function for small hybrid AC/DC buildings.* IEEE Transactions on Power Electronics, 2015. **31**(9): p.6607-6620.
8. *Limits for Harmonic Current Emissions (Equipment Input Current up to and Including 16A Per Phase)*. IEC Std. 61000-3-2, 2020.
9. Karaman, Ö. A., A. Gündoğdu, and M. Cebeci, *Performing reactive power compensation of three-phase induction motor by using parallel active power filter.* International Advanced Researches and Engineering Journal, 2020. ***4***(3): p.239-248.
10. Musavi, F., M. Edington, W. Eberle, and W. G. Dunford, *Evaluation and efficiency comparison of front end AC-DC plug-in hybrid charger topologies.* IEEE Transactions on Smart grid, 2011. **3**(1): p.413-421.
11. Valascho, R., and S. Abdel-Rahman, *Digital PFC CCM boost converter*. Infineon Technologies, Application Note, Munich, Germany, 2016.
12. Kalair, A., N. Abas, A. R. Kalair, Z. Saleem, and N. Khan, *Review of harmonic analysis, modeling and mitigation techniques.* Renewable and Sustainable Energy Reviews, 2017. **78**: p.1152-1187.
13. Jang, Y., and M. M. Jovanović, *Bridgeless high-power-factor buck converter.* IEEE Transactions on Power Electronics, 2010. **26**(2): p.602-611.
14. Jang, Y., and M. M. Jovanovic, *A bridgeless PFC boost rectifier with optimized magnetic utilization.* IEEE Transactions on Power Electronics, 2009. **24**(1): p.85-93.
15. Zhao, B., A. Abramovitz, and K. Smedley, *Family of bridgeless buck-boost PFC rectifiers.* IEEE Transactions on Power Electronics, 2015. **30**(12): p.6524-6527.
16. Akhtar, M. F., S. R. S. Raihan, N. A. Rahim, M. N. Akhtar and E. Abu Bakar, *Recent developments in DC-DC converter topologies for light electric vehicle charging: a critical review.* Applied Sciences, 2023. ***13***(3): p.1676.
17. Kushwaha, R., B. Singh and V. Khadkikar, *An improved PQ Zeta converter with reduced switch voltage stress for electric vehicle battery charger.* In 2020 IEEE Energy Conversion Congress and Exposition (ECCE), 2020, October. p. 858-863. IEEE.
18. Gupta, J., R. Kushwaha and B. Singh, *An Isolated Improved Power Quality Battery Charger for a Light Electric Vehicle.* In 2020 IEEE International Conference on Power Electronics, Smart Grid and Renewable Energy (PESGRE2020), 2020, January, p. 1-6. IEEE.
19. Samsudin, N. A., D. Ishak, and A. B. Ahmad, *Design and experimental evaluation of a single-stage AC/DC converter with PFC and hybrid full-bridge rectifier.* Engineering science and technology, an international journal, 2018. **21**(2): p.189-200.
20. Jeong, S. G., J. M. Kwon, and B. H. Kwon, *High-efficiency bridgeless single-power-conversion battery charger for light electric vehicles.* IEEE Transactions on Industrial Electronics, 2018. **66**(1): p.215-222.
21. Pandey, R., and B. Singh, *PFC-SEPIC converter-fed half-*

bridge LLC resonant converter for e-bike charging applications. IET Electrical Systems in Transportation, 2020. **10**(3): p.225-233.

22. Zhou, K., H. Yang, Y. Zhang, Y. Che, Y. Huang and X. Li, *A review of the latest research on the topological structure and control strategies of on-board charging systems for electric vehicles.* Journal of Energy Storage, 2024. *97*: 112820.
23. Onal, Y., *Analysis of a new SEPIC AC–DC PFC converter for light emitting diode applications.* Emerging Materials Research, 2021. **11**(1): p.51-59.
24. Dutta, S., S. Gangavarapu, A. K. Rathore, R. K. Singh, S. K. Mishra and V. Khadkikar, *Novel single-phase Cuk-derived bridgeless PFC converter for on-board EV charger with reduced number of components*. IEEE Transactions on Industry Applications, 2022. ***58***(3): p.3999-4010.
25. Kushwaha, R. and B. Singh, *Power factor improvement in modified bridgeless landsman converter fed EV battery charger.* IEEE transactions on Vehicular Technology, 2019. ***68***(4): p.3325-3336.
26. Kushwaha, R. and B. Singh, *Power factor correction in EV charger with bridgeless Zeta-SEPIC converter.* In 2019 IEEE Energy Conversion Congress and Exposition (ECCE), 2019, September, p.121-128. IEEE.
27. Gupta, J., R. Kushwaha, B. Singh and V. Khadkikar, *Improved power quality charging system based on high step-down gain bridgeless SEPIC APFC for light electric vehicles.* IEEE Transactions on Industry Applications, 2021. **58**(1): p.423-434.
28. Çamur, H., Z. Ortatepe and A. Karaarslan, *Comparative Analysis of Current Control Methods Implemented in Single-Phase Boost PFC Converter in CCM Mode*. International Scientific Research and Innovation Congress-ISARC, İstanbul, Turkey, 2022. p.984-992.
29. Gupta, M., N. Gupta, M. M. Garg and A. Kumar, *Robust control strategies applicable to DC–DC converter with reliability assessment: A review*. Advanced Control for Applications: Engineering and Industrial Systems, 2024. ***6***(3): p.217.
30. Mumtaz, F., N. Z. Yahaya, S. T. Meraj, B. Singh, R. Kannan and O. Ibrahim, *Review on non-isolated DC-DC converters and their control techniques for renewable energy applications.* Ain Shams Engineering Journal, 2021. ***12***(4): p.3747-3763.
31. Aldemir, A. and M. S. Anwer, *Determination of optimal PID control parameters by response surface methodology*. International Advanced Researches and Engineering Journal, 2020. ***4***(2): p.142-153.
32. Hitit, Z. Y., İ. Koçer, G. Kuş, N. Z. Arslan, E. P. Dal and H. Koz, *Optimal PID control with anti-windup in neutralization process.* International Advanced Researches and Engineering Journal, 2023. ***7***(3): p.138-145.
33. Sundaramoorthy, S., M. G. Umamaheswari, G. Marimuthu and B. Lekshmisree, *Hopfield neural network-based average current mode control of synchronous SEPIC converter*. IETE Journal of Research, 2023. ***69***(6): p.3897-3915.
34. Durgadevi, S. and M. G. Umamaheswari, *Analysis and design of single phase power factor correction with DC–DC SEPIC Converter for fast dynamic response using genetic algorithm optimised PI controller.* IET Circuits, Devices & Systems, 2018. ***12***(2): p.164-174.
35. Xia, B., Y. Li, G. Zhang, Q. Cheng and F. Ding, *A double-layer ring-structured equalizer for series-connected lithium-ion battery pack based on model predictive control.* Journal of Energy Storage, 2024. ***78****:* p.110047.
36. Sezen, A. and K. Keskin, *Hybrid Control of DC-DC Buck Boost Converter*. Demiryolu Mühendisliği, 2021. (14): p.99-109.
37. Köseoğlu, E. and A. Karaarslan, *Modified Bi-Directional Cuk Converter For Cell Balancing Using PI And Fuzzy Logic Control Method.* Journal of Optimization and Decision Making, 2023. ***2***(2): p.283-289.
38. Singh, B., and R. Kushwaha, *A PFC based EV battery charger using a bridgeless isolated SEPIC converter.* IEEE Transactions on Industry applications, (2019). **56**(1): p.477-487.
39. Kunjittipong, N., K. Kongkanjana, and S. Khwan-on, *Comparison of fuzzy controller and PI controller for a high step-up single switch boost converter.* In 2020 3rd International Conference on Power and Energy Applications (ICPEA), IEEE, 2020. p. 94-98
40. *Voltages*, I. S. Iec standard iec 60038. Ed, 2009.
41. ALKAN, Ö., S. TOSUN and Ö. ALKAN, *Enerji Kalitesi Açısından Harmonikli Bir Sağlık Tesisinin İncelenmesi.* Düzce Üniversitesi Bilim ve Teknoloji Dergisi, 2019. **7**(1): p.709-721.
42. Marti, J. V., *Analysis of duty cycle to output voltage transfer functions of cúk-like class dc-dc converters.* In Annual Seminar on Automation, Industrial Electronics and Instrumentation, 2015.
43. Sevim, D., and V. Gider, *Designing a Control Interface and PID Controller of CUK Converter*. European Journal of Technique (EJT), 2021. **11**(1): p.93-100.
44. Anusiya, K., and K. Ramadas, *SEPIC converter based transformer less grid tied PV system with reactive power compensation.* In 2017 IEEE International Conference on Intelligent Techniques in Control, Optimization and Signal Processing (INCOS), 2017. p.1-7.
45. Çamur, H., Z. Ortatepe, and A. Karaarslan, *Fuzzy logic control based dual input boost converter.* 4. International Scientific Research and Innovation Congress, İstanbul, Turkey, 2022. p.993-1002.

Available online at www.dergipark.org.tr/en

INTERNATIONAL ADVANCED RESEARCHES
and
ENGINEERING JOURNAL

Journal homepage: www.dergipark.org.tr/en/pub/iarej

e-ISSN: 2618-575X

International
Open Access

Volume 08
Issue 03

December, 2024

Research Article

Emergency communication solution with GPS and morse coding during earthquake using microcontroller and radio frequencies

İshak Parlar [a,*], ***Armağan Umut Alkan*** [a] ***Mehmet Aykutbay*** [a] ***and Özge Aksan*** [a]

[a]*Van Yüzüncü Yıl University, Faculty of Engineering, Department of Electrical and Electronics Engineering, Van, 65030, Türkiye*

ARTICLE INFO

Article history:
Received 07 August 2024
Accepted 12 December 2024
Published 20 December 2024

Keywords:
GPS module
Morse code
Natural disaster
UN SOS

ABSTRACT

This study discusses a modular and practical solution that enables secure communication during natural disasters with GPS signals of Morse code. It is an innovative solution that aims to effectively coordinate emergency services and aid teams by providing an alternative communication channel for the communication infrastructure damaged during natural disasters. In cases such as earthquakes, which are always on the agenda of our country and should be, the solution of emergency aid and communication infrastructure problems has become a focused topic. The aim of the study is to provide an alternative communication channel in cases where this communication is damaged. A specially designed radio transmitter circuit, GPS module and MORSE alphabet coding system constitute the basic components of our study. This solution will enable rapid intervention and coordination by transmitting real-time location information to local and international aid teams. The Arduino platform will allow us to adapt to different scenarios by providing flexibility and customizability. The radio transmitter circuit is designed for effective communication on the 2549Hz frequency, which is the UN SOS (United Nations Emergency Radio Frequency Line) line. The GPS data obtained with the help of sensors is encoded in the form of the MORSE alphabet with the help of a microcontroller and transmitted to the international helpline, and the location information is transmitted quickly and reliably. This system was tested for a short time in a laboratory environment and in an environment where communication was partially interrupted. Being accessible and applicable in terms of cost calculation increases the importance and effectiveness of the study in terms of appealing to every user. As a result, we aim to provide a vital alternative in cases where communication networks are inadequate, and to provide social benefit and scientific contribution.

1. Introduction

Our article aims to provide an alternative communication channel in case the communication infrastructure is damaged during natural disasters such as earthquakes, and aims to code the coordinates with Morse code and transmit them to help frequencies via radio waves. This alternative channel plays a life-saving role by ensuring that emergency services and relief teams are effectively coordinated and able to respond quickly. Our project offers an innovative solution that provides a tangible benefit to society by integrating social responsibility awareness with advanced technological knowledge and experience. By implementing technological developments in the field of disaster management that directly affects human life, our project aims to provide usefulness, benefit and convenience to society. In addition, it produces solutions to make life easier in technologically and economically disadvantaged regions and realizes these technologies with original and national resources [1-5]. The study has been meticulously evaluated and designed to be put into practice.

Considering the current literature studies, there are various studies on the subject, but our study is expected to provide a wider range of originality and applicability. When we look at these studies, it can be seen that communication issues are applied to a more limited area when needed. We aim to achieve success with this project in these years when our country is frequently on the agenda with natural disasters. At the same time, designing this project with an international communication code is expected to be beneficial not only for our country but also for our other neighbors, and this project will be used as a basis in future processes and

* Corresponding author. Tel.:+90 552 013 96 53; Fax: 0432 225 17 30.
E-mail addresses: ishakparlar@yyu.edu.tr, armaganumuta@gmail.com, fcroouu@gmail.com, ozgeaksan65@gmail.com
ORCID: *0000-0002-3383-8091, 0009-0001-9581-5389, 0009-0006-2125-022X, 0009-0009-1223-7447*
DOI: 10.35860/iarej.1529877

years [1-5].

When we look at some studies on the structure; The increased use of smartphones has brought with it many innovations that provide convenience in human life. One of these conveniences is the global positioning system that is standard in smartphones. Thanks to this system, the person using the mobile device can find his location precisely, without allowing address confusion. In this study, it is tried to use this system to find the nearest taxi and communicate, as well as to find the location of another type of vehicle that is wanted to be followed and to track it on the map [2-6].

In another important study; A device that broadcasts information such as pulse and body temperature, which can be described as vital signals for people, with location data received from GPS satellites, on the amateur radio band with the APRS protocol, has been designed. The broadcasts can be received by portable PMR radios and amateur radio stations. It has also become possible to monitor radio broadcasts over the Internet via I-GATEs [3-7]. Finally, in another important study; An accident emergency call system has been designed to help treat the injured as quickly as possible by automatically informing the emergency team in case of accidents. The designed system uses the GPS module to send messages containing information such as the location of the vehicle, the deployed airbag number, vehicle model, age and license plate to the emergency team when the airbag of the accident vehicle is deployed [8]. In general, in such projects, Morse code provides communication between the receiver and the transmitter with a communication infrastructure. However, this study uses a more secure infrastructure such as GPS instead of transmitting Morse codes over the communication channel. Since communication infrastructures are damaged during natural disasters, communicating with the GPS module is of great importance in terms of both information security and time. This project creates great differences compared to other search and rescue modules due to its modular structure and especially in terms of cost.

As a result, reaching a target solution with an international aid code instead of just calling for local help in urgent and vital places and times highlights the effectiveness and awareness of our work.

2. Material and Method

2.1 Problem Analysis

• ***Fragility of Communication Infrastructure:*** Natural disasters or crisis situations such as earthquakes often cause damage to the communication infrastructure. This makes it difficult for emergency teams to coordinate effectively and prevents rescue operations from being directed in a timely and accurate manner.

• ***Lack of Alternative Communication Channels:*** When traditional communication systems often fail or are overloaded, alternative communication channels are needed for emergencies. However, the widespread and effective use of such alternative systems is limited.

• ***Social Media in the Maraş Earthquake:*** It is a known fact that news was received about many damaged and collapsed buildings in the Maraş earthquake thanks to social media. However, false/misshared information and locations have repeatedly caused teams to receive false reports. For this reason, unfortunately, many wrecks could not be found. It is extremely important to know which building was actually damaged during an earthquake. Failure to convey this information correctly to aid teams constitutes one of the main problems [6-8].

2.2 Problems Providing Possible Solutions

Our study shows that existing solutions are often dependent on GSM networks or internet connections and frequently become unusable during disasters. While solutions such as walkie-talkie devices or emergency message systems that offer limited information transfer provide short-distance communication, they are inadequate for long-distance and reliable information transfer. The study provides an innovative and effective alternative in this context, providing critical information transfer in disaster situations and accelerating emergency response processes. Thus, it aims to provide social benefit by filling an important gap in the field of disaster management and emergency services [14-16].

2.3. Solution

2.3.1 Problem Solving Mechanism

1.Detection: The gyroscope sensor detects the tremors that occur during an earthquake and triggers the system.

2.Data Collection: GPS module collects real-time location data.

3.Coding: The location data collected is encoded with Morse code.

4.Communication: The encoded data is transmitted to the international hotline at the frequency of 2549Hz through the special radio transmitter circuit.

5.Coordination: Emergency teams can make rapid response and coordination based on the location information received.

6. Independent Operation: It is aimed to create a product that can operate independently of the grid with the help of solar energy panels.

7. Cost Analysis: All parts used in the study were obtained from waste products and recycled materials. The total cost of electronic parts, components, GPS module and plastic parts varies between approximately 500-1000 TL. Especially being accessible will make a significant contribution to our country, which is an earthquake zone.

Our project aims to offer a sustainable communication solution that does not require maintenance, repair and renovation, unlike traditional communication systems. DAIS allows disaster victims and emergency services to communicate effectively and can thus play an important role in emergency communication. The project offers a vital alternative in cases where communication networks are inadequate and provides social benefit. They also provide significant contribution to disaster management, potentially saving lives.

2.4 Solution Proposal

• ***Specially Designed Radio Transmitter Circuit:*** The specially designed radio transmitter circuit to be used in the electronic circuit is designed to provide reliable communication in cases where the communication infrastructure collapses. This circuit offers the ability to communicate effectively on the BM SOS line frequency.

• ***GPS and Morse Code Integration:*** The GPS module and Morse code coding system aim to transmit real-time location information quickly and reliably in emergency situations. In this way, relief teams can quickly reach the scene and manage operations more efficiently [18-25].

• ***Using Arduino Platform:*** Arduino platform provides flexibility and customizability. In this way, you can adapt to different geographical and operational scenarios and adapt the system as needed.

• ***Hardware:*** Electrical connections of radio transmitter circuit and GPS module equipment

• ***Software:*** Ensuring communication by coding with Morse code

• ***Coordination:*** Patent studies and cooperation with Van YYÜ

Figure 2 shows the details of the designed Emergency Communication System (ECS). The gyroscope sensor, UART NEO-6M GPS module, RF radio transmitter card, voltage regulator and 868Mhz 3dBi SMA antenna are mounted on a perforated pertinax electronic circuit board connected to Arduino Uno R3, which we use as the microcontroller platform. If it is in a prototype box that is resistant to environmental conditions; Li-ion Battery with 3.7V-3200mAh protection circuit, Charge Control Regulator, 12W Perc Monocrystalline Solar Panel, LM2940 5V voltage regulator and cable components are installed. In addition, it is aimed to install the integrated structure with the prototype resistant to environmental conditions in a way that the windows can see the sun in apartments or detached houses. Even if the energy coming from the solar panel is not continuous, location data sharing can be provided uninterruptedly for approximately 2 years with a fully charged battery in the event of an earthquake. Since the energy needs will be met by using solar panels, the devices will be able to operate without being dependent on any electrical system. This feature provides a great advantage, especially in disaster areas, because the devices can operate as an uninterruptible power source even if the electrical infrastructure is damaged.

The planned prototype of our study is shown in Figure 2. In the waves seen on the oscilloscope screen, the period $f = 2548Hz$ is calculated as approximately $T = 392us$. The waves related to the measurement of these waves and the trial code are sent only to the Morse code: "." Frequency adjustments are made with the (dot emphasis) code. The oscilloscope screen shows a visual showing whether there is a phase shift between sending this frequency with the Arduino Uno and transmitting it with the radio circuit. The transmission of the Morse code encoded by the radio circuit to the receiver has been successfully completed. ECS contains a voltage regulator and battery charging circuits to adjust the operating voltage. In addition, the design was developed using a standard radio transmitter design and minimum circuit elements.

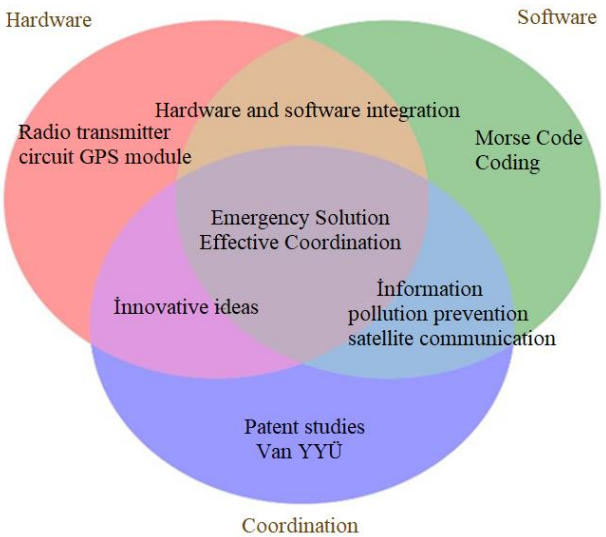

Figure 1. Schematic representation of the project realization process

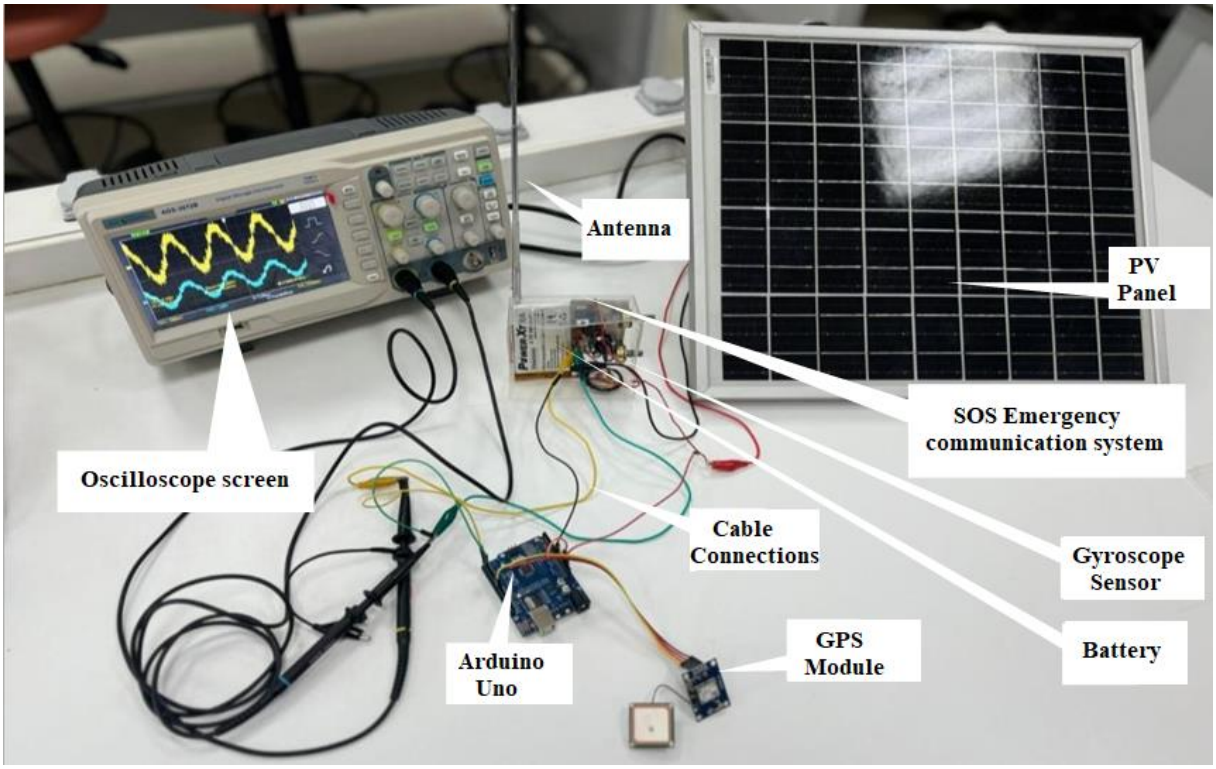

Figure 2. SOS emergency communication system prototype in-box test image

2.5 Writing SOS in Morse Code

The SOS text is expressed in Morse code as follows: "... --- ..." To transmit the SOS message in Morse code at a frequency of 2549 Hz, signals are sent by changing the frequency in a certain time period. Each short signal (dot) and long signal (dash) in Morse code is transmitted for a certain period of time, with gaps between these periods. Figure 3 shows the Morse code transmission circuit.

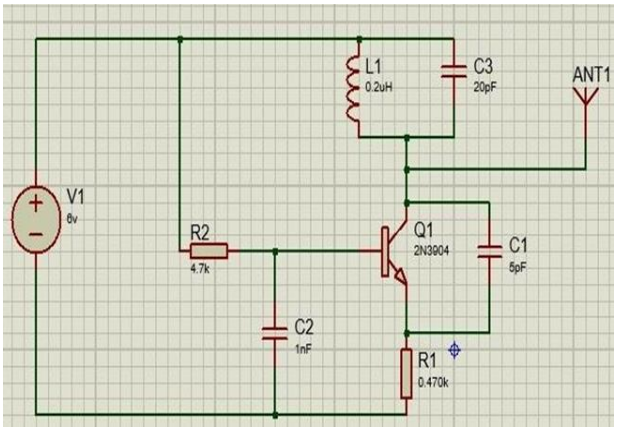

Figure 3. Radio transmitter circuit schematic representation

2.5.1 Timing Diagram of SOS Message

1. S: ...
Dot: 0.15 seconds
Space: 0.1 seconds
Dot: 0.15 seconds
Space: 0.1 seconds
Dot: 0.15 seconds
Space between letters: 1.2 seconds

2. O: ---
Dash: 1 second
Space: 0.1 seconds
Dash: 1 second
Space: 0.1 seconds
Space: 0.1 seconds
Dash: 1 second
Space between letters: 1.2 seconds

3. S: ...
Dot: 0.15 seconds
Space: 0.1 seconds
Dot: 0.15 seconds
Space: 0.1 seconds
Dot: 0.15 seconds

Space between words: 1.5 seconds (message may repeat when space between words ends)

Total Time

- S: 0.15 + 0.1 + 0.15 + 0.1 + 0.15 + 1.2= 1.85seconds
- O: 1 + 0.1 + 1 + 0.1 + 1 + 1.2 = 4.4 seconds
- S: 0.15 + 0.1 + 0.15 + 0.1 + 0.15 + 1.5 = 2.15seconds
- Total: 1.85 + 4.4 + 2.15 = 8.4 seconds

That is, the SOS message is transmitted at a frequency of 2549 Hz, repeated approximately every 3.4 seconds.

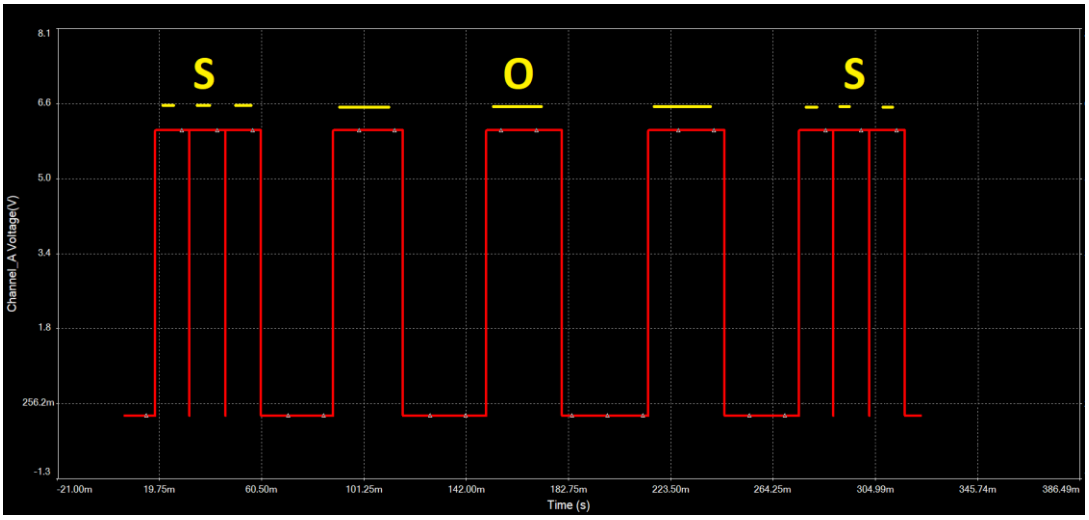

Figure 4. Voltage response of SOS signal (simulation)

Figure 4 shows the voltage response of the square signal in each signal of the SOS signal. These results were obtained in the Multisim circuit package program. The circuits in the application circuit and the Morse code signals are parallel. The source voltage selected in the simulation is 6V and the timing period is selected shorter. In the Multisim program, approximately 0.3 seconds was selected to shorten the simulation time.

3.Target Audience

Local and national emergency management teams that require effective intervention in natural disasters such as earthquakes, floods and fires, first responders such as fire brigade, medical personnel and police, non-governmental organizations such as Kızılay and AFAD that carry out aid and rescue work, disaster management and emergency planning municipalities and local governments, as well as military units that coordinate security and aid operations [11-13].

Our users are emergency management professionals, search and rescue teams, local government and municipality personnel who perform critical information transfer and coordination tasks in disaster situations, and employees of non-governmental organizations who organize aid and support activities [12]. This project is designed for individuals and communities experiencing communication problems and aims to save lives by providing reliable and fast communication during disasters.

4. SWOT Analysis

With this analysis, it is stated that the strengths and weaknesses of the system, as well as what potential it is open to, provide a holistic perspective to our study. Figure 5 shows the SWOT Analysis report.

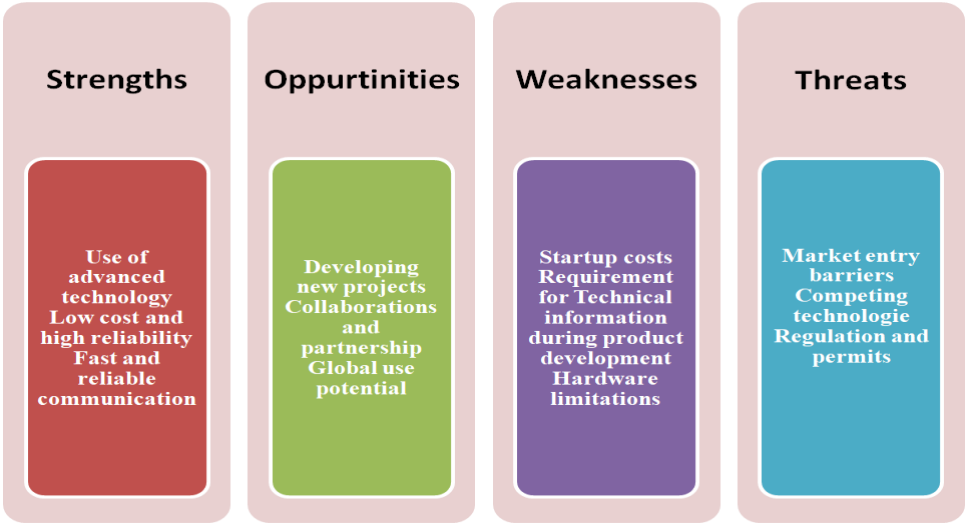

Figure 5. SWOT analysis report representation

Strengths: Our project provides an alternative communication channel in case the communication infrastructure is damaged during natural disasters, providing fast and reliable communication with low cost and high reliability through the use of advanced technology. The GPS module, radio transmitter circuit and Morse code coding system can reduce casualties and shorten response times by enabling the transfer of critical information in case of disaster.

Weaknesses: The initial costs of our project are high, and the implementation and integration processes may be complex due to the need for technical knowledge. Additionally, limitations of the hardware and software components used may affect the flexibility and extensibility of the project. These factors can create challenges for the sustainability and scalability of the project.

Opportunities: Our project offers opportunities to develop new projects and establish collaborations in the field of disaster management and emergency communication. Partnerships, especially with public institutions, non-governmental organizations and international aid organizations, can enable our project to reach wider audiences and be used on a global scale. Additionally, our project has the potential to increase its competitive advantage with technological developments and innovative solutions.

Threats: Market entry barriers are an important threat that our project may face during the commercialization process. The existence and rapid development of competing technologies may affect the competitiveness of our project. In addition, regulations and legal permissions in the field of disaster management and emergency communication may make it difficult to implement and expand our project. Strategic planning should be made to ensure the success and sustainability of our project by taking precautions against these threats.

5. Conclusions

This study aims to enable rapid response and provide social benefit by playing a critical role in disaster management with the support of specially designed hardware and software. Therefore, our project offers a vital communication channel during earthquakes and other natural disasters with its innovative approach and technological superiority. Existing solutions often depend on GSM networks or internet connectivity, and these infrastructures often become unusable during disasters. Our project offers an original study with long-distance and reliable information transfer using Morse code. The GPS module and Morse code coding system used distinguish it from existing solutions by providing fast and reliable communication in case of disaster. This innovative technology can reduce casualties and shorten response times by enabling the transfer of critical information in disaster situations. By using commercially available components, our product can be produced quickly and effectively with existing production infrastructures. Our prototype studies prove the feasibility and successful results of our product in real-world conditions, demonstrating its commercial viability.

Our project also offers ample opportunities for new projects and collaborations. It is envisaged that the impact area will be further increased with additional modules and software that will adapt to different scenarios in the field of disaster management and emergency communication. Collaborations with public institutions, non-governmental organizations and the private sector can also increase the impact of our product by enabling it to reach wider audiences. Therefore, our project provides both social benefit and has the potential to be commercially successful.

Declaration

The author(s) declared no potential conflicts of interest with respect to the research, authorship, and/or publication of this article. The author(s) also declared that this article is original, was prepared in accordance with international publication and research ethics, and ethical committee permission or any special permission is not required.

Author Contributions

All authors have the same contribution in this study.

Acknowledgment

We would like to express our gratitude to Doç. Dr. Bilal Tütüncü for his valuable support during the project process, to the Dean of Van Yüzüncü Yıl University Faculty of Engineering for providing laboratory facilities, and to Van Yüzüncü Yıl University İNNOVAN Entrepreneurship Center for technical support. Additionally, this study; It was supported by Van Yüzüncü Yıl University Scientific Research Project unit within the scope of project number FLO-2023-10886.

References

1. Dağlarlı, E., Arıbaş, E. *Design of Fixed Wing Autonomous Figting UAV*. In 2024 8th International Artificial Intelligence and Data Processing Symposium (IDAP). 2024, September, p. 1-6. IEEE.
2. Başaran, İ. *Akıllı Kargo Takip ve Güvenlik Sistemi* (Master's thesis, Marmara Universitesi (Turkey)). 2024.
3. Güngör, Ö. *Elektronik modüler kullanılarak hava aracı göstergelerinin sayısal göstergeler olarak tasarımı ve uygulaması.* 2024.

4. Umapathi, N., Suganthi, S. U., Divyasri, A. *Morse Code to Text Converter using Arduino. Grenze* International Journal of Engineering & Technology (GIJET), 2024. **10**(1).
5. Van Devender, N., Hardesty, M., Dua, R. *Morse Code to Text Translator*. In 2023 ASEE Midwest Section Conference. 2024, July.
6. Sağbaş, E. A. *Küresel Konumlama Servisi Kullanarak Araç Takibi ve Mobil Cihazlar Arası Haberleşme.* Akademik Bilişim Konferansı, 2014, p. 5-7.
7. Göksu, T., Uğuz, S. *Konum Bilgisi ve Hayati Sinyallerin APRS Tabanlı Telsiz Haberleşme Sistemi ile Yayınlanması,* 2016.
8. Ekşi, Z., Çakıroğlu, M. *Trafik kazaları için bir acil yardım çağrı sistemi tasarımı.* Sakarya University Journal of Science, 2013. **17**(3), p. 315-319.
9. Genç, F. N. *Türkiye'de doğal afetler ve doğal afetlerde risk yönetimi.* Stratejik Araştırmalar Dergisi, 2007. **9**(5), p. 201-226.
10. Gülüm, E. *Remembering a disastrous past to imagine catastrophic future (s) on social media: The expected Istanbul earthquake.* Media, Culture & Society, 2024. 01634437241228724.
11. Özkul, B., Karaman, E. (2007). Doğal afetler için risk yönetimi. TMMOB Afet Sempozyumu, **5**(7), p. 251-260.
12. Şahinsoy, K. *Kriz Yönetimi Açisindan Geleneksel ve Sosyal Medya.* İstanbul Aydın Üniversitesi Dergisi, 2017. **9**(4), p. 1-19.
13. Argın, Y. *Doğal afetlerde sosyal medya kullanimi: 2023 Kahramanmaraş depremi özelinde Twitter örneği.* İnsanat Sanat Tasarım ve Mimarlık Araştırmaları Dergisi, 2023. **3**(1), p. 140-165.
14. Duraklar, K., Burunkaya, M. *Arduino Kontrollü Özel Amaçlı Görev Robotu Tasarımı,* 2019.
15. Lee, C. T., Shen, T. C., Lee, W. D., Weng, K. W. *A novel electronic lock using optical Morse code based on the Internet of Things.* In 2016 International Conference on Advanced Materials for Science and Engineering (ICAMSE), 2016. p. 585-588. IEEE.
16. Yang, C. H., Chuang, L. Y., Yang, C. H., Luo, C. H. *Morse code application for wireless environmental control systems for severely disabled individuals.* IEEE Transactions on Neural Systems and Rehabilitation Engineering, 2003. **11**(4), p. 463-469.
17. Galamgam, D. W., Gomez, P. J., Ungos, I. C., Villegas, M., Del Rosario, J. R. B., Bandala, A. A. *Development of a Microcontroller-based Accident Detector with Morse Code Transmitter.* In 2022 IEEE 14th International Conference on Humanoid, Nanotechnology, Information Technology, Communication and Control, Environment, and Management (HNICEM). 2022, December. p. 1-4. IEEE.
18. Haddock, P. C., Hatley, J. W., Morse, W. D., Tooley, R. D. *Integrated communications and navigation module.* In 2012 IEEE international Carnahan conference on security technology (ICCST). 2012, October. p. 1-5. IEEE.
19. Tan, B., Flood, S., Jacinto, J., Hom, D. *SOS Beacon* (Doctoral dissertation, Rutgers University), 2019.
20. Juang, J. C., Tsai, Y. F., & Miau, J. J. *Status Update of the LEAP Microsatellite.* In The Fourth Asian Space Conference, Taipei, Taiwan, 2008.
21. Shahin, A. A., Younis, M. *Alert dissemination protocol using service discovery in Wi-Fi direct.* In 2015 IEEE International Conference on Communications (ICC). 2015, June. p. 7018-7023. IEEE.
22. Cardona, O. D., Ordaz, M. G., Yamín, L., Arámbula, S., Marulanda, M. C., Barbat, A. *Probabilistic seismic risk assessment for comprehensive risk management: modeling for innovative risk transfer and loss financing mechanisms.* The 14th World Conference on Earthquake Engineering, 2008.
23. Herovic, E., Sellnow, T. L., Sellnow, D. D. *Challenges and opportunities for pre-crisis emergency risk communication: lessons learned from the earthquake community.* Journal of Risk Research, 2020. **23**(3), p. 349-364.
24. Mileti, D., & Fitzpatrick, C. *The great earthquake exper*, 2019.
25. Jang, H. C., Lien, Y. N., Tsai, T. C. *Rescue information system for earthquake disasters based on MANET emergency communication platform.* In Proceedings of the 2009 international conference on wireless communications and mobile computing: connecting the world wirelessly, 2009, June. p. 623-627.

Available online at www.dergipark.org.tr/en

INTERNATIONAL ADVANCED RESEARCHES and ENGINEERING JOURNAL

Journal homepage: www.dergipark.org.tr/en/pub/iarej

International Open Access

Volume 08
Issue 03

December, 2024

e-ISSN: 2618-575X

Research Article

A research on the importance of testing the normality assumption in microbiological data

Murat Çimen [a,*]

[a] *CMN İstatistik ve Bilimsel Araştırma Merkezi, Çorum, Türkiye*

ARTICLE INFO

Article history:
Received 13 August 2024
Accepted 02 December 2024
Published 20 December 2024

Keywords:
Data
Microbiology
Normality test

ABSTRACT

The most used distribution in statistical analysis is the normal distribution. Parametric tests (e.g. one sample t-test) require that the data are normally distributed. In this study, milk somatic cell count data (SCC) used to test the normal distribution was obtained from a farm for the first and second month of lactation. According to the findings of the present study, SCC data of the first month showed normal distribution. However, the SCC data of the second month did not show normal distribution. Since the first month data showed a normal distribution, one-sample t-test, which is one of the parametric test methods, was applied for comparison with a specific reference value; since the second month data did not show a normal distribution, the Wilcoxon One-Sample Signed Rank Test, which is the non-parametric equivalent of the one-sample t-test, was applied. When the parametric test was applied to the second month data that did not show a normal distribution, results that did not comply with the standards in terms of SCC were found. When the same data was analyzed with the nonparametric test method, results that complied with the standards were obtained. It is noteworthy that different results are obtained in both analyses. As can be seen from the research results, since existing data sets in the field of microbiology may tend to show large variations, it should be tested whether the data show normal distribution before determining the statistical analysis method. According to the research results, the normality test must be applied in the statistical analysis of microbiological data showing large variations.

1. Introduction

Before applying statistical analysis, it is of great importance to determine the analysis method appropriate to the data sets at hand. Determining the appropriate analysis method is essential for the error-free completion of scientific research design, implementation, results acquisition and interpretation stages [1]. The results obtained from the statistical analysis output will affect the research hypothesis and will direct the inferential results of the research [2]. For this reason, classification of data and detection of data that disrupts normality are also important [3]. After detecting data that violates normal distribution, two options should be considered. The first of these is to remove absurd data from the data set. However, this is not possible in every case depending on the research hypothesis. The second method is to prefer nonparametric methods instead of applying parametric methods in the analysis of data that does not conform to normal distribution [4]. This second method is a more commonly used method. Before determining the most appropriate statistical method for the current data set, it is important to know whether the data are normally distributed. A statistical method chosen without applying the normal distribution test will lead to erroneous results and erroneous interpretations [5]. This will negatively affect the reliability of the results of scientific research. The first factor that impairs the reliability of results in scientific research is sometimes the interventions in the data as a result of manipulations made by researchers intentionally to direct the hypothesis, but sometimes it is also effective in unintentionally incorrect statistical analyses [6]. Any wrong application, whether intentionally or unintentionally, can cause information pollution. This is a situation that is not welcomed in the scientific community. It is noteworthy that in recent years, articles that create information pollution have been referred to ethics committees. Authors are primarily responsible for any information pollution that may occur

* Corresponding author. Tel.: +90-*530-226-9672*..
E-mail addresses: mcimen19@gmail.com
ORCID: *0000-0003-4290-2718*

DOI: 10.35860/iarej.1532064

as a result of the application of incorrect statistical methods. Insufficient statistical knowledge does not constitute a justifiable justification for the information pollution resulting from incorrect results [7]. Researchers must have sufficient statistical knowledge to publish articles. Therefore, researchers must test whether the data is normally distributed before applying statistical analysis to their data set. [8]. According to the results, researchers should prefer parametric methods if the data fits the normal distribution and non-parametric statistical methods if they do not [9]. The methods to be determined according to these results cannot be arbitrary and random, and determining the most appropriate method is absolutely essential. There are also problems in publishing research that does not comply with this rule in academic journals [10].

In this study, normal distribution test was applied to a sample data set obtained in the field of microbiology. Although a data set in the field of microbiology is shown as an example in the research, people working in other fields of Science and Health sciences must apply normality test to the parametric data set they have, as shown in the example. This test method is very important for their research to yield reliable results [11]. This study aims to be an exemplary research in terms of showing the importance of applying the normal distribution test to the data obtained in the field of microbiology with the help of SPSS in determining the statistical method.. In this study, it was aimed to determine whether data showing large changes, especially in the field of microbiology, conform to normal distribution, and also to reveal the negative results that would be caused by incorrect statistical methods applied to data that do not conform to normal distribution. Thus, researchers will be able to determine the method according to the results to be obtained by performing a normality test on the data they have before determining a statistical method. The meticulous application of the normality test will also prevent information pollution [12]. The current study creates significant awareness in terms of both showing the importance of applying the normal distribution test and showing the possible negative effects of choosing the right statistical method on research results.

2. Material and Methods

The material and methods section consists of obtaining milk data, milk analysis and statistical analysis sections.

2.1. Obtaining data

Milk data was obtained from Çağdaş Pertek Agriculture and Livestock Tourism Construction Food Production Marketing Industry Trade Ltd. Co. To determine somatic cell counts (SCC), 10 milk samples were collected from the first and second months of the enterprise is given in Table 1.

2.2. Milk analysis

Milk samples were collected in 100-ml sterile containers to determine somatic cell counts. The somatic cell counts within taken raw milk samples were detected by the standard analysis (Microscopic count) method.

2.3 Statistical analysis

Normality test was applied to determine whether the values shown in Table 1 show a normal distribution. Shapiro Wilk test was used to determine the normal distribution of the data. If the significance level found as a result of Shapiro Wilk analysis is less than 0.05, the data is considered to comply with the normal distribution, otherwise it is considered not to comply [13]. If the data are suitable for normal distribution, parametric tests should be applied, if not, non-parametric tests should be applied [14]. The normality test of the data, one simple t test and Wilcoxon One-Sample Sign Rank Test were calculated using the SPSS 18.0 package program produced by IBM Company.

Entering the data into the SPSS program and applying the Shapiro test are shown below. In the research, monthly data were subjected to normal distribution test. The stages of entering the data into the SPSS program and analyzing them are shown in Figure 1-3.

Figure 1 shows the data being entered into the SPSS program.

Then, the Plots button is pressed and in the window that opens, the fields marked none and the fields marked Normality plots with tests are marked (Figure 3).

When you press Continue and then the OK button in the rear window, the analysis result is obtained.

3. Results and Discussion

It would be useful to examine the scatter plots before examining the normal distribution analysis of the data. As can be seen from Figure 4, the data show a homogeneous distribution on a line. There is no excessively concentrated distribution to the right and left of the line. Before performing the analysis, an idea arises that such a distribution can be expected to show a normal distribution.

Table 1. SCC for the first month and second month

SCC for the first month	SCC for the second month
175000	150000
160000	180000
100000	10000
25000	85000
19000	13000
30000	10000
45000	15000
185000	190000
90000	170000
70000	185000

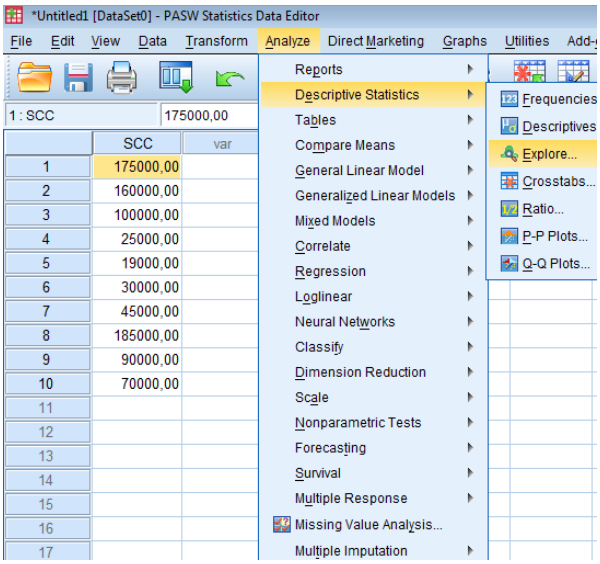

Figure 1. Entering the data into the Spss program

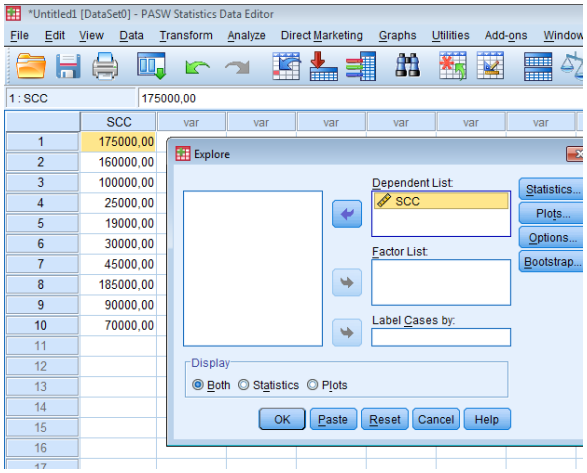

Figure 2. Moving the dependent variable to the dependent list field

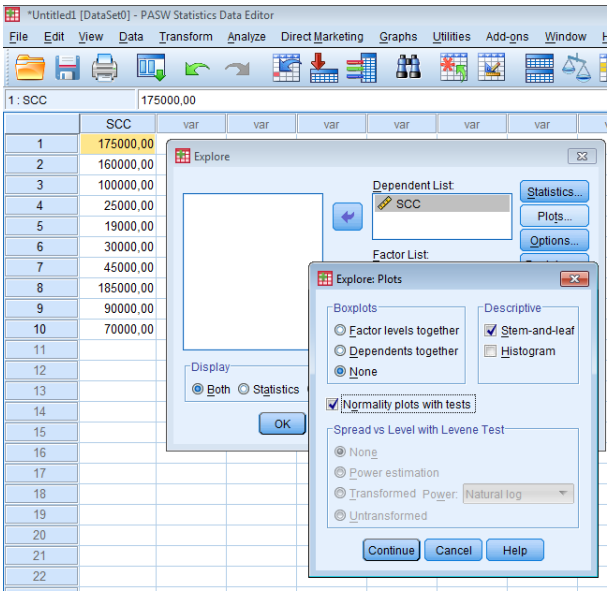

Figure 3. Using the plots window for normality testing

In the Explore window, the text SCC is moved to the section labeled Dependent List (Figure 2).

When Figure 5 is examined, larger variations in the distributions are noted compared to the previous figure. The idea that the large variation seen in Figure 5 may negatively affect the normal distribution for the second month data arises. However, the definitive result will emerge with the analysis to be performed. The benefit of scatter plots is that they enable visual detection of data that may affect the normal distribution in the data set and enable seeing where absurd data falls around the line [15].

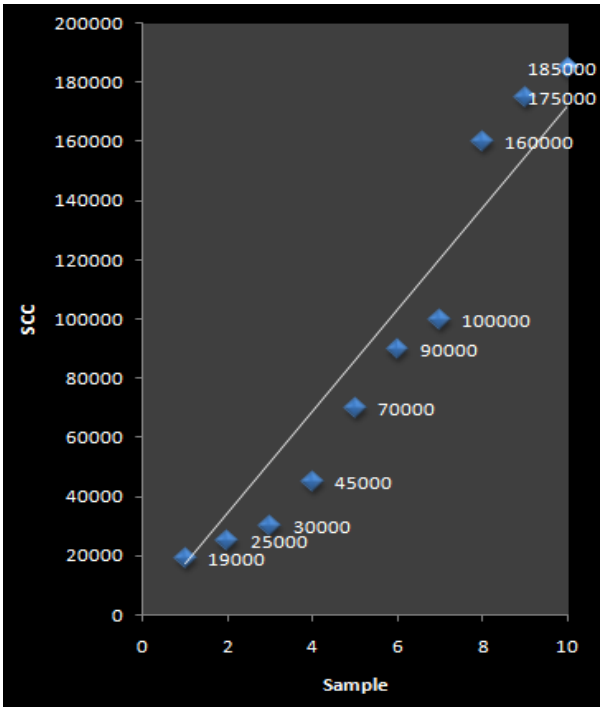

Figure 4. Scatter plot for SCC in first month data

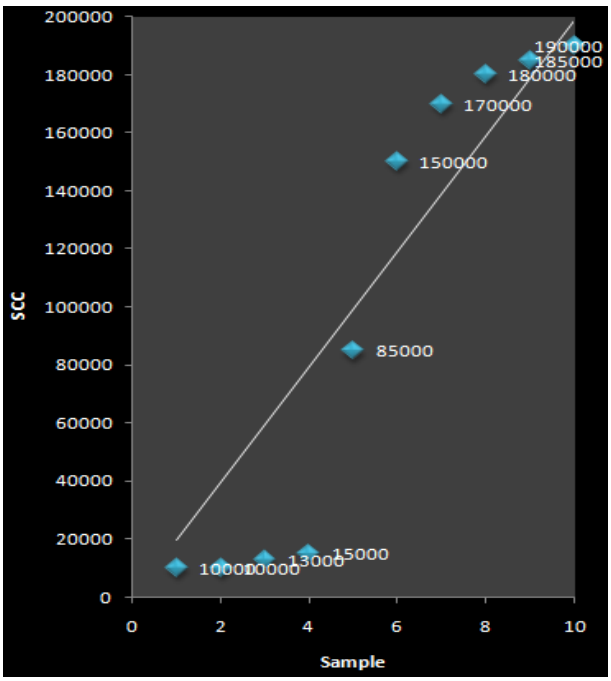

Figure 5. Scatter plot for SCC in second month data

It is noteworthy that the data in the first month data were distributed at narrower angles on the line. However, as seen in Figure 5, the data in the second month were distributed at wider angles on the line. This distribution can be expected to negatively affect the normal distribution. Because when the data is not arranged at equal distances and in equal numbers on the right and left of the line, this can negatively affect the normal distribution. However, as stated, in order to say this with certainty, the normal distribution test should be performed and comments should be made [16].

Although it is possible to bring the data closer to a normal distribution by removing the data that is farthest from the truth from the data set, this may not always be possible. Because while removing absurd data from some data sets does not negatively affect the structure of the data set, this is not possible in some data sets [17]. The removed data may have a feature that will disrupt the purpose of the hypothesis [18]. For example, in cases where all the examples of a population must be in the data set, such a removal is not possible. When the data is removed, the integrity of the population may be disrupted [19, 20]

Table 2 shows the normal distribution analysis results for the SCC values of the first month.

If less than 2000 data are used in the data set, the Sig value in the section labeled Shapiro Wilk should be taken into consideration. Since the current data set consists of 10 data in total, the Sig value in the section labeled Shapiro Wilk will be taken into account [21]. Since the sig value (0.156) found as a result of the research is above the value of 0.05, known as the significance level limit (0.05<0.156), it can be assumed that the data for the first month shows a normal distribution. The normality test was applied to the second month data in the same way.

As a result of the analysis shown in Table 3, it is concluded that the data for the second month does not show a normal distribution, since the sig value of 0.011 in the Shapiro-Wilk household is below the value of 0.05 (0.011<0.05). Therefore, since the first month data show a normal distribution, if a comparison is to be made with a certain reference value, one-sample t-test, one of the parametric test methods, should be applied, whereas since the second-month data does not show a normal distribution, the Wilcoxon One-Sample Sign Rank Test, which is the non-parametric equivalent of the one-sample t-test, should be applied [22, 23]. As mentioned before, absurd data in the second month data can be eliminated and brought closer to normal distribution. When the data approaches normal distribution as a result of the analysis to be made after this, parametric test methods can be used. However, this situation is not always desired. In addition, even if this method is desired, using missing data in the data set may not always comply with the hypothesis. For such reasons, it would be more meaningful to apply non-parametric data analysis instead of eliminating absurd data from the data set. Sometimes, when a data that should not be removed from the data set is removed, incorrect results that do not comply with the research hypothesis can be encountered [24].

One is curious about the results that will be seen when the second month data, which does not show a normal distribution, is analyzed with one sample t test. For example, a dairy farm does not want the somatic cell count to be over 20000. It is desired to know whether the second month milk data exceeds the limit reference value of 20000. When we look at Table 4, we see that there is a statistically significant difference ($p = 0.012$) when we compare the mean value (100800) with reference value (20000). The dairy farm sees the unwanted level of SCC data in these results. However, it would be wrong to apply this method since the data does not show a normal distribution.

Now, Wilcoxon one simple sign rank test is applied to the same data. Looking at the analysis results given in Table 5, when the numbers forming the data set are compared on a median basis rather than an average, there is no statistical difference compared to the reference value ($p = 0.074 > 0.05$). Since the normal distribution is disrupted because the operating data shows great variation, there is no negative effect compared to the reference value of 20000 in terms of somatic cell numbers. In other words, the dairy farm did not encounter any negative results in the 2nd month compared to the reference limit value (20000). As can be seen, very opposite results were obtained from the two analyses. Accordingly, an analysis performed without knowing whether the data complies with normal distribution may cause information pollution.

As can be seen from the research results, since existing data sets in the field of microbiology may tend to show large variations, it should be tested whether the data show normal distribution before determining the statistical analysis method [25, 26]. Non-parametric test methods should be applied to data that do not show normal distribution [27]. Interpreting according to rank values is a method used in nonparametric tests and these tests are used in some research [28, 29].

Table 2. Normality test result for SCC in the first month

	Kolmogorov-Smirnov[a]			Shapiro-Wilk		
	Statistic	df	Sig.	Statistic	df	Sig
SCC	.164	10	.200*	.887	10	.156

Table 3. Normality test result for SCC in the second month

	Kolmogorov-Smirnov[a]			Shapiro-Wilk		
	Statistic	df	Sig.	Statistic	df	Sig.
SCC	.253	10	.070	.790	10	.011

Table 4. One-sample t-test analyses results

	N	Mean	Std. Deviation	Std. Error Mean
SCC	10	100800.00	81879.0	25892.42

One-Sample Test

	Test Value = 20000					
	t	df	Sig. (2-tailed)	Mean Difference	95% Confidence Interval of the Difference Lower	Upper
SCC	3.12	9	.012	80800.00	22227.2	139372.7

Table 5. Wilcoxon one-sample sign rank test analyses results

Ranks

		N	Mean Rank	Sum of Ranks
Reference value - SCC	Negative Ranks	6[a]	7.50	45.00
	Positive Ranks	4[b]	2.50	10.00
	Ties	0[c]		
	Total	10		

a. Referencevalue < SCC
b. Referencevalue > SCC
c. Referencevalue = SCC

Test Statistics[b]

	Referencevalue-SCC
Z	-1.785[a]
Asymp. Sig. (2-tailed)	.074

a. Based on positive ranks.
b. Wilcoxon Signed Ranks Test

In this research, while the first month data set showed a normal distribution, the second month data set did not show a normal distribution. Therefore, it is seen from the research results that the statistical methods to be applied for each month should be different. Before using parametric statistical methods such as t-test and analysis of variance, which compare the means of treatment groups, it must be tested whether the data sets of the treatment groups show normal distribution [30-32]. In order to obtain reliable information, research must be planned correctly and the data obtained must be tested according to appropriate analysis methods [33-35]. But, it is noteworthy that in some studies there are major errors in the collection and analysis of data [36, 37]. To prevent information pollution, care should be taken during the planning and analysis stages [38, 39]. Otherwise, there may be problems in the publication phase of research articles. Even if such studies are published, they may cause negativities in the academic life of the researchers because they create information pollution [40].

4. Conclusions

This study is of great importance in terms of emphasizing the importance of the normal distribution test and also showing how determining the wrong statistical method can negatively affect the research results. According to the results of the current study, in all studies where the parametric test method is applied, whether the data are suitable for normal distribution should be questioned before determining the current statistical method. Unfortunately, in many studies where parametric data analyses are used in the literature, it is not stated whether the normal distribution test is applied to the data. Studies where parametric data analyses are used and whether it is not known whether the data are suitable for normal distribution should not be accepted in journals. Authors should be asked whether they have applied the normal distribution test in their studies and whether they have determined the analysis method they have chosen according to the normal distribution test result. Studies where parametric data analyses are applied to data that are not known to meet the normal distribution condition should be viewed with suspicion and should never be accepted for publication in journals. This study will be a guide in determining the correct statistical method in future research.

Declaration

The author declared no potential conflicts of interest with respect to the research, authorship, and/or publication of this article. The author also declared that this article is original, was prepared in accordance with international publication and research ethics, and ethical committee permission or any special permission is not required

Author Contributions

Murat Çimen: Obtaining data, analysis of data, article writing, literature review, editing

References

1. Al-Eideh, B.M., *Statistical methods for business data analysis using spss.* 2016, Scholars Press. ISBN-10: 9783639864892.
2. Flora, D.B., *Statistical methods for the social and behavioral sciences: a model based approach.* 2018, Pp. 472. Sage publications. ISBN-10: 1446269833.
3. Thalberg, M., *Statistical analysis: Methods and techniques for data interpretation.* 2024, Independently pub. ISBN-13979-8325377037:.
4. Padem, H., A. Göksu, and Z. Konaklı, A*raştırma*

yöntemleri. Spss uygulamalı. 2012, International Burch University. Sarajevo. ISBN: 978-9958-834-04-2.

5. Borman, D., *Statistics 101: from data analysis and predictive modeling to measuring distribution and determining probability, your essential guide to statistics.* 2018, Simon and Schuster Pub. Pp 240. ISBN:1507208189, 9781507208182.
6. Sumpter, D., *Four ways of thinking: statistical, interactive, chaotic and complex.* 2023, Allen Lane pub. Pp. 336. ISBN-10:0241624169.
7. Jung, Y.M., *Data analysis in quantitative research*. 2018, In: Liamputtong, P. (eds) Handbook of research methods in health social sciences. Springer, Singapore. ISBN: 978-981-10-5251-4.
8. Ott, R. and M. Longnecker, *An introduction to statistical methods and data analysis.* 2021, Cengage Learning. 7 th Ed. Pp. 1296. ISBN-10: 0357670620.
9. Mahsin, M.. *Data analysis techniques for quantitative study*. 2022, In: Islam, M.R., Khan, N.A., Baikady, R. (eds) Principles of social research methodology. Springer, Singapore. ISBN: 978-981-19-5441-2.
10. Çimen, M., *Fen ve sağlık bilimleri alanlarında spss uygulamalı veri analizi.* 2015, Palme Yayıncılık, Yayın No: 905, ISBN: 978-605-355-366-3. Sıhhıye, Ankara.
11. Das, K., *A brief review of tests for normality.* American Journal of Theoretical and Applied Statistics, 2016. **5**(1): p.5-12.
12. Hatem, G., J. Zeidan, and M. Goessens, *Normality testing methods and the importance of skewness and kurtosis in statistical analysis*, BAU Journal Science and Technology, 2022. **3**(2): p. 1-7.
13. Huynh, K., *Getting started with spss: an introduction for beginners.* 2024. Independently pub. First Ed. P 174. ISBN-13:979-8878835145.
14. Jung, Y.M., *Data analysis in quantitative research*. 2019, In: Liamputtong, P. (eds) Handbook of research methods in health social sciences. Springer, Singapore. ISBN: 978-981-10-5251-4.
15. Rutheford, A., *Statistics for the rest us: mastering the art of understanding data without math skills (advanced thinking skills).* 2023, Independently pub. Pp 152. ISBN-13:979-8391345831.
16. Frost, J., *Introduction to statistics: an intuitive guide for analyzing data and unlocking discoveries.* 2020, Statistics by jim publishing. Pp 255. ISBN-101735431109:.
17. Theobald, O., *Statistics for Absolute beginners (Secon Edition) (Al data sciences, python&statistics for beginners*. 2020, Independently pub. Pp 157. ISBN-13:979-8654976123.
18. Rumsey, D.J., *Statistics al in on efor dummies.* 2022, For dummies pub.Pp 560. ISBN-101119902568: .
19. Honner, P., *Painless statistics (barron's painless).* 2022, Barrons educational services. Pp 320. ISBN-10: 1506281583.
20. Ural, A. and İ. Kılıç, *Bilimsel araştırma süreci ve spss ile veri analizi.* 2013, 4.Baskı. 296 Sayfa. Detay Yayınları. ISBN:978-975-8326-17-X.
21. Newbold, P., W. Carlson, and B. Thorne, *Statistics for business and economics.* 2012, Eighth Edition. Pearson Education. ISBN10 : 0273767062.
22. Can, A., *Spss ile bilimsel araştırma sürecinde nicel veri analizi.* 2014, 3. Baskı. 396 Sayfa. Pegem Yay. ISBN: 978-605-364-448-4.
23. Ganesan, R. and P.V. Sreinvasalah, *Textbook of statistics.* 2015, First Edition. Write And Print Publications. ISBN-10: 9789384649050.
24. Karagöz, Y., *Biyoistatistik.* 2014, Nobel Yay. No: 1075. 1. Basım. 733 sayfa. ISBN: 978-605-133-979-5.
25. Anonymous., *Digital literacy training. Spss advanced significance testing.* 2019, ANU Library. Pp.20. Available from: https://services.anu.edu.au/files/SPSSAdvancedSignificance Testing.pdf .
26. Rutherford, A. and J.H. Kim, *The art of statistical thinking: detect misinformation, understand the world deeper, and make better decisions. (Advanced Thinking Skills).* 2022, First Edition. ARB Publications. ISBN: 9798358180710.
27. Sheskin, D.J., *Handbook of parametric and non-parametric statistical procedures.* 2011, Fifth Edition. Taylor and Francis Group. 6000 Broken South Parkway NW Suite 300 Boca Raton. FI. 33487-2742. ISBN: 978-1-4398-5801-1.
28. Rezai, A. and S. Jalal, *Investigating the causes of delay and cost overrun in construction industry*. International Advanced Researches and Engineering Journal, 2018. **2**(2): p. 75-79.
29. Mamenko, 0. and S. Potiannyk, *Rank non-parametric correlation analysis of indicators of heavy metal transition from blood to cow's milk to assess its environmental safety.* Scientific Horizons, 2021. **24**(5): p.35-45.
30. Singh, J.P, *Statistical methods in public health*. 2022, In Gupta S.D. (eds) health care system managements. Pp. 85-127. Springer. ISBN: 978-981-19-3076-8.
31. Yuan, I., A.A. Topjian, C.D. Kurth, M.P. Kirschen, C.G. Ward, B. Zhang, and J.L. Mensinger, *Guide to the statistical analysis plan.* Pediatric Anesthesia, 2019. **29**(3): p.1-15.
32. Jebb, A.T., S. Parrigon, and S.E. Woo, *Exploratory data analysis as a foundation of inductive research.* Human Resource Management Review, 2017. **27**(2): p.265-276.
33. Mehta, S., *Statistics topics.* 2014, Kindle Store. Kindle Edition. p. 161. ASIN : B00KVPB8H8.
34. Dean, S. and B. Ilowsky, *Introductory statistics.* 2016, Open stax pub. p. 907. ISBN-10: 1938168208.
35. Hill, T. and P. Lewicki, *Electronic statistics textbook*. 2013, Stat soft inc. p. 800. ISBN-10: 1884233597.
36. Salcedo, J. and K. McCormick, *SPSS statistics workbook for dummies.* 2023, Wiley Pub. p. 336. ISBN: 97813941563 06,1394156308.
37. Salkind, N.J., *Statistics for people who (think they) hate statistics.* 2010, Sage Pub. p. 399. ISBN: 9781412971027.
38. Knap, H., *Introductory statistics using spss*. 2016, Sage Pub. p. 312. ISBN-10: 1506341004.
39. Schmuller, J., *Statistical analysis with R for dummies.* 2017, For dummies pub. First Ed. P 464. ISBN-10:9781119337065.
40. Gentle, E.J., *Theory of statistics*. 2013, Pub. L. No. 94-553, 90 Stat. 2541. p. 917. ISBN:n/a.

Available online at www.dergipark.org.tr/en

INTERNATIONAL ADVANCED RESEARCHES and ENGINEERING JOURNAL

Journal homepage: www.dergipark.org.tr/en/pub/iarej

e-ISSN: 2618-575X

International Open Access

Volume 08
Issue 03

December, 2024

Research Article

Investigation of failure loads of adhesive bonded and induction welded joints on similar and dissimilar substrates

Fatih Huzeyfe Öztürk [a,*]

[a]*Industrial Design Engineering Department, Karabük University, Karabük, 78050, Turkey*

ARTICLE INFO

Article history:
Received 16 August 2024
Accepted 26 November 2024
Published 20 December 2024

Keywords:
Additive manufacturing
Adhesive bonding
Failure
Induction welding load

ABSTRACT

This study investigates the effect of adhesive bonding and induction welding on the maximum load of joints of Additive Manufacturing (AM) printed thermoplastic substrates with steel substrates. DINC75 was used as steel substrate and polylactic acid (PLA) as thermoplastic substrate. Fast-curing cyanoacrylate adhesive was used as adhesive. As the novelty of the study, there is a type of joint formed by induction welding of 3D printed substrates with steel has not been found in the literature. Single lap joint (SLJ) and double lap joint (DLJ) geometries were selected as joint geometries. The maximum load of joints was determined by applying tensile test to the joints. As a result, all the joints showed no adhesive failure and also the induction welded joints showed 27.51% and 65.49% increase in failure load compared to adhesive joints for SLJ and DLJ, respectively. The maximum load of joint of 9.40 kN was obtained for the DLJ geometry prepared by induction welding. Induction welding was found to be a good alternative to adhesive bonded joints.

1. Introduction

Adhesive bonding is a critical technique utilized in various fields such as dentistry, materials science, and engineering due to its ability to establish robust and enduring bonds between different materials. These joints offer several advantages over traditional bonding methods, including a more uniform stress distribution along the bonded area, leading to enhanced structural integrity and load-bearing capacity of Additively manufactured components [1]. Furthermore, these joints contribute to weight reduction in structures by eliminating the need for mechanical fasteners, such as rivets and bolts, thereby enhancing the overall efficiency of the bonded component [2]. The use PLA in AM has facilitated the creation of complex, customized structures with unique properties.

Zhang et al. [3] investigated surface modification approaches to enhance the lap shear strength of epoxy bonded joints and highlighted the significance of optimizing the crosslinking structures within the polymeric layer to augment the overall bond strength. This research emphasizes the crucial importance of surface treatments in achieving strong adhesive bonded joints in polymer additive manufacturing applications. Golewski et al. [4] conducted an empirical investigation on single lap hybrid joints composed of 3D printed polymer and aluminum substrates. They offered valuable perspectives on the mechanical behavior and performance of hybrid joints and stressed the significance of comprehending the interplay between diverse materials in adhesive bonded structures. Silva et al. [5] investigated the joining of additive manufacturing components via “mortise and tenon” joints, demonstrating the feasibility and deformation mechanics of this new joining process. By investigating the deformation mechanics of single lap joints in additive manufacturing, this study contributes to improving the design and fabrication of complex structures using adhesive bonded joints.

Induction welding of steel with thermoplastic materials is an advanced joining technique that has gained significant interest across various industries, particularly in aerospace and automotive applications. Two thermoplastic parts, called substrates, can be joined together using this method. This can be done with resistance welding, ultrasonic welding, and most importantly, induction welding [6,7]. Induction welding is recognized for its speed, cleanliness, and contact-free nature, reducing welding time and eliminating the need for mechanical fastening methods like rivets and bolts,

* Corresponding author. Tel.: +90-370-418-9020 ; Fax: +90-370-418-9419 .
E-mail addresses: fhozturk@karabuk.edu.tr *(Fatih Huzeyfe ÖZTÜRK).*
ORCID: 0000-0001-8025-8236 *(Fatih Huzeyfe ÖZTÜRK).*
DOI: 10.35860/iarej.1534565

thereby preventing weight increase in the final joint [8]. This technique has been acknowledged for its potential in cost reduction and environmental impact mitigation while maintaining joint quality at acceptable levels, making it a promising solution for various applications, including aerospace technologies [9]. Induction welding is particularly suitable for large-scale applications in industries like aerospace, where it is employed to efficiently and effectively join thermoplastic composite structures [10]. The automated nature of the technology and its ability to produce high-quality joints make it a preferred choice for welding steel with thermoplastic materials in various structural components. The process of induction welding is highly automated and suitable for long production runs, making it a preferred choice for welding steel pipes and other components in industrial settings [11]. Also, ongoing improvements in induction welding technology have worked on improving the mechanical performance of joints made of reinforced plastics. This shows that efforts are still being made to improve the quality and dependability of welded joints [12].

In the realm of thermoplastic composites, induction welding offers a rapid and reliable method for joining different materials, including metals like steel, to create robust and durable structures [13]. The precise control of through-thickness temperature distribution during induction welding of carbon composite aerospace parts showcases the precision and control achievable with this technique, ensuring uniform heating and high-quality joints [14]. Thorough research has contrasted induction welding for thermoplastic composites with other welding methods such as ultrasonic and resistance welding, emphasizing its distinct benefits and abilities in joining complex materials [15]. Additionally, the use of induction welding for repairing impacted thermoplastic composite laminates underscores its versatility and effectiveness in maintenance and repair applications [16]. Furthermore, researchers have explored the use of advanced techniques like material extrusion and friction stir welding to create single lap joints between polymers and metals [17,18]. These methods offer unique advantages in terms of joint strength and integrity, especially when joining dissimilar materials like polymer and aluminum alloy. By leveraging these innovative joining techniques, manufacturers can achieve robust and durable single lap joints in polymer additive manufacturing applications.

The utilization of induction welding in joining thermoplastic composites with steel has been extensively researched and developed. The utilization of stainless steel mesh as a susceptor in thermoplastic composite induction welding showcases the adaptability and efficiency of this method [19]. Induction welding for thermoplastic composite materials is commonly treated as a complex problem involving multiple physical factors. Researchers use finite element methods and process modeling to study and improve the performance and efficiency of this process [20]. Novel heating components, such as conductive films made of carbon nanofibers coated with metals like silver or nickel, have been created for use as heating elements in the induction welding of thermoplastic composites. This advancement significantly improves the capabilities and potential uses of this technology [21].

In conclusion, induction welding of steel with thermoplastic materials is a cutting-edge joining technique offering numerous advantages in terms of efficiency, reliability, and joint quality. The literature highlights the potential of induction welding in creating robust joints between thermoplastic composites and metals, especially in applications where weight reduction and structural integrity are critical, such as in the aerospace and automotive industries. However, previous studies have generally used either a conductive composite or a conductive part (susceptor) when induction welding a metal plate with a thermoplastic material. In this study, as different from the literature, steel and thermoplastic material were joined by adhesive bonding and induction welding method. DINC75 was used as steel substrate and 3D printed PLA was used as thermoplastic substrate. SLJ and DLJ geometries were selected and the effect of joining type on failure load was investigated. The maximum load of joint values was determined by uniaxial tensile test method.

2. Experimental Procedures

2.1 Materials

In this study, a series of controlled experiments were conducted to assess the impact of induction welding and adhesive bonding technology on the bond strength of joints. The dissimilar joints considered for this study are 3D printed and DIN C75 high-strength steel substrates. Material Extrusion technology and PLA thermoplastic filament (Porima industrial, Yalova, Turkey) were chosen as the material for the 3D printed substrates. 3D printing process was performed using a ZAXE X1 3D printer (ZAXE, Istanbul, Turkey) equipped with a 0.4 mm nozzle [22]. The printing parameters were set using the XDesktop slicing program based on the filament manufacturer's data sheet. Bed and extrusion temperatures were 60°C and 210°C respectively [23], with on-edge orientation and tensile load direction [24]. The mechanical properties of PLA and DIN C75 are given in Table 1. A cyanoacrylate type adhesive manufactured by VODABOND (Taiwan) with fast-curing properties was used to produce the bonded joints. Furthermore, the adhesive was chosen as it is suitable for joining polymer materials with low surface energy and its fast-curing property is similar to the joint times produced by induction welding.

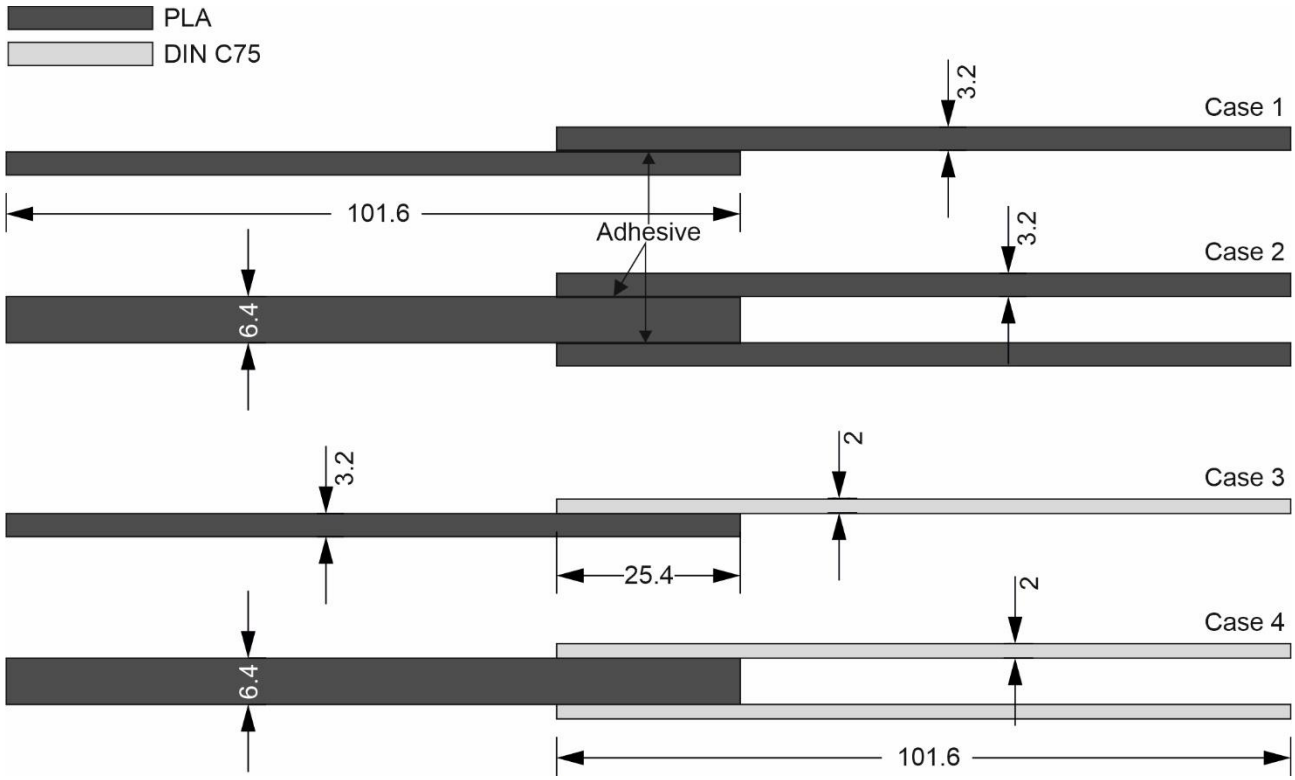

Figure 1. All joint configurations (dimensions in mm)

Table 1. Mechanical properties of substrates [25,26]

Properties	PLA	DIN C75
Young's modulus (MPa)	2850	198300
Tensile strength (MPa)	56	1413

Table 2. Properties of used adhesive

Chemical Type	Ethyl Cyanoacrylate
Components	One part -
Color	Slightly cloudy
Relative density (g/cm$^{3)}$	1.1
Specific Gravity @ 25ºC	1.05
Viscosity (cP) (at 1.5 rpm)	112000
Tensile Strength (MPa) [27]	20
Cure speed (at sec.)	5-120

The properties of the adhesive according to the technical data sheet obtained from the supplier are presented in Table 2.

2.2 Experimental Study

In this study, four joint configurations were investigated. These are the bonded SLJ and DLJ, induction welding SLJ and DLJ (Figure 1). SLJs and DLJs are fundamental types of adhesive joints that play crucial roles in various applications. SLJs are widely used and researched due to their simple geometry and structural efficiency [28]. They are preferred for their reliability and ease of implementation, making them a common choice in adhesive bonding [29]. On the other hand, DLJs offer specific advantages and are commonly used in thin structures under low running loads [30]. PLA+PLA in cases 1 and 2, PLA substrates in cases 3 and 4 were joined by induction welding to DINC75 substrate. SLJ and DLJ geometries are determined according to ASTM D3163-1 and ASTM D3528-96 respectively [31,32]. The overlap length and the thickness of the bond line were set similarly for all the prepared cases.

PLA+PLA joints (Case 1-2) were degreased by wiping with isopropyl alcohol along the tensile load direction prior to joining. Subsequently, adhesive was applied to the cleaned adhesion area, the other substrate was placed, and the joints were prepared with the use of metal clamps. The overlap length of the joints was measured with a digital caliper to check the dimensional accuracy. The technique used in cases 3 and 4, based on induction welding, is shown schematically in Figure 2.

The device represented in Figure 2 is a 30 KHz 50 kW induction machine manufactured by ONX (ONX, Turkey). The coil type with a diameter of 50 mm and a length of 65 mm was used as a bobbin on the device. The bobbin coil is a crucial component in induction welding systems, significantly impacting the efficiency and effectiveness of the heating process. The design and characteristics of the coil play a vital role in various aspects of the heating operation. For example, the use of a bobbin coil can result in improved temperature distribution, reduced process time, and enhanced heating efficiency in induction welding applications [33].

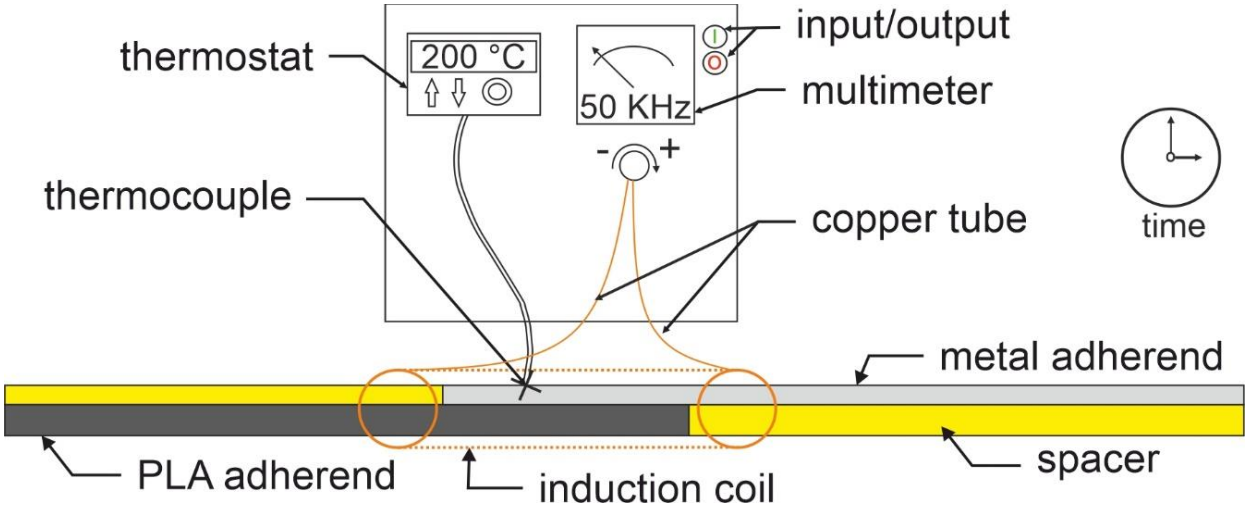

Figure 2. Schematic representation of induction welding technique

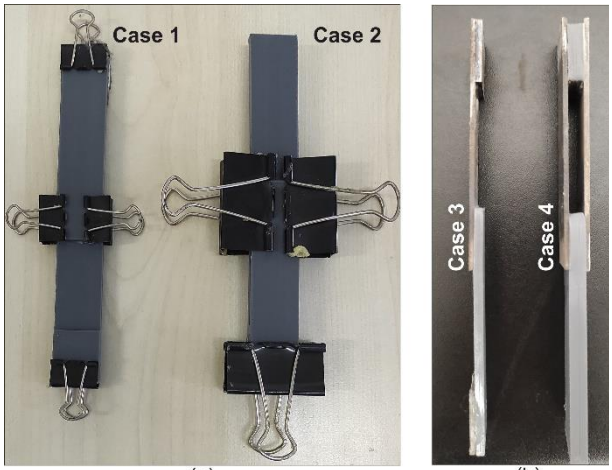

Figure 3. Produced specimens a) adhesive bonded and b) induction welded

Digital Thermostat (DT-48EM) thermostat was used to control the temperature on the substrate during the induction welding process. Prior to the bonding process, metal surfaces were prepared by sandblasting with silicon carbide and PLA surfaces were wiped with isopropyl alcohol. Induction welding was performed at 200 °C since the melting (*Tm*) and glass transition temperature (*Tg*) of PLA are 155-170 °C and 55-60 °C, respectively [34,35], and the decomposition temperature starts at 300 °C and ends at 375 °C [36]. Metal and polymer substrates were placed in the coil using a non-conductive mold. Subsequently, the joint was removed from the coil and the mold was applied pressure. The joints produced by adhesive bonding technology and induction welding are shown in Figure 3.

Mechanical characterization was performed under displacement control and at a test speed of 1 mm/min using a Shimadzu AG-50X (Kyoto, Japan) universal testing machine. Each characterization test was repeated at least three times, and load-displacement curves were acquired for each configuration.

3. Result and Discussion

3.1 Fracture Surface Analysis

The fracture surfaces of all joint cases are shown in Figure 4. When Figure 4 is considered, it is seen that cohesive damage is observed for the adhesive joints (Case 1 and 2). In the case of cohesive failure, it is understood that the adhesive has reached the maximum load it can carry [24]. When Case 3 and 4 are examined, it is clear that the damage is caused by the rupture of the thermoplastic material. In the case of adhesive joint and induction welding, the absence of adhesion failure showed that adequate surface preparation was carried out.

The cross-sections and top views of the damage areas in the induction welded cases were observed using an ISM-PM 200 SA digital microscope. Figure 5 shows the damage details of the joint in Case 3. When Figure 5 is examined, it is seen that the adhesion of the interface between DIN C75 and PLA is higher than the strength of PLA and therefore the damage is caused by PLA. In addition, when the interface was examined, it was observed that the bottom layer of PLA melted and bonded to the DINC75 surface. PLA has a brittle nature, which can lead to premature failure under stress. This brittleness is particularly evident in 3D printed samples where the layer-by-layer structure can form weak interlayer bonds. The mechanical performance of PLA parts is significantly affected by the fracture mode, which can be categorized as inter-layer and intra-layer fractures [37]. Inter-layer fractures occur due to poor bonding between layers, while intra-layer fractures are related to the intrinsic properties of the material [38]. As seen in Figure 5, intra-layer damage type was observed in PLA for Case 3.

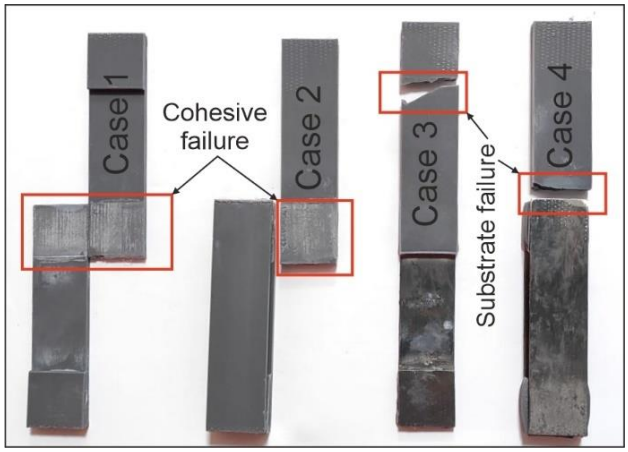

Figure 4. Fracture surface of all cases

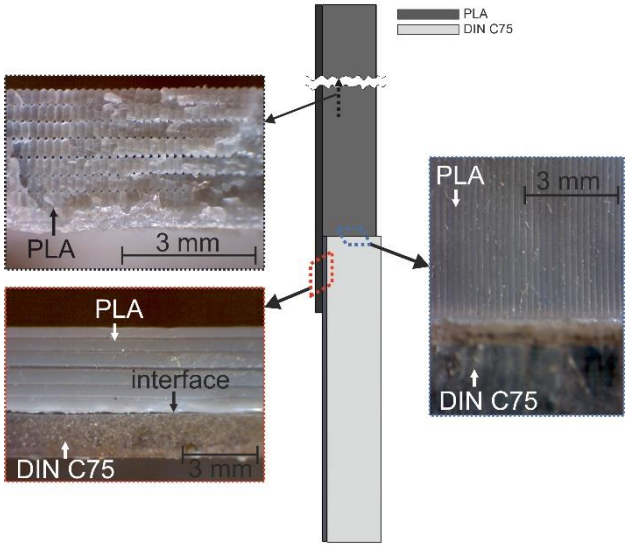

Figure 5. Fracture detail of Case 3

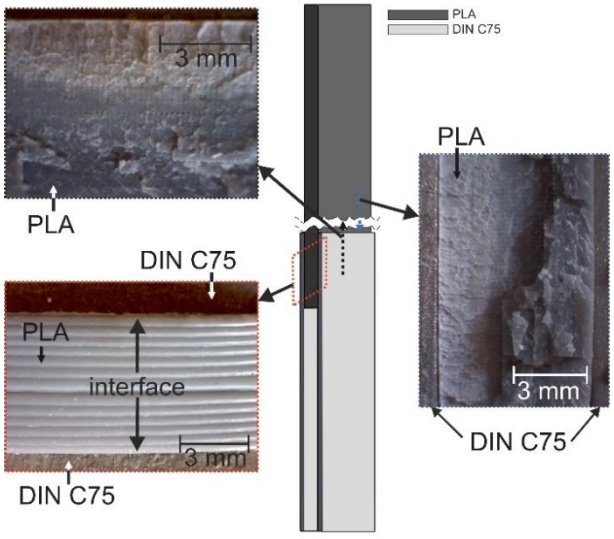

Figure 6. Fracture detail of Case 4

Figure 6 shows the damage states and detailed microscope images of the induction welded joint after the tensile test for Case 4. When using the SLJ geometry (Case 3), the induction coil only affects the single metal sheet. However, in DLJ geometry, in order to determine the effect of the induction process on the PLA sheet between two DIN C75 sheets, DLJ geometry was also preferred. As can be seen from Figure 6, the interface formed between PLA and two DIN C75 plates was formed by the melting of the top and bottom layers of PLA, and since the damage was caused by the PLA specimen, the strength of this interface was higher than the strength of PLA. Similarly, in Case 4, the damage of PLA was observed as intra-layer damage.

3.2. Tensile test results

Figure 7 shows the load-displacement curves of (Case 1 and 2) joined with adhesive. When these cases are compared, it is seen that Case 2 reaches the highest load-displacement value. Case 1 (i.e. the SLJ) rotates and suffers early damage due to significant joint rotations at the overlap edges [37,39]. This is due to the load asymmetry of Case 1 [40]. On the other hand, in Case 2 (i.e. DLJ), the rotation of the joint is eliminated as the load is symmetrically applied to the joint. Therefore, it has a higher load carrying capacity than Case 1 [41,42].

Figure 8 shows the load-displacement graphs of Case 3 and Case 4 prepared by induction welding method. Similar load-displacement behavior was obtained with the load-displacement behavior of adhesive joints. It was found that case 4 carried up to twice the load of case 3.

The failure load values of all prepared joints (adhesive and induction welded) are given in Figure 8. When Figure 9 is examined, it is seen that induction welding reaches the highest failure load in all joint types. Induction welded joints increased the failure load by 27.51% for SLJ and 65.49% for DLJ when compared to adhesively bonded joint. The reason that induction welding reaches a higher failure load than adhesive joints is due to the fact that, as previously outlined in Section 3.1, the maximum load that the adhesive can carry is reached in the case of an adhesive joint. Once the adhesive has exceeded the maximum load that it is capable of carrying, the damage is called cohesive damage. This damage means that the strength of the PLA is greater than the strength of the adhesive [39]. For this study, it can also be said that the interface formed between PLA and DIN C75 in the joints produced by induction welding (Case 3 and Case 4) is stronger than the adhesion strength and the PLA.

3. Conclusions

The effect of adhesive bonding and induction welding on the maximum load of joint of PLA+PLA and PLA+DINC75 substrates in SLJ and DLJ geometries was investigated. PLA substrates were produced using 3D printing technology. The impact of adhesive bonding and induction welding on the maximum load of joint was compared after uniaxial tensile testing of the joints. The main results obtained are listed below:

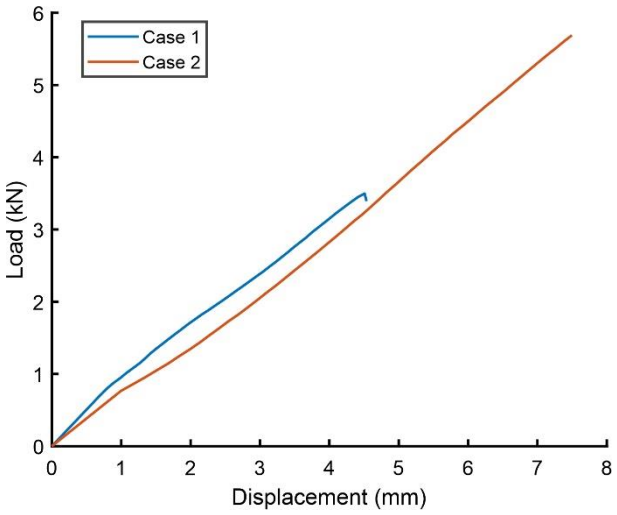

Figure 7. Load-displacement of adhesive bonded cases 1 and 2

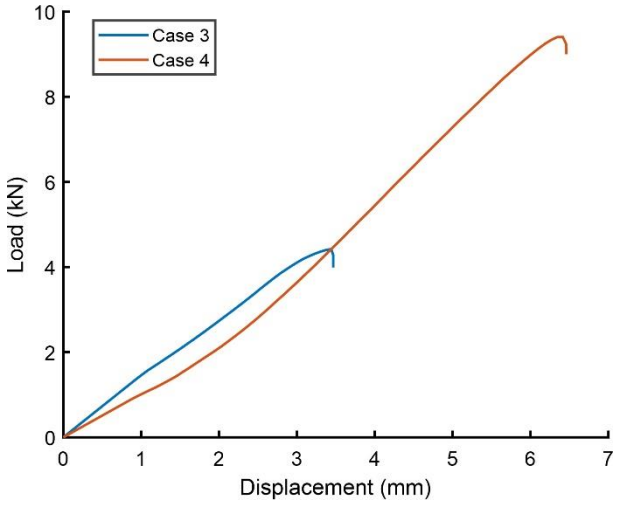

Figure 8. Load-displacement of adhesive bonded cases 3 and 4

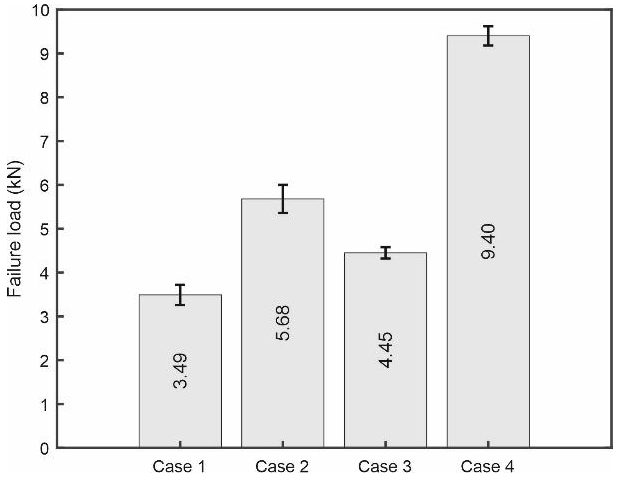

Figure 9. Comparison of failure load of all cases

- The maximum load of joint of adhesive bonding on PLA specimens was 3.49 kN and 5.68 kN for SLJ and DLJ geometries, respectively. Cohesive damage was observed in the adhesive joints (Case 1 and Case 2).
- The maximum load of joint of induction welding technology on PLA+DINC75 specimens was 4.45 kN for SLJ and 9.40 kN for DLJ. The induction welding method resulted in 27.51% and 65.49% increase in failure loads for SLJ and DLJ, respectively, compared to the adhesively joint. Induction welded joints (Case 3 and Case 4) showed substrate damage. In addition, the damage to the substrate was caused by the fact that the strength of the interface formed after the induction welding process between DIN C75 and PLA substrates was higher than the strength of PLA.
- No adhesive failure was observed in all joint configurations. This indicated that the two methods were used correctly and adequate surface preparation was performed.

These results suggest that induction welding is an important alternative to adhesively joining polymeric materials to steel.

Declaration

The author declared no potential conflicts of interest with respect to the research, authorship, and/or publication of this article. The author also declared that this article is original, was prepared in accordance with international publication and research ethics, and ethical committee permission or any special permission is not required.

Author Contributions

F.H. Öztürk developed the methodology, performed the experiments, analyzed the results and wrote the manuscript.

References

1. Ayaz, Y., *Predicting the effect of adherend dimensions on the strength of adhesively bonded joints using M5P and M5 classifiers*. Journal of the Brazilian Society of Mechanical Sciences and Engineering, 2020. **42**(9): p. 465.
2. Kara, E., Kurşun, A., Haboğlu, M., Enginsoy, H., and Aykul, H., *Fatigue behavior of adhesively bonded glass fiber reinforced plastic composites with different overlap lengths*. Proceedings of the Institution of Mechanical Engineers, Part C: Journal of Mechanical Engineering Science, 2015. **229**(7): p. 1292–1299.
3. Zhang, Y., Hasegawa, K., Kamo, S., Takagi, K., and Takahara, A., *Surface Modification for Enhanced Lap Shear Strength of the Epoxy-Bonded Joints Consisting of Metallic Adherents and Similar/Dissimilar Materials*. ACS Applied Polymer Materials, 2023. **5**(7): p. 5381-5389.
4. Golewski, P., Nowicki, M., Sadowski, T., and Pietras, D., *Experimental Study of Single-Lap, Hybrid Joints, Made of 3D Printed Polymer and Aluminium Adherends*. Materials, 2021. **14**(24): p. 7705.
5. Silva, DF., Bragança, IMF., Alves, LM., and Martins, P a. F., *Joining by forming of additive manufactured 'mortise-and-tenon' joints.* Proceedings of the Institution of Mechanical Engineers, Part B: Journal of Engineering Manufacture, 2017. **233**(1): p. 166-173
6. Acaroğlu, M., Öz, Ö., and Öztürk, FH., *Eklemeli İmalat Yöntemi ile Üretilmiş PLA Levhaların Bağlantı Dayanımları: İndüksiyonla Isıtma ve Yapıştırıcı Teknolojilerinin Karşılaştırılması.* Afyon Kocatepe

Üniversitesi Fen ve Mühendislik Bilimleri Dergisi, 2024. **24**(4): p. 993–1004.
7. Farahani, RD., Janier, M., and Dubé, M., *Conductive films of silver nanoparticles as novel susceptors for induction welding of thermoplastic composites*. Nanotechnology, 2018. **29**(12): p. 1-9
8. Choi, B., Kang, CS., Yoo, MH., and Seo, MK., *Effect of Processing Parameters on Bonding Performance of a Carbon Fiber/Polyetheretherketone Thermoplastic Composite Prepared by Induction Welding*. Materials, 2023. **16**(11): p. 3954.
9. Katsiropoulos, CV., Pantelakis, S., Felline, F., Buccoliero, G., and Pappadà, S., *A holistic assessment of a stiffened panel production using a novel thermoplastic material and implementing the induction welding process*. Aircraft Engineering and Aerospace Technology, 2022. **94**(9): p. 1556-1566.
10. Brandon, S., Waruna, S., and John, T., E*ffect of Applied Pressure on Induction Welded Thermoplastic Composite Joint Quality and Performance*. SAMPE neXus, 2021. p. 1-13.
11. Boumerzoug, Z., and Lakhdari, L., *Effect of Heat Treatments on Microstructure and Mechanical Properties of Low Carbon Steel Pipes Welded by Induction Process*. Advanced Materials Research, 2014. **887–888**: p. 1301–1306.
12. Kagan, VA., and Nichols, RJ., *Benefits of Induction Welding of Reinforced Thermoplastics in High Performance Applications*. Journal of Reinforced Plastics and Composites, 2005. **24**(13): p. 1345-1352.
13. Schieler, O., and Beier, U., *Induction Welding of Hybrid Thermoplastic-thermoset Composite Parts*. KMUTNB International Journal of Applied Science and Technology, 2015. **9**(1): p. 27-36.
14. Schieler, O., Beier, U., and Mitscháng, P., *Control of the through-thickness temperature distribution in carbon composite aerospace parts during induction welding*. Journal of Thermoplastic Composite Materials, 2017. **31**(12): p. 1587-1608.
15. O'Shaughnessey, PG., Dubé, M., and Villegas, IF., M*odeling and experimental investigation of induction welding of thermoplastic composites and comparison with other welding processes*. Journal of Composite Materials, 2016. **50**(21): p. 2895-2910.
16. Modi, V., Bandaru, AK., Ramaswamy, K., Kelly, C., McCarthy, C., Flanagan, T., and O'Higgins, R., *Repair of Impacted Thermoplastic Composite Laminates Using Induction Welding*. Polymers, 2023. **15**(15): p. 3238.
17. Abdullah, IT., and Hussein, SK., *Shear strength and temperature distribution model of friction spot lap joint of high density polyethylene with aluminum alloy 7075*. International Journal of Structural Integrity, 2019. **10**(4): p. 469–483.
18. Alhmoudi, A., Sheikh-Ahmad, J., Almaskari, F., and Bojanampati, S., *Joining of polymer to metal using material extrusion additive manufacturing*. The International Journal of Advanced Manufacturing Technology, 2023. **129**(7–8): p. 3303–331.
19. Baek, IS., and Lee, SS., *A Study of Films Incorporating Magnetite Nanoparticles as Susceptors for Induction Welding of Carbon Fiber Reinforced Thermoplastic*. Materials, 2020. **13**(2): p. 318.
20. Guo, H., Pandher, J., Tooren, M van., and Wang, S., *Process Modelling of Induction Welding for Thermoplastic Composite Materials By Neural Networks*. SAMPE 2019-Charlotte, NC 2019. p. 15.
21. Farahani, RD., and Dubé, M., N*ovel Heating Elements for Induction Welding of Carbon Fiber/Polyphenylene Sulfide Thermoplastic Composites*. Advanced Engineering Materials, 2017. **19**(11): p. 1-10.
22. Öz, Ö., and Öztürk, FH., *Yazdırma Açısının 3B Yazıcıda Üretilen PLA Numunenin Mekanik Özellikleri Üzerine Etkisinin Deneysel ve Sonlu Elemanlar Metodu ile İncelenmesi*. Politeknik Dergisi, 2023. **26**(2): p. 529–540.
23. Parmaksız, F., Anaç, N., Koçar, O., and Erdogan, B., *Investigation of mechanical properties and thermal conductivity coefficients of 3D printer materials*. International Advanced Researches and Engineering Journal, 2023. **7**(3): p. 146–156.
24. Öztürk, FH., *Optimization of adherend thickness and overlap length on failure load of bonded 3D printed PETG parts using response surface method*. Rapid Prototyping Journal, 2024. **30**(8): p. 1579–1591.
25. Porima3D. P*orima Tecnical Data Sheet*. 2024. https://static.ticimax.cloud/42373/uploads/dosyalar/porima-tds-tr.pdf [accessed February 8, 2024].
26. Öz, Ö., and Özer, H., *An experimental investigation on the failure loads of the mono and bi-adhesive joints.* Journal of Adhesion Science and Technology, 2017. **31**(19–20): p. 2251–2270.
27. Metsan. *EMS FORCE PR-4066 Instant Adhesive.* 2024. https://www.metsan.gen.tr/tr/product/super-glues/engineering-super-glues/item/ems-force-pr-4066-super-glue-plastic-and-rubber/ [accessed October 15, 2024].
28. Moya-Sanz, EM., Iváñez, I., and García-Castillo, SK., *Effect of the geometry in the strength of single-lap adhesive joints of composite laminates under uniaxial tensile load.* International Journal of Adhesion and Adhesives, 2017. **72**: p. 23–29.
29. Santos, TF., and Campilho, RDSG., *Numerical modelling of adhesively-bonded double-lap joints by the eXtended Finite Element Method*. Finite Elements in Analysis and Design, 2017. **133**: p. 1–9.
30. Azeem, M., Irfan M, Masud M, Rehman GU, Ali H, Ali MU, Zafar, A., Niazi, UM., Rahman, S., Legutko, S., Petrů, J., and Kratochvíl, J., *Experimental and Numerical Investigation of Effect of Static and Fatigue Loading on Behavior of Different Double Strap Adhesive Joint Configurations in Fiber Metal Laminates.* Materials, 2022. **15**(5): p. 1840.
31. ASTM D3163-01. *Standard Test Method for Determining Strength of Adhesively Bonded Rigid Plastic Lap-Shear Joints in Shear by Tension Loading*. West Conshohocken, PA: ASTM International; 2023.
32. ASTM D3528-96. *Standard Test Method for Strength Properties of Double Lap Shear Adhesive Joints by Tension Loading*. West Conshohocken, PA: ASTM International; 2016.
33. Tian, Y., Wang, L., Anyasodor, G., Xu, Z., and Qin, Y., *Heating schemes and process parameters of induction heating of aluminium sheets for hot stamping*. Manufacturing Review, 2019. **6**: p. 17.
34. Coppola, B., Cappetti, N., Di Maio, L., Scarfato, P., and Incarnato, L., *3D Printing of PLA/clay Nanocomposites: Influence of Printing Temperature on Printed Samples Properties.* Materials, 2018. **11**(10): p. 1947.
35. Abeykoon, C., Sri-Amphorn, P., and Fernando, A., *Optimization of fused deposition modeling parameters for improved PLA and ABS 3D printed structures*. International Journal of Lightweight Materials and Manufacture, 2020. **3**(3): p. 284–297.
36. Soares, JB., Finamor, J., Silva, FP., Roldo, L., and Cândido, LH., *Analysis of the influence of polylactic acid (PLA) colour on FDM 3D printing temperature and part finishing*. Rapid Prototyping Journal, 2018. **24**(8): p. 1305–1316.

37. Öz, Ö., and Öztürk, FH., *An investigation on failure behaviour of bonded polylactic acid adherends produced by 3D printing process: experimental and numerical approach*. Journal of the Brazilian Society of Mechanical Sciences and Engineering, 2023. **45**(8): p. 399.
38. Zhang, X., Chen, L., Mulholland, T., and Osswald, TA., *Characterization of mechanical properties and fracture mode of PLA and copper/PLA composite part manufactured by fused deposition modeling*. SN Applied Sciences, 2019. **1**(6): p. 616.
39. Öztürk, FH., Marques, E a. S., Carbas, RJC., and da Silva, LFM., *Experimental and numerical study on mechanical behavior of 3D printed adhesive joints with polycarbonate substrates*. Journal of Applied Polymer Science, 2024. **141**(29): p. 1-18.
40. Zhao, B., Lu, ZH., and Lu, YN., *Two-dimensional analytical solution of elastic stresses for balanced single-lap joints—Variational method.* International Journal of Adhesion and Adhesives, 2014. **49**: p. 115–126.
41. da Silva, LFM., and Adams, R., *Techniques to reduce the peel stresses in adhesive joints with composites.* International Journal of Adhesion and Adhesives, 2007. **27**(3): p. 227–235.
42. Barbosa, NGC., Campilho, RDSG., Silva, FJG., and Moreira, RDF., *Comparison of different adhesively-bonded joint types for mechanical structures.* Applied Adhesion Science, 2018. **6**(1): p. 1-19.

Available online at www.dergipark.org.tr/en

e-ISSN: 2618-575X

INTERNATIONAL ADVANCED RESEARCHES and ENGINEERING JOURNAL

Journal homepage: www.dergipark.org.tr/en/pub/iarej

International Open Access

Volume 08
Issue 03

December, 2024

Research Article

Thermomechanical vibration response of nickel foam nanoplates

Mustafa Eroğlu [a]

[a]*Engineering Faculty, Mechanical Engineering Department, Sakarya University, Sakarya, 54187, Turkey*

ARTICLE INFO

Article history:
Received 22 August 2024
Accepted 19 December 2024
Published 20 December 2024

Keywords:
Foam
Nanoplate
Thermal buckling
Vibration

ABSTRACT

This article studies the buckling properties of nickel foam nanoplate. This research used nonlocal strain gradient elasticity and the new theory of sinusoidal higher-order deformation. After deriving the nanoplate's equations of motion from Hamilton's principle, the Navier technique was used to solve them. Two different kinds of foam models, uniform and symmetric, can be used to depict the nanoplate. Examining the nanoplate's dimensionless fundamental natural frequencies was the study's primary goal. The effects of temperature difference, nonlocal parameters, foam void ratio, and two different kinds of foam were considered in this investigation. In this context, the nanoplate's natural frequency decreases by 23.78% in the symmetric foam model and 51.5% in the uniform foam model as the foam void ratio increases. The research provides valuable insights for the development of nanoelectromechanical systems (NEMS), nanosensors, and transducers intended for high-temperature environments. By analyzing the impact of temperature and foam void ratio on nanoplate stability, the study informs material selection and structural design for applications where performance under thermal stress is critical, such as in aerospace and energy sectors.

1. Introduction

The vibration analysis of nanoplates can be effectively studied through nonlocal viscoelasticity models [1]. These models consider factors like viscoelasticity and piezoelectricity, which are crucial in understanding the dynamic characteristics of nanoscale structures. Researchers have explored the behavior of various nanomaterials like carbon nanotubes under different conditions, such as longitudinal magnetic fields, emphasizing the importance of nonlocal theories in predicting wave propagation and dynamic characteristics [2]. Additionally, using smart materials like self-healing polymer composites has gained attention for repairing microcracks in nanoplates, showcasing the practical applications of advanced materials in maintaining structural integrity [3]. Further research on the size-dependent vibration of nanoplates reinforced with carbon nanotubes under various influences like longitudinal magnetic fields can provide valuable insights into their dynamic behavior [4].

Nanoplates, as nanoscale structures, possess unique properties that can be influenced by various factors, including thermal effects. The thermal properties of nanoplates play a crucial role in their applications, such as in heat dissipation, thermal energy conversion, and thermal stability. The thermal conductivity of nanoplates is a key characteristic that affects their ability to transfer heat efficiently [5]. Similarly, incorporating BN nanoplates into composite materials has been shown to enhance heat conduction and transfer capabilities, as evidenced by increased thermal conductivity and thermal diffusivity [6]. Furthermore, the thermal behavior of nanoplates can impact their photothermal conversion efficiency. Graphite nanoplates, for instance, have been demonstrated to convert solar light into thermal energy through lattice vibrations of the carbon backbone [7]. Moreover, the thermal properties of nanoplates can influence their electrical and thermoelectric performance. For example, the fabrication of Au-Sb_2Te_3 nanoplates with optimized interface barriers and phonon scattering has resulted in synergistically optimal electrical and thermal properties [8]. Additionally, the growth of ultrathin Bi_2Te_3 nanoplates and subsequent fabrication of nanostructured thermoelectric materials have been reported, highlighting the importance of thermal management in enhancing thermoelectric efficiency [9]. Studies have shown that

* Corresponding author. Tel.: *+90-264-295-5587*.
E-mail addresses: mustafaeroglu@sakarya.edu.tr *(M. Eroğlu)*
ORCID: 0000-0002-1429-7656 *(M. Eroğlu)*
DOI: 10.35860/iarej.1537234

adding graphene nanoplates to nanofluids can improve thermal efficiency and heat transfer characteristics in heat exchangers [10, 11]. Similarly, metal-containing nanofluids with nanoplates have been investigated for thermal energy storage applications, demonstrating enhanced specific heat due to interfacial layering effects [12].

An expanding field of study, foam nanoplates have great promise for various engineering contexts. Nanoplate structures' vibration properties can be greatly affected by foams. Al-Waily et al. investigated micro aluminum powder-reinforced foam sandwich plates using free vibration analysis [13]. Functionally graded nanoporous metal foam nanoplates showed exceptional fracture toughness and electrical solid conductivities, making them appropriate for thin-film elements [14]. The study focused on free vibration and buckling in the FG porous beam's response to thermal effects and magnetic fields [15]. Zhao et al. investigated the sandwich plates with aluminum foam cores experimentally and numerically [16]. Sun et al. used carbon fiber/epoxy stitched reinforcements with a precisely adjusted fiber volume fraction to strengthen foam core sandwich constructions [17]. Also, aluminum facesheets were utilized with polyurethane and polystyrene foam cores [18].

As demonstrated in a recent study, the use of additives in biodiesel and the coating of tractor engine components can significantly reduce fuel consumption and exhaust emissions, while promoting more environmentally friendly agricultural practices [19]. As investigated in a recent study, blending hexane and water with diesel fuel in ceramic-coated and uncoated diesel engines can improve emission and performance parameters, with the ceramic coating proving to be the most effective factor for all tested parameters [20].

Nanosensors and nanoelectromechanical systems are widely used in high-temperature applications due to nanotechnology's widespread use. To ensure exact measurement and operation of these systems, new designs or configurations, such as the sandwich arrangement, must be developed. This study must make unique contributions due to a dearth of literature. This study examined foam nanoplate thermomechanical vibration to meet the criteria. The nanoplates are nickel foam. The initiative aims to build and test high-temperature nanoplates.

2. Modelling of Foam Nanoplate

The equations of motion for the nanoplate analyzed in this paper were derived using the Hamiltonian approach. This method allows for examining the nanoplate's dynamic behaviour in the temperature environment. Fig. 1 shows the physical depiction of a rectangular nanoplate positioned in the *x, y, z* coordinate system. The nanoplate consists of a single layer. The dimensions of the nanoplate in the *y* and *x* directions are specified as *a* and *b*, respectively. The thickness is denoted by the variable *h*.

This study investigates the dynamic characteristics of a nanoplate composed exclusively of nickel foam. Fig. 1 displays two distinct varieties of foam nanoplates within this environment. Fig. 1a depicts a homogenous foam model, whereas Fig. 1b shows a foam model with concentrated surface regions. The Young Modulus *E* and densities of the aforementioned models are provided as follows [21–24].

Uniform foam (Fig. 1a):

$$\begin{aligned} E(z) &= E_1(1-\alpha\psi) \\ \rho(z) &= \rho_1\sqrt{(1-\alpha\psi)} \\ \psi &= \frac{1}{\alpha}-\frac{1}{\alpha}\left(\frac{2\sqrt{(1-\alpha\psi)}}{\pi}-\frac{2}{\pi}+1\right)^2 \end{aligned} \tag{1}$$

Symmetric foam (Fig. 2a):

$$\begin{aligned} E(z) &= E_1[1-\alpha\cos(\pi z/h)] \\ \rho(z) &= \rho_1[1-\alpha_d\cos(\pi z/h)] \\ \alpha_d &= 1-\sqrt{(1-\alpha)} \end{aligned} \tag{2}$$

ρ_1 and E_1 denote the density and young modulus of the nickel foam, respectively. The symbol α represents the foam's void ratio.

Uniform foam models represent a consistent distribution of voids throughout the structure, making them suitable for applications requiring isotropic mechanical properties and ease of manufacturing. On the other hand, symmetric foam models account for graded distributions of voids, which are more representative of advanced fabrication techniques, such as additive manufacturing or layer-by-layer deposition.

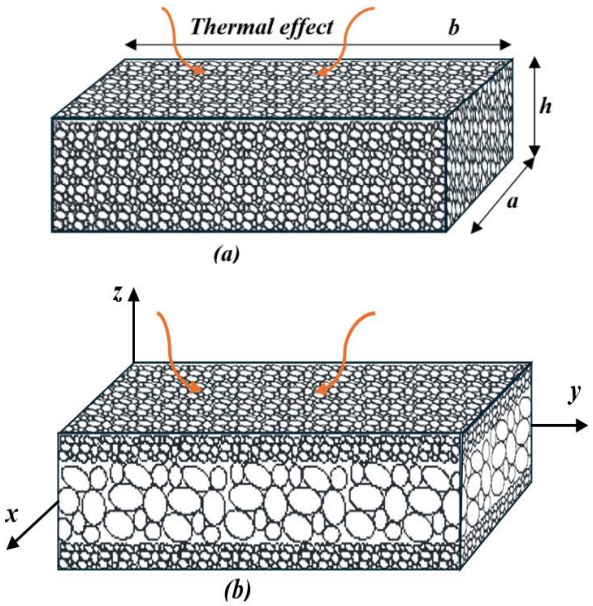

Figure 1. Configuration of nickel nanoplate a) Uniform foam model b) Symmetric foam model

These models offer enhanced control over material properties, allowing for tailored responses to specific operational requirements, such as improved thermal resistance or localized stiffness. By analyzing both models, the study provides a comprehensive understanding of how different foam configurations influence the structural performance of nanoplates, offering insights for designing materials optimized for specific engineering applications.

2.1 The temperature effect on nanoplate

Temperature parameters are necessary as the impact of temperature on the behaviour of the nanoplate is considered. The equation provided describes the non-linear relationship between the material characteristics, such as the temperature-dependent elastic modulus and Poisson's ratio [25].

$$P = P_0(P_{-1}T^{-1} + 1 + P_1T + P_2T^2 + P_3T^3) \quad (3)$$

In this context, the symbol P indicates an ingredient that varies with temperature, whereas P_0 represents the matching material. Table 1 presents the P_{-1}, P_1, P_2, and P_3 values that correlate to the temperature T.

The temperature distribution of the nanoplate in the z direction can be described by the following linear equation. Here, T_1 and T_2 denote the temperature of the lower and upper surfaces, respectively, and the temperature rise is considered to be from T_1 to T_2 [26].

$$T(z) = T_1 + (T_2 - T_1)\left(\frac{h + 2z}{2h}\right) \quad (4)$$

The non-linear temperature rise in the nanoplate is demonstrated by solving the heat transfer equation. The expression is as follows: [27].

$$-\frac{d}{dz}\left(\kappa(z)\frac{dT}{dz}\right) = 0, \qquad T\left(\frac{h}{2}\right) = T_2, \quad T\left(-\frac{h}{2}\right) = T_1 \quad (5)$$

$$T(z) = T_1 + \frac{(T_2 - T_1)}{\int_{-\frac{h}{2}}^{\frac{h}{2}} \frac{1}{\psi(z)} d(z)} \int_{-\frac{h}{2}}^{z} \psi(z)dz \quad (6)$$

Table 1. Coefficients that vary with temperature for Nickel (Ni) characteristics

Property	P_{-1}	P_0	P_1	P_2	P_3
ρ (kg/m^3)	0	8900	0	0	0
E (Pa)	0	223x10^9	-2.79x10^{-4}	3.99x10^{-7}	0
υ	0	0.31	0	0	0
α (1K^{-1})	0	9.9x10^{-6}	8.70x10^{-4}	0	0
ψ (W/mK)	0	58.74	-4.6x10^{-4}	6.67x10^{-7}	-1.52x10^{-10}

2.2 The theory of nonlocal strain gradient theory (NSGT)

Eringen's research suggests that the stress within a body is intrinsically connected to all other locations, and the structure's stiffness is influenced by the material size factor and the nonlocal density [28]. The stress tensors σ and $\boldsymbol{\sigma}^{(h)}$ in NSGT are expressed by the following equations [29].

$$\sigma = \int_V \alpha_0(\boldsymbol{x}', \boldsymbol{x}, e_0a)\boldsymbol{C} : \varepsilon'(\boldsymbol{x}')dV' \quad (7a)$$

$$\sigma^{(h)} = l_m^2 \int_V \alpha_1(\boldsymbol{x}', \boldsymbol{x}, e_1a)\boldsymbol{C} : \nabla\varepsilon'(\boldsymbol{x}')dV' \quad (7b)$$

In this context, α_0 and α_1 denote the conventional kernel and nonlocal functions of higher order, while ∇ and C correspond the Laplacian operator (∇=∂/∂x+∂/∂y) and the fourth-order material coefficient, respectively. The terms ∇ε and ε denote the classical strain tensors and the strain gradient, respectively. The symbols e_0 and e_1 represent the nonlocal coefficients, while l_m represents the material size factor. The symbol ":" represents the tensor's double-dot product. The tensor of stress obtained from the Navier equations can be expressed as [29, 30].

$$\sigma^t = \sigma - \nabla^2\sigma^{(1)} \quad (8)$$

Given that the concepts of $\alpha_1(\boldsymbol{x}', \boldsymbol{x}, e_1a)$ and $\alpha_0(\boldsymbol{x}', \boldsymbol{x}, e_0a)$ align with the Ref. [31] and that e_0=e_1=e$_0$a, using the linear differentiation operator yields the following result.

$$[1 - (e_0a)^2\nabla^2]\sigma = \mathbf{C} : \varepsilon, [1 - (e_0a)^2\nabla^2]\sigma^{(1)} = l_m^2\,\mathbf{C} : \nabla\varepsilon \quad (9)$$

Eq. 9 can be employed to compute the overall stress in the following manner:

$$[1 - (e_0a)^2\nabla^2]\sigma = \mathbf{C} : \varepsilon - l_m^2\,\nabla\mathbf{C} : \nabla\varepsilon \quad (10)$$

Stress-strain relations of plate are calculated by Refs. [29, 32]:

$$[1 - (e_0a)^2\nabla^2]\sigma_{xx} = [1 - l_m^2\nabla^2]E(z)\varepsilon_{xx} \quad (11a)$$

$$[1 - (e_0a)^2\nabla^2]\sigma_{yy} = [1 - l_m^2\nabla^2]E(z)\varepsilon_{yy} \quad (11b)$$

$$[1 - (e_0a)^2\nabla^2]\sigma_{xz} = [1 - l_m^2\nabla^2]G(z)\gamma_{xz} \quad (11c)$$

$$[1 - (e_0a)^2\nabla^2]\sigma_{yz} = [1 - l_m^2\nabla^2]G(z)\gamma_{yz} \quad (11d)$$

The equations provided above define the strains and stresses in the y and x directions as σ_{xx}, σ_{yy}, ε_{xx}, and ε_{yy}, respectively. The shear stresses and strains are represented by σ_{xz}, σ_{yz}, and γ_{xz}, γ_{yz}. E(z) and G(z) denote the elasticity and shear modulus, correspondingly. The classical continuum theory's stress-strain relations can be calculated by setting

the nonlocal parameters in these equations to zero [31].

2.3 Kinematic relation

Sinusoidal higher-order shear deformation theory was used in the analysis of this structure consisting of a single-layered rectangular plate [33]. For plane displacements *u* and *v*, u_0 represents extension, w_s represents shear, and w_0 represents bending. To account for bending w_0 and shear w_s components of transverse stresses (σ_{xz}, σ_{yz}, σ_{zz}) and strains (ε_{xz}, ε_{yz}, ε_{zz}), the transverse displacement w is adjusted. Incorporating shear components increases the trigonometric variation of shear stresses (σ_{xz}, σ_{yz}) and strains (ε_{xz}, ε_{yz}) over plate thickness. As to this idea, the nanoplate's displacement field is:

$$\begin{aligned} u(x,y,z,t) &= u_0(x,y,t) - z\frac{\partial w_0(x,y,t)}{\partial x} \\ &\quad - f(z)\frac{\partial w_s(x,y,t)}{\partial x} \\ v(x,y,z,t) &= v_0(x,y,t) - z\frac{\partial w_0(x,y,t)}{\partial y} \\ &\quad - f(z)\frac{\partial w_s(x,y,t)}{\partial y} \\ w(x,y,z,t) &= w_0(x,y,t) + w_s(x,y,t) \\ &\quad + w_{st}(x,y,z,t) \end{aligned} \tag{12}$$

Let's establish the definitions of the *f(z)*, w_{st}, and *g(z)* as follows:

$$\begin{aligned} f(z) &= z - \frac{h}{\pi}\sin\left(\frac{\pi z}{h}\right) \\ w_{st}(x,y,z,t) &= \mathrm{g}(z)\emptyset(x,y,t), \\ g(z) &= cos\,(\frac{\pi z}{h}) \end{aligned} \tag{13}$$

The total displacements represented by the variables *u*, *v*, and *w* in the displacement equations. A midplane of the unshaped plate is represented by the symbols u_0, v_0, and w_0, which stand for in-plane and transverse displacements, respectively. While the w displacement indicates the bending deflection of the plate, the *u* and *v* displacements are linked to its extensional deformation. In terms of the displacement field, the following is a general form for the strain-displacement interactions:

$$\begin{aligned} \begin{Bmatrix} \varepsilon_{xx} \\ \varepsilon_{yy} \\ 2\varepsilon_{xy} \end{Bmatrix} &= \begin{Bmatrix} \varepsilon_{xx}^{(0)} \\ \varepsilon_{yy}^{(o)} \\ \gamma_{xy}^{(0)} \end{Bmatrix} + z\begin{Bmatrix} \varepsilon_{xx}^{(b)} \\ \varepsilon_{yy}^{(b)} \\ \gamma_{xy}^{(s)} \end{Bmatrix} \\ \begin{Bmatrix} 2\varepsilon_{xz} \\ 2\varepsilon_{yz} \end{Bmatrix} &= g(z)\begin{Bmatrix} \gamma_{xz}^{(0)} \\ \gamma_{yz}^{(0)} \end{Bmatrix} \\ \varepsilon_{zz} &= g'(z)\varepsilon_{zz}^{(0)} \end{aligned} \tag{14}$$

The strain components are as follows:

$$\begin{aligned} \begin{Bmatrix} \varepsilon_{xx}^{(0)} \\ \varepsilon_{yy}^{(0)} \\ \gamma_{xy}^{(0)} \end{Bmatrix} &= \begin{Bmatrix} \dfrac{\partial u_0}{\partial x} \\ \dfrac{\partial v_0}{\partial y} \\ \dfrac{\partial u_0}{\partial y} + \dfrac{\partial v_o}{\partial x} \end{Bmatrix}, \begin{Bmatrix} \varepsilon_{xx}^{(b)} \\ \varepsilon_{yy}^{(b)} \\ \gamma_{xy}^{(b)} \end{Bmatrix} \\ &= \begin{Bmatrix} -\dfrac{\partial^2 w_0}{\partial x^2} \\ -\dfrac{\partial^2 w_0}{\partial y^2} \\ -2\dfrac{\partial^2 w_0}{\partial x \partial y} \end{Bmatrix} \\ \begin{Bmatrix} \gamma_{xz}^{(0)} \\ \gamma_{yz}^{(o)} \end{Bmatrix} &= \begin{Bmatrix} \left(1 - f'(z)\right)\dfrac{\partial w_s}{\partial x} + g(z)\dfrac{\partial \emptyset}{\partial x} \\ \left(1 - f'(z)\right)\dfrac{\partial w_s}{\partial y} + g(z)\dfrac{\partial \emptyset}{\partial y} \end{Bmatrix} \\ &= \begin{Bmatrix} g(z)\left(\dfrac{\partial w_s}{\partial x} + \dfrac{\partial \emptyset}{\partial x}\right) \\ g(z)\left(\dfrac{\partial w_s}{\partial y} + \dfrac{\partial \emptyset}{\partial y}\right) \end{Bmatrix} \\ \varepsilon_{zz}^{(0)} &= \emptyset \end{aligned} \tag{15}$$

The stresses can be obtained from the constitutive relations using the given formula.

$$\begin{Bmatrix} \sigma_x \\ \sigma_y \\ \sigma_z \\ \sigma_{xy} \\ \sigma_{xz} \\ \sigma_{yz} \end{Bmatrix} = \begin{bmatrix} C_{11} & C_{12} & C_{13} & 0 & 0 & 0 \\ C_{12} & C_{22} & C_{23} & 0 & 0 & 0 \\ C_{13} & C_{23} & C_{33} & 0 & 0 & 0 \\ 0 & 0 & 0 & C_{66} & 0 & 0 \\ 0 & 0 & 0 & 0 & C_{55} & 0 \\ 0 & 0 & 0 & 0 & 0 & C_{44} \end{bmatrix} \begin{Bmatrix} \varepsilon_x \\ \varepsilon_y \\ \varepsilon_z \\ \gamma_{xy} \\ \gamma_{xz} \\ \gamma_{yz} \end{Bmatrix} \tag{16}$$

which are defined as the three-dimensional elastic constants C_{ij}

$$\begin{aligned} C_{11} = C_{22} = C_{33} &= \frac{(1-v)E}{(1-2v)(1+v)} \\ C_{12} = C_{13} = C_{23} &= \frac{vE}{(1-2v)(1+v)} \\ C_{44} = C_{55} = C_{66} &= \frac{E}{2(1+v)} \end{aligned} \tag{17}$$

Rewriting the constitutive relations

$$\begin{aligned} &\begin{Bmatrix} \sigma_x \\ \sigma_y \\ \sigma_{xy} \\ \sigma_{yz} \\ \sigma_{xz} \end{Bmatrix} \\ &= \frac{E}{1-v^2}\begin{bmatrix} 1 & v & 0 & 0 & 0 \\ v & 1 & 0 & 0 & 0 \\ 0 & 0 & \dfrac{(1-v)}{2} & 0 & 0 \\ 0 & 0 & 0 & \dfrac{(1-v)}{2} & 0 \\ 0 & 0 & 0 & 0 & \dfrac{(1-v)}{2} \end{bmatrix} \begin{Bmatrix} \varepsilon_x \\ \varepsilon_y \\ \gamma_{xy} \\ \gamma_{yz} \\ \gamma_{xz} \end{Bmatrix} \end{aligned} \tag{18}$$

where nanoplate Young's modulus is *E* and Poisson's ratio is *v*. For simplicity's sake, we'll assume that Poisson's ratio *v* is constant, since it has a negligible effect on nanoplate responses.

The strain energy

$$U = \frac{1}{2}\int_A \int_{-h/2}^{h/2} \left(\sigma_x \varepsilon_x + \sigma_y \varepsilon_y + \sigma_z \varepsilon_z + \sigma_{xy}\gamma_{xy} + \sigma_{xz}\gamma_{xz} + \sigma_{yz}\gamma_{yz}\right) dA dz \tag{19}$$

The strain energy can be rewritten as below:

$$U = \frac{1}{2}\int_A \left[N_x \frac{\partial u}{\partial x} - M_x^b \frac{\partial^2 w_b}{\partial x^2} + N_y \frac{\partial v}{\partial y} - M_y^b \frac{\partial^2 w_b}{\partial y^2} + R_z w_z + N_{xy}\left(\frac{\partial u}{\partial y} + \frac{\partial v}{\partial x}\right) - 2M_{xy}^b \frac{\partial^2 w_b}{\partial x\, \partial y} + Q_z\left(\frac{\partial w_s}{\partial \mathrm{x}} + \frac{\partial w_z}{\partial x}\right) + Q_y\left(\frac{\partial w_s}{\partial \mathrm{y}} + \frac{\partial w_z}{\partial y}\right)\right] \tag{20}$$

as the stress resultants N, M, Q, and R are defined by

$$\begin{aligned} \left(N_x, N_y, N_{xy}\right) &= \int_{-\frac{h}{2}}^{\frac{h}{2}} \left(\sigma_x, \sigma_y, \sigma_{xy}\right) dz \\ \left(M_x^b, M_y^b, M_{xy}^b\right) &= \int_{-h/2}^{h/2} \left(\sigma_x, \sigma_y, \sigma_{xy}\right) z dz \\ \left(Q_x, Q_y\right) &= \int_{-\frac{h}{2}}^{\frac{h}{2}} \left(\sigma_{xz}, \sigma_{yz}\right) g(z) dz \\ R_z &= \int_{-h/2}^{h/2} \sigma_z g'(z) dz \end{aligned} \tag{21}$$

Stress results is given as below:

$$\begin{aligned} N_x &= A_{11}\frac{\partial u}{\partial x} + A_{12}\frac{\partial v}{\partial y} - B_{11}\frac{\partial^2 w_b}{\partial x^2} - B_{12}\frac{\partial^2 w_b}{\partial y^2} + X_{13} w_z \\ N_y &= A_{12}\frac{\partial u}{\partial x} + A_{22}\frac{\partial v}{\partial y} - B_{12}\frac{\partial^2 w_b}{\partial x^2} - B_{22}\frac{\partial^2 w_b}{\partial y^2} + X_{23} w_z \\ N_{xy} &= A_{66}\left(\frac{\partial u}{\partial y} + \frac{\partial v}{\partial x}\right) - 2B_{66}\frac{\partial^2 w_b}{\partial x\, \partial y} \\ M_x^b &= B_{11}\frac{\partial u}{\partial x} + B_{12}\frac{\partial v}{\partial y} - D_{11}\frac{\partial^2 w_b}{\partial x^2} - D_{12}\frac{\partial^2 w_b}{\partial y^2} + Y_{13} w_z \\ M_y^b &= B_{12}\frac{\partial u}{\partial x} + B_{22}\frac{\partial v}{\partial y} - D_{12}\frac{\partial^2 w_b}{\partial x^2} - D_{22}\frac{\partial^2 w_b}{\partial y^2} + Y_{23} w_z \\ M_{xy}^b &= B_{66}\left(\frac{\partial u}{\partial y} + \frac{\partial v}{\partial x}\right) - 2D_{66}\frac{\partial^2 w_b}{\partial x\, \partial y} \end{aligned} \tag{22}$$

$$R_z = X_{13}\frac{\partial u}{\partial x} + X_{23}\frac{\partial v}{\partial y} - Y_{13}\frac{\partial^2 w_b}{\partial x^2} - Y_{23}\frac{\partial^2 w_b}{\partial y^2} + Z_{33} w_z$$

where

$$\begin{aligned} \left(A_{ij}, B_{ij}, D_{ij}, H_{ij}^s\right) &= \int_{-\frac{h}{2}}^{\frac{h}{2}} (1, g^2, z, f, z^2, fz, f^2) C_{ij} dz \\ \left(X_{ij}, Y_{ij}, Z_{ij}\right) &= \int_{-h/2}^{h/2} (g', g'z, g'f, g'^2) C_{ij} dz \end{aligned} \tag{23}$$

Work is done by externally transverse loads q by the use of

$$V = -\int_A q(w_b + w_s + g w_z) dA \tag{24}$$

The kinetic energy;

$$K = \frac{1}{2}\int_A \int_{-h/2}^{h/2} \rho(\dot{u}_1^2 + \dot{u}_2^2 + \dot{u}_3^2) dA dz \tag{25}$$

where ρ is the effective mass density of plates and the dot-superscript convention shows the differentiation concerning the time variable *t*. The equations of motion are determined using Hamilton's principle. The principle can be indicated analytically in one approach as

$$\int_0^T \delta(U + V - K) dt = 0 \tag{26}$$

δ is the variational operator.

To obtain the following motion equations, we take the *U*, *V*, and *K* expressions, and then gather the coefficients of (δ_u, δ_v, δ_{wb}, δ_{ws}, δ_{wz}).

$$\begin{aligned} \delta u: &\frac{\partial N_x}{\partial x} + \frac{\partial N_{xy}}{\partial y} = I_0 \ddot{u} - I_1 \frac{\partial \ddot{w}_b}{\partial x} - J_1 \frac{\partial \ddot{w}_s}{\partial x} \\ \delta v: &\frac{\partial N_{xy}}{\partial x} + \frac{\partial N_y}{\partial y} = I_0 \ddot{v} - I_1 \frac{\partial \ddot{w}_b}{\partial y} - J_1 \frac{\partial \ddot{w}_s}{\partial y} \\ \delta w_b: &\frac{\partial^2 M_x^b}{\partial x^2} + 2\frac{\partial^2 M_{xy}^b}{\partial x\, \partial y} + \frac{\partial^2 M_y^b}{\partial y^2} + q = I_0(\ddot{w}_b + \ddot{w}_s) + J_0 \ddot{w}_z + I_1\left(\frac{\partial \ddot{u}}{\partial x} + \frac{\partial \ddot{v}}{\partial y}\right) - I_2 \nabla^2 \ddot{w}_b - J_2 \nabla^2 \ddot{w}_s \\ \delta w_s: &\frac{\partial Q_{xz}}{\partial x} + \frac{\partial Q_{yz}}{\partial y} + q = I_0(\ddot{w}_b + \ddot{w}_s) + J_0 \ddot{w}_z + J_1\left(\frac{\partial \ddot{u}}{\partial x} + \frac{\partial \ddot{v}}{\partial y}\right) - J_2 \nabla^2 \ddot{w}_b - K_2 \nabla^2 \ddot{w}_s \end{aligned} \tag{27}$$

$$\delta w_z: \frac{\partial Q_{xz}}{\partial x} + \frac{\partial Q_{yz}}{\partial y} - R_z + gq = J_0(\ddot{w}_b + \ddot{w}_s) + K_0\ddot{w}_z$$

2.4 Analytical Solution

By using Navier's approach with simple boundary conditions, we may estimate displacements *u(x,t)*, *w(x,t)* and *ϕ(x,t)* with a periodic solution in time.

$$\begin{aligned} u(x,y,t) &= \sum_{m=1}^{\infty}\sum_{n=1}^{\infty} U_{mn} e^{i\omega_n t} \cos\alpha x \sin\beta y \\ v(x,y,t) &= \sum_{m=1}^{\infty}\sum_{n=1}^{\infty} V_{mn} e^{i\omega_n t} \sin\alpha x \cos\beta y \\ w_b(x,y,t) &= \sum_{m=1}^{\infty}\sum_{n=1}^{\infty} W_{bmn} e^{i\omega_n t} \sin\alpha x \sin\beta y, \\ w_s(x,y,t) &= \sum_{m=1}^{\infty}\sum_{n=1}^{\infty} W_{smn} e^{i\omega_n t} \sin\alpha x \sin\beta y \\ w_z(x,y,t) &= \sum_{m=1}^{\infty}\sum_{n=1}^{\infty} W_{zmn} e^{i\omega_n t} \sin\alpha x \sin\beta y \end{aligned} \quad (28)$$

$$\beta = \left(\frac{n\pi}{L}\right) \qquad \alpha = \left(\frac{m\pi}{L}\right)$$

The coefficients (U_{mn}, V_{mn}, W_{bmn}, W_{smn}, W_{zmn}) and natural frequency ω_n are represented. Eq. (28) solves for U_n, W_n, and Φ_n at x=0 and x=L, satisfying both classical and non-classical boundary conditions.

The closed-form answers are derived below:

$$\left(\begin{bmatrix} s_{11} & s_{12} & s_{13} & s_{14} & s_{15} \\ s_{12} & s_{22} & s_{23} & s_{24} & s_{25} \\ s_{13} & s_{23} & s_{33} & s_{34} & s_{35} \\ s_{14} & s_{24} & s_{34} & s_{44} & s_{45} \\ s_{15} & s_{25} & s_{35} & s_{45} & s_{55} \end{bmatrix} - \omega^2 \begin{bmatrix} m_{11} & 0 & m_{13} & m_{14} & 0 \\ 0 & m_{22} & m_{23} & m_{24} & 0 \\ m_{13} & m_{23} & m_{33} & m_{34} & m_{35} \\ m_{14} & m_{24} & m_{34} & m_{44} & m_{45} \\ 0 & 0 & m_{35} & m_{45} & m_{55} \end{bmatrix} \right) \begin{Bmatrix} U_{mn} \\ V_{mn} \\ W_{bmn} \\ W_{smn} \\ W_{zmn} \end{Bmatrix} = 0 \quad (29)$$

In Eq. (28), i is the imaginary unit. The symbol ω_n represents the nth natural vibration frequencies.

$$(\mathbf{S} - \omega_n^2 \mathbf{M})\mathbf{d} = 0 \quad (30)$$

For this context, the vector of defined unknowns is $\mathbf{d} = \{U_n \quad W_n \quad \Phi_n\}^T$. Matrix **S** symbolizes stiffness and **M** mass. These matrices' coefficients are in Appendix A.

2.2 Verification

Table 2. Comparison of dimensionless frequency $\overline{w}$ in SSSS rectangular plates

Mode	Ref. [35]	Ref. [36]	Present Study
(1,1)	10.024	9.525	10.158
(2,2)	32.571	28.762	31.853
(3,3)	66.284	50.966	63.356
(4,4)	104.006	131.186	112.967
(5,5)	129.647	139.106	134.589

A comparative study was managed to verify the current methodology by comparing the central deflections of rectangular and square plates using three nonlocal plate theories. This study builds upon previous research [34]. The center deflection $\overline{w}$ is standardized by employing the equation for the point load q_0 and the uniform load Q_0.

$$\overline{w} = -w\left(\frac{Eh^2}{q_0 a^4}\right)10^2 \,, \overline{w} = -w\left(\frac{Eh^2}{Q_0 a^4}\right)10^2 \quad (31)$$

The plate parameters are *b*, *h*, *E*, and *ρ*, signifying length, height, elasticity modulus, and density. Table 2 presents a comparison of central deflections for SSSS isotropic plates with a length of a=10, modulus of elasticity E=30x10^6 MPa, and Poisson's ratio v=0.3, under a point load q_0=1N. The table includes the central deflections obtained using various theories.

To assess the correctness of the suggested method, the findings were compared with data from the literature Ref. [35] and Ref. [36]. Table 2 demonstrates a strong concordance between the findings of this investigation and those of the comparative studies. This validates the precision and dependability of the suggested procedure. The method demonstrates high accuracy in both analytical and numerical approaches. This comparison demonstrates that the suggested model exhibits competitive performance relative to existing methods in the literature and is suitable for safe application in engineering contexts.

3. Results

This study examined the fundamental dimensionless natural frequencies of the nanoplate at various temperatures. The nanoplate is composed of Nickel materials. In Fig. 1, The nanoplate can be classified into two unique foam types: the uniform foam model and the symmetric foam model. The frequencies are provided for foam void ratios (FVR) and two distinct foam types. The length of the nanoplate is b=500 nm, and its height is one-tenth of its length. The width of the plate is also the same as its length. In addition, the nanoplate was subjected to extreme temperature variations from all directions.

Fig. 2 illustrates the relationship between the fundamental natural frequencies of the nanoplate and both the foam void

ratio (FVR) and temperature variations. As the FVR rises, the natural frequencies decrease, indicating a reduction in the nanoplate's stiffness and structural stability. Similarly, as the ΔT rises, natural frequencies diminish further, eventually reaching zero at ΔT=3484, signaling the onset of buckling. This behavior underscores the critical role of thermal effects and material porosity in the structural integrity of nanoplates. Specifically, Fig. 2a shows that for a uniform foam model at ΔT=0, the dimensionless natural frequency of the nanoplate is $\lambda_{(1,1)}$=6.39, 5.34, 4.45, and 3.10 for foam void ratio α=0, 0.3, 0.6, and 0.9, respectively. This corresponds to a 51.5% reduction in the natural frequency as the FVR increases from 0 to 0.9, reflecting a significant weakening of the nanoplate's dynamic response due to increased void content. Fig. 2b highlights the symmetric foam model under the same FVR range, where the natural frequencies are $\lambda_{(1,1)}$=6.39, 5.69, 5.16, and 4.87 for α=0, 0.3, 0.6, and 0.9, respectively. Here, the reduction in natural frequency is comparatively lower at 23.78%, suggesting better retention of structural stability under increased FVRs. In Fig. 2c, the dependence of the natural frequencies on temperature variations for both foam types is presented at α=0.6. At ΔT=0, the natural frequency is $\lambda_{(1,1)}$=4.45 for uniform foam and 5.16 for symmetric foam. The plots indicate that the symmetric foam model exhibits higher frequency stability under temperature changes, while the uniform foam model is more susceptible to thermal effects. These observations highlight the importance of foam type and thermal considerations in designing nanoplates for applications requiring high stability, such as in thermal environments or precision instruments. The dimensionless natural frequencies of the nanoplate are investigated in Fig. 3, which illustrates the effect of α and temperature difference ΔT on its mechanical behavior. The analysis includes four different temperature variances and two types of foam. From the graphs, it is clear that the natural frequency of the nanoplate decreases as both the temperature difference and foam void ratio increase. The decrease in natural frequency with higher temperature differences can be attributed to the increased thermal stresses that reduce the structural stiffness of the nanoplate. In Fig. 3a, the natural frequency of the nanoplate for the uniform foam type at ΔT=0, 300, 600, and 1000 is $\lambda_{(1,1)}$=6.39, 6.1, 5.79, and 5.36, respectively. At a foam void ratio of 0.9, the frequencies are $\lambda_{(1,1)}$=3.1, 2.96, 2.81, and 2.6, showing a significant decrease of approximately 51% as the foam void ratio increases. The trend in Fig. 3b further emphasizes this, with a considerable decrease in the nanoplate's natural frequency as the foam void ratio increases. Fig. 3c compares the natural frequencies of uniform and symmetric foam types at a temperature difference of 600. The natural frequency values for both foam types are consistent when the α is zero, which signifies a solid material with no voids. As the foam void ratio increases, the natural frequency values decrease.

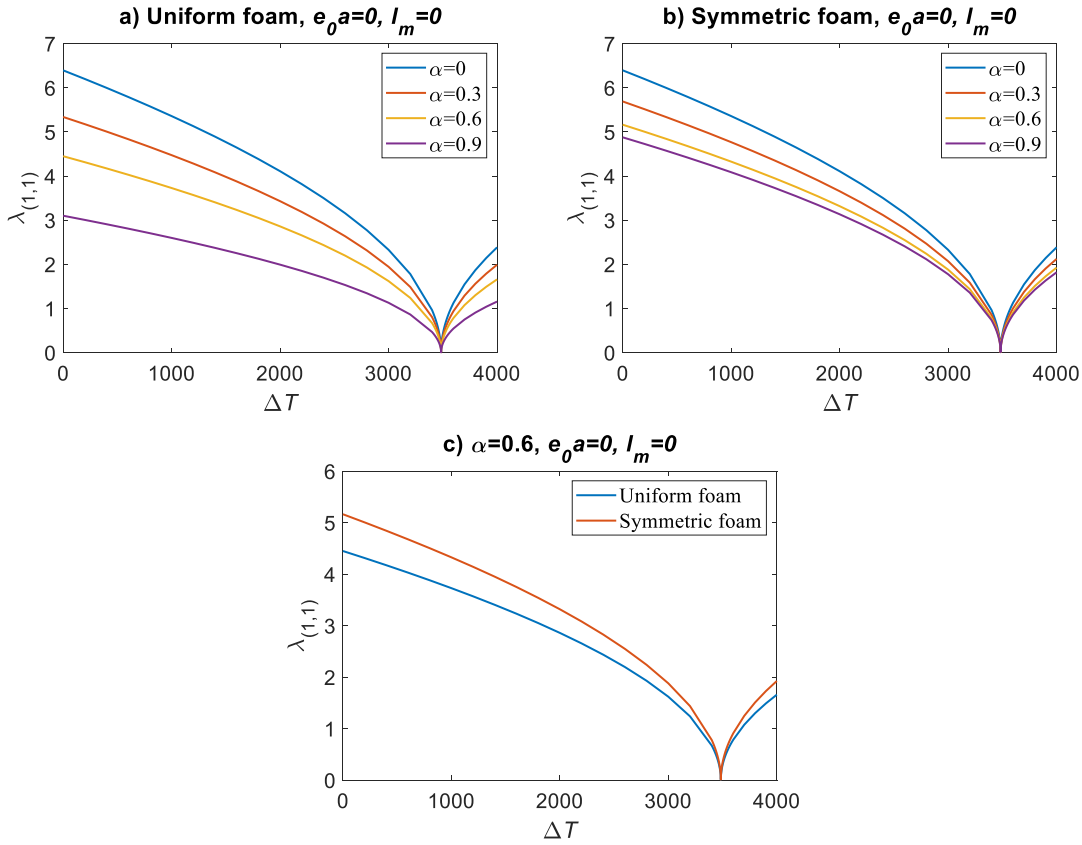

Figure. 2. Changing of the $\lambda_{(1,1)}$ depending on the ΔT and four distinct foam void ratios (α=0, 0.3, 0.6, 0.9)

For α=0, the natural frequency for both foam types is 5.79, whereas at α=0.9, the frequencies are 2.8 for uniform foam and 4.41 for symmetric foam. This demonstrates that while both foam types experience a reduction in natural frequency with increasing void ratio, the symmetric foam shows a comparatively smaller decrease, indicating that its structure might retain more stiffness and stability than the uniform foam under thermal and mechanical loading.

Figure 4 analyzes the effect of altering the temperature difference on the intrinsic natural frequency of the nanoplate. This is accomplished by analyzing four nonlocal parameters designated as e_0a=0, 1, 2, and 4. The graphical representations indicate that an increase in the nonlocal parameter and ΔT leads to a decrease in the natural frequency. Furthermore, it is crucial to note that even with a temperature differential of ΔT=3485, the nanoplate continues to undergo buckling. Analysis of Fig. 4a reveals that augmenting the nonlocal parameter from e_0a=0 to e_0a=4 nm² leads to a 25.28% reduction in the natural frequency, decreasing from λ=5.34 to λ=3.99. In Fig. 4b, the λ of the nanoplate is ascertained to be 5.69, with a nonlocal parameter e_0a of 0 and a ΔT of 0. Fig. 4c presents a comparative analysis of two different types of foam based on a singular nonlocal parameter. The variation in the fundamental frequencies of the nanoplate, seen in Fig. 5, is obtained by analyzing four distinct material size factors (l_m=0, 1, 2, and 4) alongside the temperature differential. Data analysis reveals that the dimensions of the material significantly influence the natural frequencies. In Fig. 5a, with parameters l_m=0 and ΔT=0, the natural frequency is determined to be λ=5.34. However, when the value of l_m is adjusted to 4 nm², the natural frequency rises to λ=7.14. Notably, when the material size grows, the natural frequency experiences an estimated 34% increase. In Fig. 5b, the natural frequencies of the symmetric foam model rise by around 33% with an increase in the material size factor. Furthermore, as the ΔT increases, the inherent frequencies across all dimensions of the material decrease.

At a temperature difference of 3484, the natural frequency values diminish to zero, leading to buckling. Moreover, when the nonlocal parameter increases in the graph above, the natural frequency of the nanoplate decreases, whereas it increases with a rise in material size factor. The graph in Fig. 5c depicts a comparison between two different types of foam, depending on a single factor of material size.

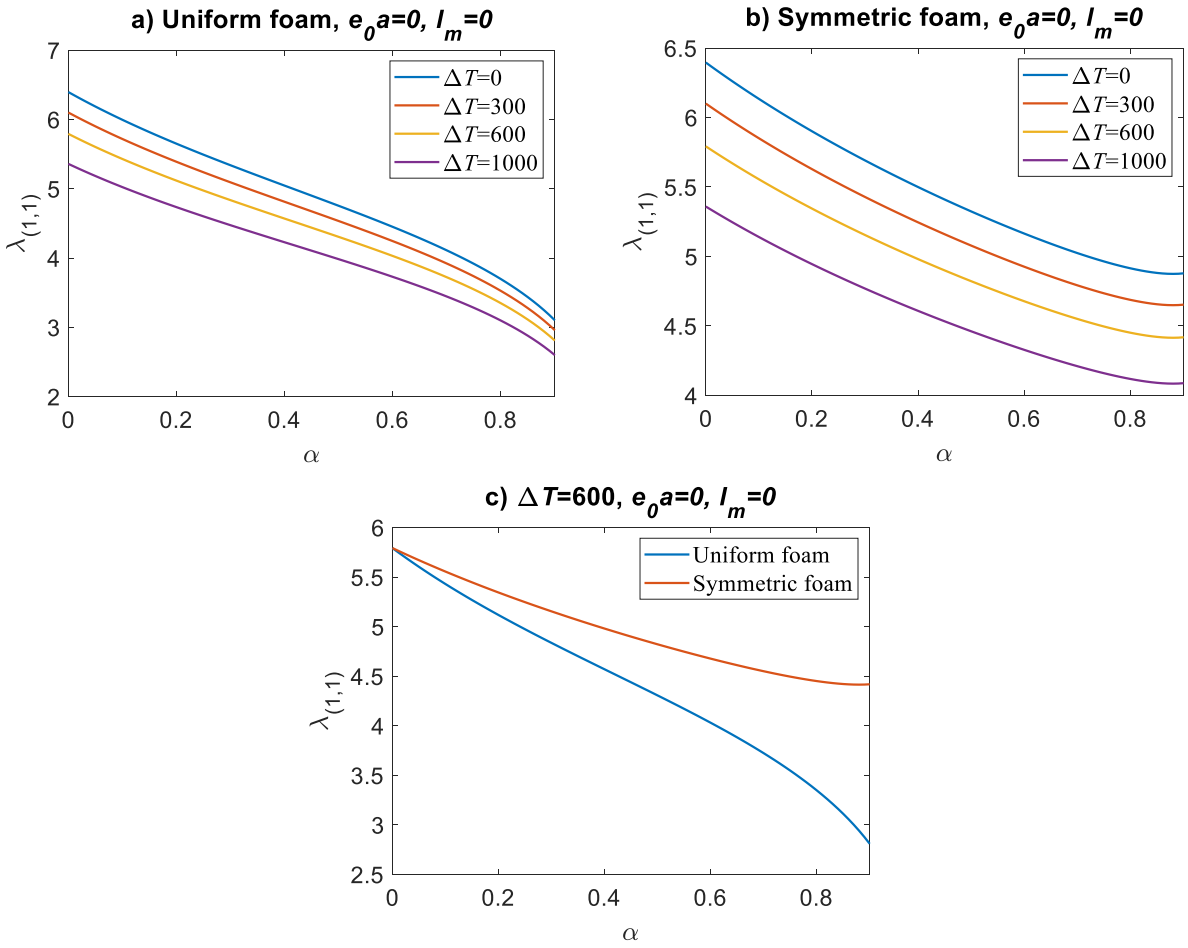

Figure 3. Changing of the $\lambda_{(1,1)}$ depending on the foam void ratio α and four distinct ΔT (ΔT=0, 300, 600, 1000)

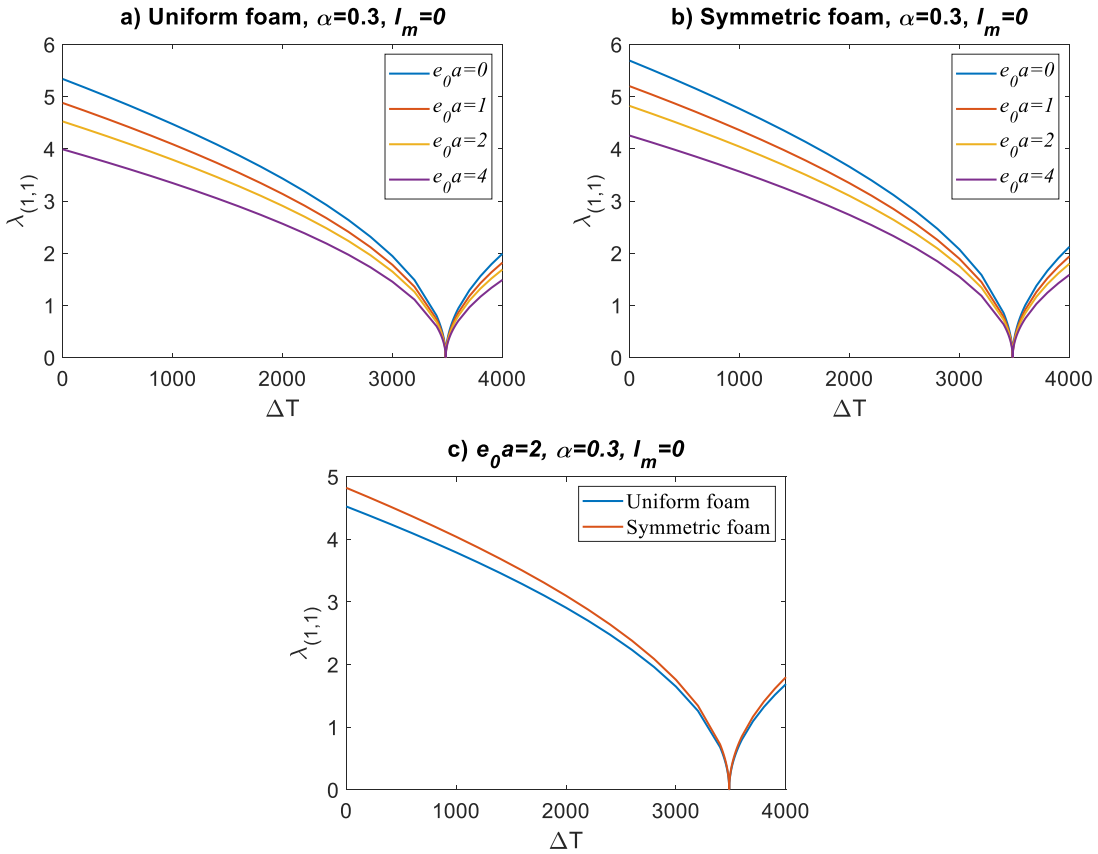

Figure 4 . Changing of the $\lambda_{(1,1)}$ depending on the ΔT and four distinct nonlocal parameters (e_0a=0, e_0a=0.3, e_0a=0.6, e_0a=0.9)

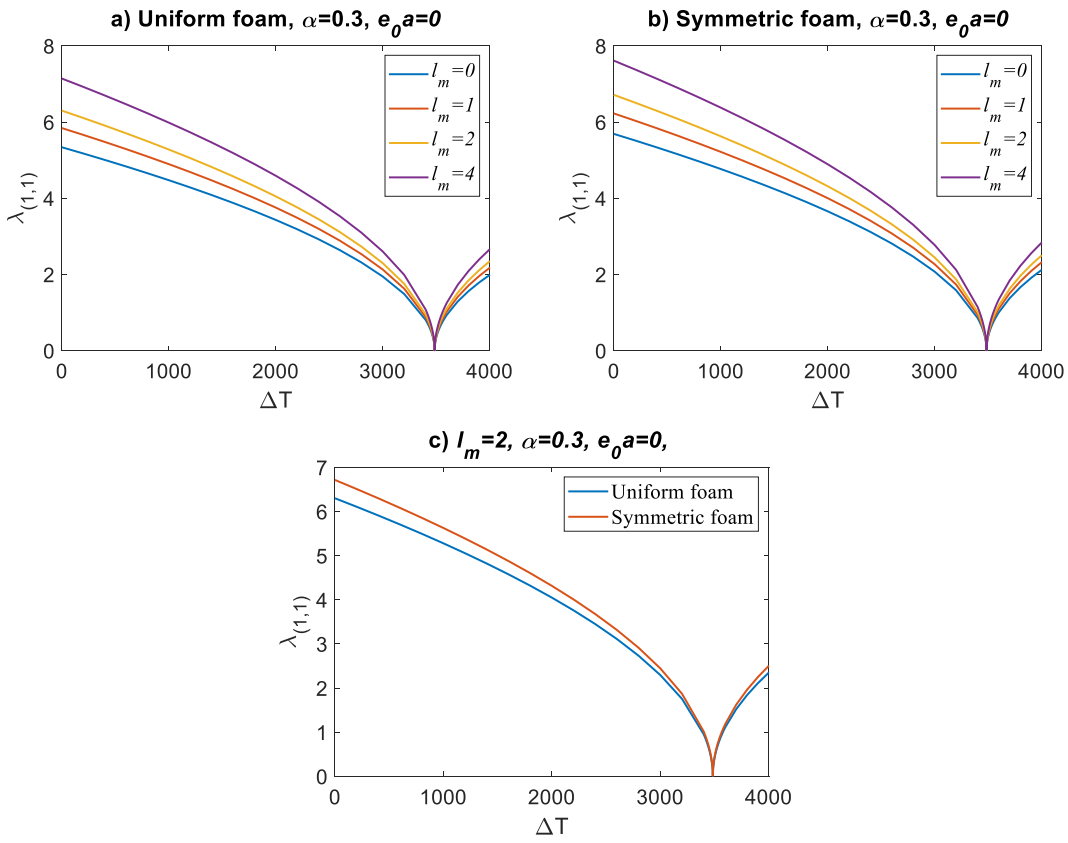

Figure 5 Changing of the $\lambda_{(1,1)}$ depending on the ΔT and four distinct material size factors (l_m=0, l_m=0.3, l_m=0.6, l_m=0.9)

3. Conclusions

In the current study, the buckling characteristics of a nanoplate made of nickel are investigated, with a particular focus on how temperature changes influence the buckling process. The study also examines the modeling of two distinct foam structures, the uniform and symmetric foam models, and explores how their material properties impact buckling behavior under thermal loading. Trigonometric functions are utilized to determine the thermal buckling characteristics of nanoplates within the framework of sinusoidal higher-order shear deformation theory.

A thorough analysis was conducted on the effects of several parameters, including temperature variations, foam type, foam void ratio, and the influence of material properties such as thermal expansion coefficients and stiffness. Nonlocal and material size factors were considered, highlighting their role in the nanoplate's stability under temperature-induced stresses. The findings provide valuable insights into the interplay between temperature changes and material characteristics, offering a deeper understanding of their impact on buckling behavior.

The results are consistent with previous studies that examined the influence of foam structures on the dynamic response and thermal stability of nanoplates. Similar to the findings in studies on nanocomposites and nanostructured materials, the present work emphasizes the importance of material properties, such as thermal expansion coefficients, in governing the thermomechanical behavior of foam nanoplates. This study contributes to the ongoing research on high-temperature applications and highlights the potential of foam nanoplates for engineering applications, especially in systems exposed to thermal loads.

Additionally, future studies may explore using advanced composite materials and hybrid nanostructures to investigate their potential for improving the mechanical properties and thermal stability of foam nanoplates under extreme conditions. Finally, exploring the effects of additional environmental factors such as humidity and pressure could provide a more comprehensive understanding of the nanoplate's performance in real-world applications.

•In the context of the symmetric foam model, the nanoplate's natural frequency experiences a decrease of 23.78% as the FVR grows. In contrast, the uniform foam model results in a more significant decrease of 51.5% in the nanoplate's natural frequency.

•When the FVR is 0, the component has no empty spaces. As the FVR increases, the natural frequency decreases.

•An observed correlation exists between the rise in the nonlocal parameter and the temperature difference, reflected in the reduction of the natural frequency.

•The natural frequency of the nanoplate reduces as the nonlocal parameter increases, whereas it increases when the material size factor is included in the equation.

Declaration

The author declared no potential conflicts of interest with respect to the research, authorship, and/or publication of this article. The author also declared that this article is original and was prepared in accordance with international publication and research ethics, and ethical committee permission or any special permission is not required.

Author Contributions

Mustafa Eroğlu developed the methodology, performed the simulation codes, and wrote the manuscript.

References

1. Ghorbanpour-Arani, A.H., Rastgoo, A., Sharafi, M.M., Kolahchi, R., and Ghorbanpour Arani, A., *Nonlocal viscoelasticity based vibration of double viscoelastic piezoelectric nanobeam systems*. Meccanica, 2016. **51**(1): p. 25–40.
2. Ghorbanpour-Arani, A.H., Rastgoo, A., Hafizi Bidgoli, A., Kolahchi, R., and Ghorbanpour Arani, A., *Wave propagation of coupled double-DWBNNTs conveying fluid-systems using different nonlocal surface piezoelasticity theories*. Mechanics of Advanced Materials and Structures, 2017. **24**(14): p. 1159–1179.
3. Ghorbanpour Arani, A., Miralaei, N., Farazin, A., and Mohammadimehr, M., *An extensive review of the repair behavior of smart self-healing polymer matrix composites*. Journal of Materials Research, 2023. **38**(3): p. 617–632.
4. Ghorbanpour Arani, A., Haghparast, E., and Ghorbanpour Arani, A.H., *Size-dependent vibration of double-bonded carbon nanotube-reinforced composite microtubes conveying fluid under longitudinal magnetic field*. Polymer Composites, 2014. **37**(5): p. 1375–1383.
5. Meng, M., Yuan, Y., Liu, J.G., Geng, C., and Xu, S., *Phosphor-Converted LEDs Based on CdSe/CdS Quantum Rod–BN Nanoplate Assembly*. ACS Applied Nano Materials, 2024. **7**(12): p. 14719–14726.
6. Lin, Y., Qin, C., Fang, L., Wang, J., and Li, D., *Colored Polymeric Films with a Bilayer Porous Design for Efficient Subambient Radiative Cooling*. ACS Applied Polymer Materials, 2024. **6**(1): p. 722–731.
7. Zhao, X., Tang, Y., Wang, J., Li, Y., Li, D., Zuo, X., and Yang, H., *Visible Light Locking in Mineral-Based Composite Phase Change Materials Enabling High Photothermal Conversion and Storage*. ACS Applied Materials & Interfaces, 2023. **15**(42): p. 49132–49145.
8. Kohashi, K., Okano, Y., Tanisawa, D., Kaneko, K., Miyake, S., and Takashiri, M., *Surface Modification of Bi2Te3 Nanoplates Deposited with Tin, Palladium, and Tin/Palladium Using Electroless Deposition*. Crystals, 2024. **14**(2): p. 132.
9. Son, J.S., Choi, M.K., Han, M.-K., Park, K., Kim, J.-Y., Lim, S.J., Oh, M., Kuk, Y., Park, C., Kim, S.-J., and Hyeon, T., *n-Type Nanostructured Thermoelectric Materials Prepared from Chemically Synthesized Ultrathin Bi2Te3 Nanoplates*. Nano Letters, 2012. **12**(2): p. 640–647.
10. Zhu, H., and Fan, L., *Nanofluids effect on the overall transfer coefficients change mechanism analysis*.

Energy Science & Engineering, 2023. **11**(2): p. 4481–4492.

11. Zolfalizadeh, M., Zeinali Heris, S., Pourpasha, H., Mohammadpourfard, M., and Meyer, J.P., *Experimental Investigation of the Effect of Graphene/Water Nanofluid on the Heat Transfer of a Shell-and-Tube Heat Exchanger*. International Journal of Energy Research, 2023. **2023**(1): p. 1–16.
12. Carrillo-Berdugo, I., Midgley, S.D., Grau-Crespo, R., Zorrilla, D., and Navas, J., *Understanding the Specific Heat Enhancement in Metal-Containing Nanofluids for Thermal Energy Storage: Experimental and Ab Initio Evidence for a Strong Interfacial Layering Effect*. ACS Applied Energy Materials, 2020. **3**(9): p. 9246–9256.
13. Al-Waily, M., Raad, H., and Njim, E.K., *Free Vibration Analysis of Sandwich Plate-Reinforced Foam Core Adopting Micro Aluminum Powder*. Physics and Chemistry of Solid State, 2022. **23**(4): p. 659–668.
14. Wang, Y., and Zhang, Z., *Non-Local Buckling Analysis of Functionally Graded Nanoporous Metal Foam Nanoplates*. Coatings, 2018. **8**(11): p.389.
15. Eroğlu, M., Esen, İ., and Koç, M.A., T*hermal vibration and buckling analysis of magneto-electro-elastic functionally graded porous higher-order nanobeams using nonlocal strain gradient theory*. Acta Mechanica, 2024. **235**(2): p. 1175–1211.
16. Zhao, N., Ye, R., Tian, A., Cui, J., Ren, P., and Wang, M., *Experimental and Numerical Investigation on the Anti-Penetration Performance of Metallic Sandwich Plates for Marine Applications*. Journal of Sandwich Structures & Materials, 2019. **22**(2): p.494-522.
17. Sun, C., Albustani, H., Phadnis, V.A., Nasr, M., Cantwell, W.J., and Guan, Z., *Improving the structural integrity of foam-core sandwich composites using continuous carbon fiber stitching*. Composite Structures, 2023. **324**: p., 117509.
18. Mocian, O., Constantinescu, D.M., and Indreș, A., *Assessment on Energy Absorption of Foam Core Sandwich Panels Under Low Velocity Impact*. Macromolecular Symposia, 2021. **396**(1).
19. Ozer, S., Haciyusufoglu, F., and Vural, E., *Experimental investigation of the effect of the use of nanoparticle additional biodiesel on fuel consumption and exhaust emissions in tractor using a coated engine*. Thermal Science, 2023. **27**(4): p. 3189–3197.
20. Vural, E., Özer, S., Özel, S., and Binici, M., *Analyzing the effects of hexane and water blended diesel fuels on emissions and performance in a ceramic-coated diesel engine by Taguchi optimization method*. Fuel, 2023. **344**: p. 128105.
21. Chen, D., Yang, J., and Kitipornchai, S., *Elastic buckling and static bending of shear deformable functionally graded porous beam*. Composite Structures, 2015. **133**: p. 54–61.
22. Yang, J., Chen, D., and Kitipornchai, S., *Buckling and free vibration analyses of functionally graded graphene reinforced porous nanocomposite plates based on Chebyshev-Ritz method*. Composite Structures, 2018. **193**: p. 281–294.
23. Wang, Y.Q., and Zhao, H.L., *Free vibration analysis of metal foam core sandwich beams on elastic foundation using Chebyshev collocation method*. Archive of Applied Mechanics, 2019. **89**(11): p. 2335–2349.
24. Garg, A., Chalak, H.D., Li, L., Belarbi, M.O., Sahoo, R., and Mukhopadhyay, T., *Vibration and Buckling Analyses of Sandwich Plates Containing Functionally Graded Metal Foam Core*. Acta Mechanica Solida Sinica, 2022. **35**(4): p. 1–16.
25. Touloukian, Y.S., *Thermophysical properties of high temperature solid materials*. Macmillan, 1967.
26. Kiani, Y., and Eslami, M.R., *An exact solution for thermal buckling of annular FGM plates on an elastic medium*. Composite Part B: Engineering, 2013. **45**(1): p.101–110.
27. Zhang, D.G., *Thermal post-buckling and nonlinear vibration analysis of FGM beams based on physical neutral surface and high order shear deformation theory*. Meccanica, 2014. **49**(2): p.283–293.
28. Eringen, A.C., *Theories of nonlocal plasticity*. International Journal of Engineering Science, 1983. **21**(7): p.741–751.
29. Lim, C.W., Zhang, G., and Reddy, J.N., *A higher-order nonlocal elasticity and strain gradient theory and its applications in wave propagation*. Journal of the Mechanics and Physics of Solids, 2015. **78**: p.298–313.
30. Farajpour, A., and Rastgoo, A., *Influence of carbon nanotubes on the buckling of microtubule bundles in viscoelastic cytoplasm using nonlocal strain gradient theory*. Results in Physics, 2017. **7**: p.1367–1375.
31. Eringen, A.C., *On differential equations of nonlocal elasticity and solutions of screw dislocation and surface waves*. Journal of Applied Physics, 1983. **54**(9): p.4703–4710.
32. Li, L., Li, X., and Hu, Y., *Free vibration analysis of nonlocal strain gradient beams made of functionally graded material*. International Journal of Engineering Science, 2016. **102**: p.77–92.
33. Żur, K.K., Arefi, M., Kim, J., and Reddy, J.N., *Free vibration and buckling analyses of magneto-electro-elastic FGM nanoplates based on nonlocal modified higher-order sinusoidal shear deformation theory*. Composite Part B: Engineering, 2020. **182**.
34. Aghababaei, R., and Reddy, J.N., *Nonlocal third-order shear deformation plate theory with application to bending and vibration of plates*. Journal of Sound and Vibration, 2009. **326**(1–2): p.277–289.
35. Monaco, G.T., Fantuzzi, N., Fabbrocino, F., and Luciano, R., *Critical temperatures for vibrations and buckling of magneto-electro-elastic nonlocal strain gradient plates*. Nanomaterials, 2021. **11**(1): p.1–18.
36. Ramirez, F., Heyliger, P.R., and Pan, E., *Discrete layer solution to free vibrations of functionally graded magneto-electro-elastic plates*. Mechanics of

Advanced Materials and Structures, 2006. **13**(3): p.249–266.

Appendix

The coefficient of the **S** and **M** matrices:

$$s_{11} = (A_{11}k_1^2 + A_{66}k_2^2)c_2, \quad s_{12} = (A_{12} + A_{66})k_1k_2c_2, \quad s_{13} = (-B_{11}k_1^3 - (B_{12} + 2B_{66})k_1k_2^2)c_2$$

$$s_{14} = (-B_{11}^s k_1^3 - (B_{12}^s)k_1k_2^2)c_2, \quad s_{15} = (-X_{13}k_1)c_2, \quad s_{22} = (A_{66}k_1^3 + A_{22}k_2^2)c_2$$

$$s_{23} = (-B_2k_2^3 - (B_{12} + 2B_{66})k_1^2k_2)c_2, \quad s_{25} = (-X_{23}k_2)c_2$$

$$s_{33} = \big(D_{11}k_1^4 + 2(D_{12} + 2D_{66})k_1^2k_2^2 + D_{22}k_2^4 + (-N^T)(k_1^2 + k_2^2)\big)c_1,$$

$$s_{34} = \big((-N^T)(k_1^2 + k_2^2)\big)c_1,$$

$$s_{55} = \big(A_{55}^s k_1^2 + A_{44}^s k_2^2 + Z_{33} + g(-N^T)(k_1^2 + k_2^2)\big)c_1$$

$$s_{35} = (Y_{13}k_1^2 + Y_{23}k_2^2)c_2, s_{44} = \big((-N^T)(k_1^2 + k_2^2)\big)c_1$$

$$m_{11} = I_0c_1, \quad m_{13} = -k_1I_1c_1, \quad m_{14} = -k_1J_1c_1, \quad m_{22} = I_0c_1, \quad m_{23} = -k_2I_1c_1, \quad m_{24} = -k_2J_1c_1$$

$$m_{33} = \big(I_0 + I_2(k_1^2 + k_2^2)\big)c_1, \quad m_{34} = \big(I_0 + J_1(k_1^2 + k_2^2)\big)c_1, \quad m_{35} = J_0c_1$$

$$m_{44} = \big(I_0 + K_2(k_1^2 + k_2^2)\big)c_1, \quad m_{45} = J_0c_1, \quad m_{55} = K_0c_1$$

$$c_1 = \big(1 + l_m^2(k_1^2 + k_2^2)\big) \quad c_2 = \big(1 + e_0a^2(k_1^2 + k_2^2)\big)$$

Available online at www.dergipark.org.tr/en

INTERNATIONAL ADVANCED RESEARCHES
and
ENGINEERING JOURNAL

Journal homepage: www.dergipark.org.tr/en/pub/iarej

e-ISSN: 2618-575X

International Open Access

Volume 08
Issue 03

December, 2024

Research Article

Investigation of microstructure and microhardness properties of Nd: YAG laser welded galvanized steel plates

Arife Kübra Yontar [a,*] ***and Sinem Çevik*** [b]

[a]*Department Mechanical and Metal Technologies, Ondokuz Mayis University, 55300, Samsun, Turkey*
[b]*Department of Metallurgical and Materials Engineering, Ondokuz Mayis University, 55270, Samsun, Turkey*

ARTICLE INFO

Article history:
Received 02 September 2024
Accepted 02 December 2024
Published 20 December 2024

Keywords:
Galvanized Steel
Laser Welding
Microhardness
Microstructure

ABSTRACT

Modern industry has discovered many uses for stainless steel because of its excellent mechanical and physical qualities, outstanding resistance to oxidation and corrosion, hot and cold workability, and superior weldability. The development of lightweight, cost-effective materials is being driven by technological advances. Thus, in order to satisfy Industry 4.0 criteria, additional materials that are resistant to corrosion and oxidation are required. Utilizing galvanization has extended the lifespan of materials used in the chemical, automotive, and white goods sectors, among other industries. Zinc coating, often known as galvanizing, is one technique for surface protection. It is inevitable that welding techniques will become widely used in component manufacturing. Several welding techniques may be used on galvanized materials, but they also come with several drawbacks for the joined samples, including flaws, porosities, and solidification fissures. As a result, the popularity of laser welding (LW) has steadily risen. In the current research, Nd-YAG laser welding was used to combine 2mm thick sheet-galvanized steel sheets. Microhardness tests were used to assess welded samples to determine their mechanical characteristics. Experimental results showed that the microhardness of the welded area was higher than that of the base metal. The microstructure of the welded samples was also examined using SEM and EDS mapping to look for flaws in the base metal, coating, welded area, and HAZ. SEM images revealed that a martensite structure was formed in the weld area, and a smooth joining process was achieved.

1. Introduction

New and innovative welding methods are becoming more and more necessary as technology advances rapidly. When deciding on a welding joint method to utilize, consideration is given to factors such as cost, quality, automation, and time efficiency. The ability of welded joints to meet requirements including self-attraction, impact resistance, corrosion resistance, and strength properties-as well as pre-, intermediate, and final annealing-is crucial. Aside from these, factors including investment costs, operational and consumable expenses, and the choice and application of filler metal are considered when determining the best technique to utilize [1, 2].

Gas tungsten arc welding (GTAW) is a common industrial technique for joining nearly any metallic material, including stainless steel, aluminum, nickel, and nickel alloys. Between the tungsten electrode and the sample in GTAW, an arc is created by a combination of argon, helium, or all shielding gas burning freely [3, 4]. GTAW welding has some disadvantages, such as the mixing of the tungsten electrode with the weld bead, oxide residues, pore formation, insufficient melting, and the formation of end crater cracks [5–7].

The joining procedures must be extended to lower dimensions due to the constant condition of the gadget parts. Conventional welding techniques are not applicable when small-sized items are employed in production settings. The most effective joining technique available today is laser beam welding, an advanced method whose benefits include deep penetration, low heat input, fast welding speed, negligible distortion, and use in an aqueous environment [8, 9]. The low energy input and high joint strength of the material to be welded makes it attractive since the heat in the weld zone has less of an effect on it. The base material's microstructure changes minimally due to the low linear energy input, which produces a smaller weld zone and heat-affected zone (HAZ).

* Corresponding author. Tel.: +*903623121919*
E-mail addresses: kubra.demirbas@omu.edu.tr *(A.K. Yontar)*, sinemu@omu.edu.tr *(S. Çevik)*
ORCID: 0000-0003-1486-9332 *(A.K. Yontar)*, 0000-0002-3506-7892 *(S. Çevik)*
DOI: 10.35860/iarej.1541710

Its additional features are its excellent power density and outstanding focusability in the few nanometer regions. The ability of the lens to focus light on focal points smaller than 0.005 inches makes the lens's participation in this process crucial [10–12]. The advantages of laser welding are its fast speed, limited heat-affected zone, deep penetration, high-quality welding joints, low heat input per unit volume, dispersion of fiber optic beams, and ease of robot operation [13]. A few milliseconds is all that is needed as a welding time to achieve high production rates and avoid metallurgical internal structural changes. Since shielding gas and a vacuum environment are not needed for the generation of laser beams, they provide substantial cost and speed benefits, particularly in mass production. As a result, laser welding makes combining tiny, thin parts feasible to create a narrow, smooth weld seam [14–16]. The laser source works on the concept that light energy is transformed into heat energy on the component's surface to be welded when the focal point is aimed. Before the heat-affected zone (HAZ) forms, the piece's outer layer starts to melt, and condensed energy facilitates melting and bonding [17].

1.06 micron light is produced using a neodymium-YAG solid-state laser, which employs an industrial crystal as its active substrate. It can run on beam powers ranging from around 100W to 3kW. Nd: YAG solid-state lasers can produce 10-kW brief pulses despite having lower average powers than CO_2 gas lasers. The 1kW Nd: YAG laser equipment can weld 4mm thick steel forehead at a pace of 0.3 meters per minute with great speed. The most significant benefit is that, because of the wavelength of the laser beam it generates, it makes control easier by allowing energy to be sent across fiber optic cables [18, 19].

Due to their excellent corrosion resistance, galvanized steels have seen significant growth in application in the automobile sector in the last decade. Galvanized steels exhibit high performance in both low and high-temperature service situations. As per the findings of other steels, vehicles with galvanized steels have lower weights and, thus, use less gasoline. Thus, cost-effective manufacture and increased vehicle safety may be guaranteed [20–22]. Galvanization is a commonly employed technique that involves applying a zinc coating to the surface of steel in order to prevent the effects of corrosion. By submerging the iron and steel in the molten zinc bath, zinc, and zinc compounds are often present in many layers of this protective coating. Galvanizing modifies the intricate structure of the layers, which has an impact on characteristics like chemical activity, diffusion, and subsequent cooling [23–25]. It is common practice to join galvanized steel using conventional welding techniques, which are identical to those employed for joining noncoated steel. Zinc is not as soluble as steel, though, and it has a lower melting point. Steel begins to melt around 1809 K, whereas zinc vaporizes at 1180 K thermal temperature [26]. Because of this, zinc burns during the welding process, resulting in porosity, various flaws, fractures, HAZ softening, and zinc depletion in the weld zone. Laser welding is an excellent approach to combining galvanized steel to prevent these unwanted issues. Because flaws, fractures, and porosities reduce the weld seam's mechanical strength, which is unacceptable in many applications. Therefore, in order to generate high-quality weldments, further study and developments for the joining of galvanized steels by laser welding are required [27–30].

The present study investigated the weldability of galvanized steel, which was joined by the Nd- YAG laser welding method. The microstructural examination of the welded specimens is carried out with the optical microscope and SEM/ EDS analyses. The hardness of the laser welded specimens is measured with the Vickers hardness tester.

2. Materials And Methods

2.1 Preparation of galvanized steel plates

The galvanized steel sheet with a length of 10 cm and a thickness of 2 mm was cut into ten equal pieces with the SRGM 1360-SAYMAK cutting device shown in Figure 1(a). The simulated and authentic appearance of the samples prepared before welding are shown in Figures 2(b) and (c).

2.2 Nd: YAG laser welding of galvanized steels

The experiments focused on laser welding with a solid-state Nd: YAG-laser. 1470 watts of power were used, and the focal length was over 0 to 15 and 20 mm in travel speeds. As maximum output power, 4 kW is used. All parameters used in the welding application are given in Table 1. When butt welding, especially in butt welding of galvanized steels, the gap between the samples must be adjusted precisely one hand, issues such as porosity and discontinuity in welding joints can be readily generated if the sheets are firmly secured together due to the notable difference between the melting temperature of steel (1583° C) and the zinc's evaporation temperature (906° C). However, excessive gaps result in poor weld appearance and, in certain situations, even impair the ability of the workpieces to be effectively integrated into one another. According to Mei et.al.(2009) [13], the gap should be controlled within 10% of the thickness of the workpiece in deep-penetration laser welding. Considering all of those affecting factors, while the workpieces are fixed, the gap between workpieces should be controlled within 0.15–0.2 mm. The appearance of samples after welding is shown in Figure 2 (a).

Four total samples were prepared by cutting the laser-welded specimens into tiny pieces with a 0.5–1 cm diameter to confine the weld zone for the optical microscope and hardness tests. After sanding and etching, the mounted

samples were evaluated under an optical microscope. The etching solution consisted of 20 mL of ethanol, 20 mL of hydrochloric acid, and one gram of cuprous chloride dihydrate solution. Images of metallographically prepared samples are shown in Figure 2 (b).

Table 1. Welding parameters.

Flow Rate	6-7 L/dk
Current Setting	60-70 A
Gas Type	Argon
Gas Setting	1.2 L
Angle Between Metal-Piece	20°

2.3 Characterizations

The stereo microscope (Leica DM2500 P) was used to evaluate the microstructure and the defect distribution of the polished surface of the welded specimen. The hardness values of the samples were measured at 3 mm intervals by applying a force of 0.98 kg for 15 seconds using the TMTECK HV-1000B Micro hardness device. The effect of the welding process on the hardness of the alloy was examined by comparing the hardness values of the welding zone, the heat-affected zone, and the base metal zone. A JEOL 7001F field emission (FE) scanning electron microscope with an EDS attachment and an 80mm^2 X-MAX detector was used to investigate the substances' microstructural characterization and EDS chemical mapping. A Scanning Electron Microscope (SEM) examination was conducted for every Nd: YAG laser-welded specimen. Energy-dispersive spectroscopy (EDS) was used to analyze materials semiquantitatively chemically. The compositions of the welded samples were determined through map analysis and EDS spectra. Thus, research is done on how many elements, including zinc vaporization, shielding gas, welding speed, laser power, and focal location, affect the quality of the welded joints. The behavior of the weld pool during zero-gap and butt laser welding was thoroughly investigated.

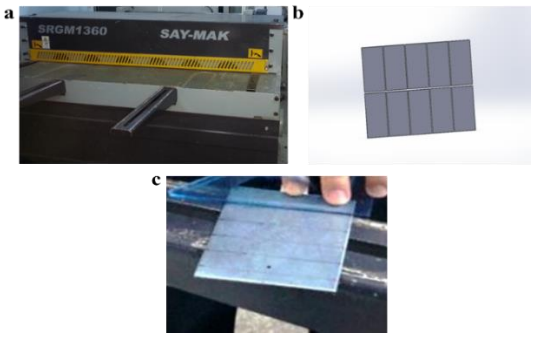

Figure 1. (a) Cutting Device, (b) simulation of samples prepared before cutting, and (c) galvanized steel plate prepared for cutting.

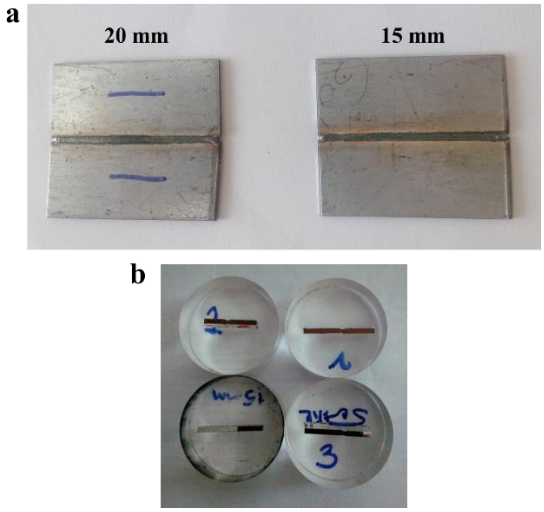

Figure 2. (a) Nd: YAG laser welded samples and (b) metallographically prepared samples.

3. Results And Discussion

3.1 Optical Microscope Analysis

The optical microscope images in Figure 3 clearly show that the laser-welded steel has a smooth and homogeneous structure. It is also seen that the plates of the same thickness, which are joined together with the laser welding, are uniform and smooth. The galvanized steel joined by the laser welding method has a crack-free, fault-free welding appearance in HAZ. It is obvious that the welded area of the sample joined with a 15 mm focal length, shown in Figure 3 (a), is broader and more uniform. However, the sample with a 20 mm focal length does not have pores, indicating that the joint is of higher quality and more integrated. As shown in Figures 3 (a) and (b), excessive grain growth is not a concern in the HAZ of laser-welded specimens. This shows us that both welded joints have no negative effect on toughness and deformability.

It is crucial to consider how the laser's power affects the weld's width and depth. As laser power increases, the weld's depth and breadth also rise [13]. This is due to the fact that when laser power grows, so does the quantity of heat input. The laser may achieve complete penetration when its power exceeds 1300W. The aspect ratio of the weld joint falls, and the increasing rate for the depth and width of the weld seam is less than that for the width of the weld seam when the laser power exceeds 1300W. As a result, in the current investigation, an adequate laser power of around 1470 W is used. As well known, the keyhole effect is the essential characteristic of deep-penetration laser welding, which plays a vital role in the energy coupling during the welding process [31, 32]. Therefore, this effect can be clearly seen in Figure 3.

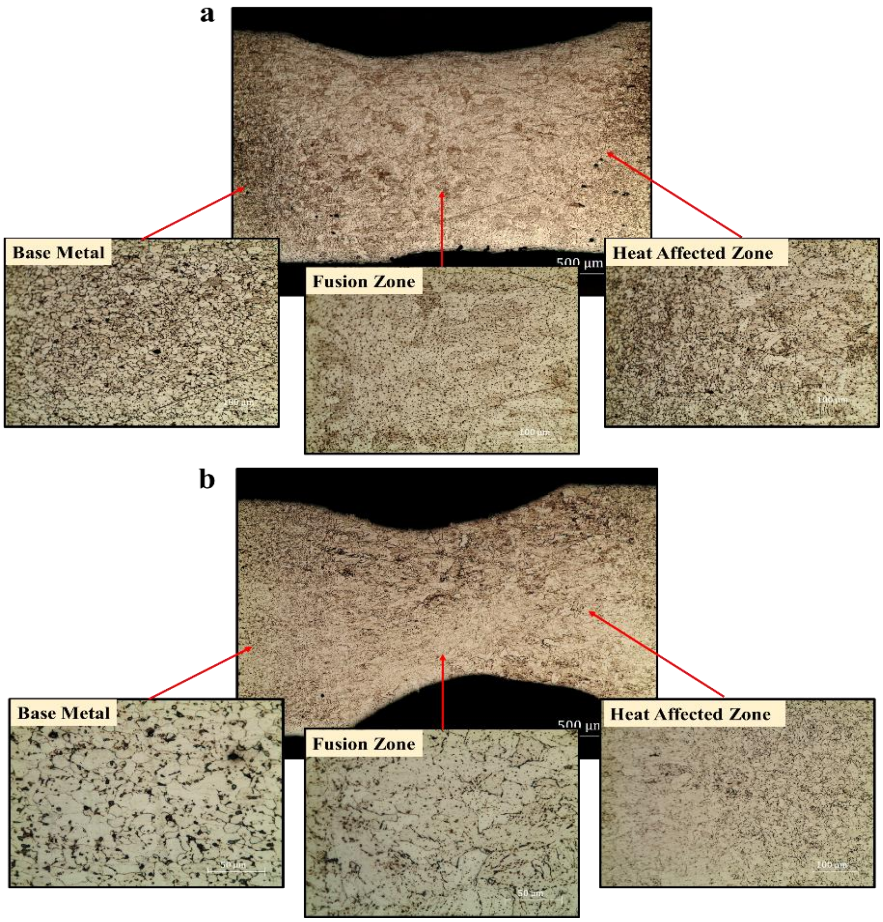

Figure 3. Optical microscope images of (a) steel sample welded with laser at 15 mm focal length and (b) steel sample welded with 20 mm focal length.

3.2 SEM and EDS analyses

When the laser power is greater than 1200W, some very small pores are observed in HAZ, as shown in Figure 4(a) HAZ image. As laser power drops, the number of pores falls as well. Low laser power is claimed to be able to prevent pore development by lowering the generation of metal vapor. Zinc vaporization is one of the main factors boosting splashing electric spark and porosity during laser welding of galvanized steel sheets. On the other hand, rapid zinc evaporation lowers the amount of zinc in the welding joint, and HAZ expands the hazardous area, weakens welding stability, and ruins the galvanized layer, all of which will eliminate the galvanized steel's protective layer. Furthermore, quick zinc vaporization lowers the quality of welding connections, creates internal tension, pores, and cracks in the joints, and makes safeguarding focusing mirrors more challenging. Shielding gas serves several crucial purposes in high-power deep-penetration laser welding, including preventing oxidation of the workpiece surface, ensuring that zinc vapor has no effect, suppressing the creation of pores, and clearing the plasma cloud that absorbs and disperses laser energy. Plasma can be restrained to reduce the strength of the plasma density by choosing the suitable shielding gas. Appropriate plasma in the keyhole is beneficial to improve the workpiece's absorption of laser energy and, therefore, boost weld penetration. The side-blow shielding gas used in this investigation to protect the welding joints is argon (Ar). In a high-temperature melt pool, nitrogen (N_2) causes a metallurgical reaction with a base metal substance [33–35]. Nitrogen, a comparatively reactive gas, can react with the weld metal when utilized as a shielding gas because it dissolves in the pool at high temperatures. Instead of reacting with the base metal, argon is an inert gas. Consequently, nitrogen has a far deeper penetration depth than argon does. Porosity and nitride, however, appear in the welds because nitrogen molecules can split into nitrogen atoms (N_2- 2[N]). Since the weld metal has porosity, the nitrogen can achieve the ideal penetration criterion but not the formability criteria [36]. Ar is selected as shielding gas during the welding process to obtain better manufacturing performance for tailor-welded sheets. So, no deformation, distortion, porosities, or failures are observed in the fusion zone and base metal of samples seen in Figure 4. Heat-induced decomposition of moisture that is either adhered to the workpiece surface or present in the ambient into hydrogen can result in the creation of pores in welding joints. It can be seen that after taking these measures, the welding joints are of high quality and practically free of pores, as shown in Figure 4.

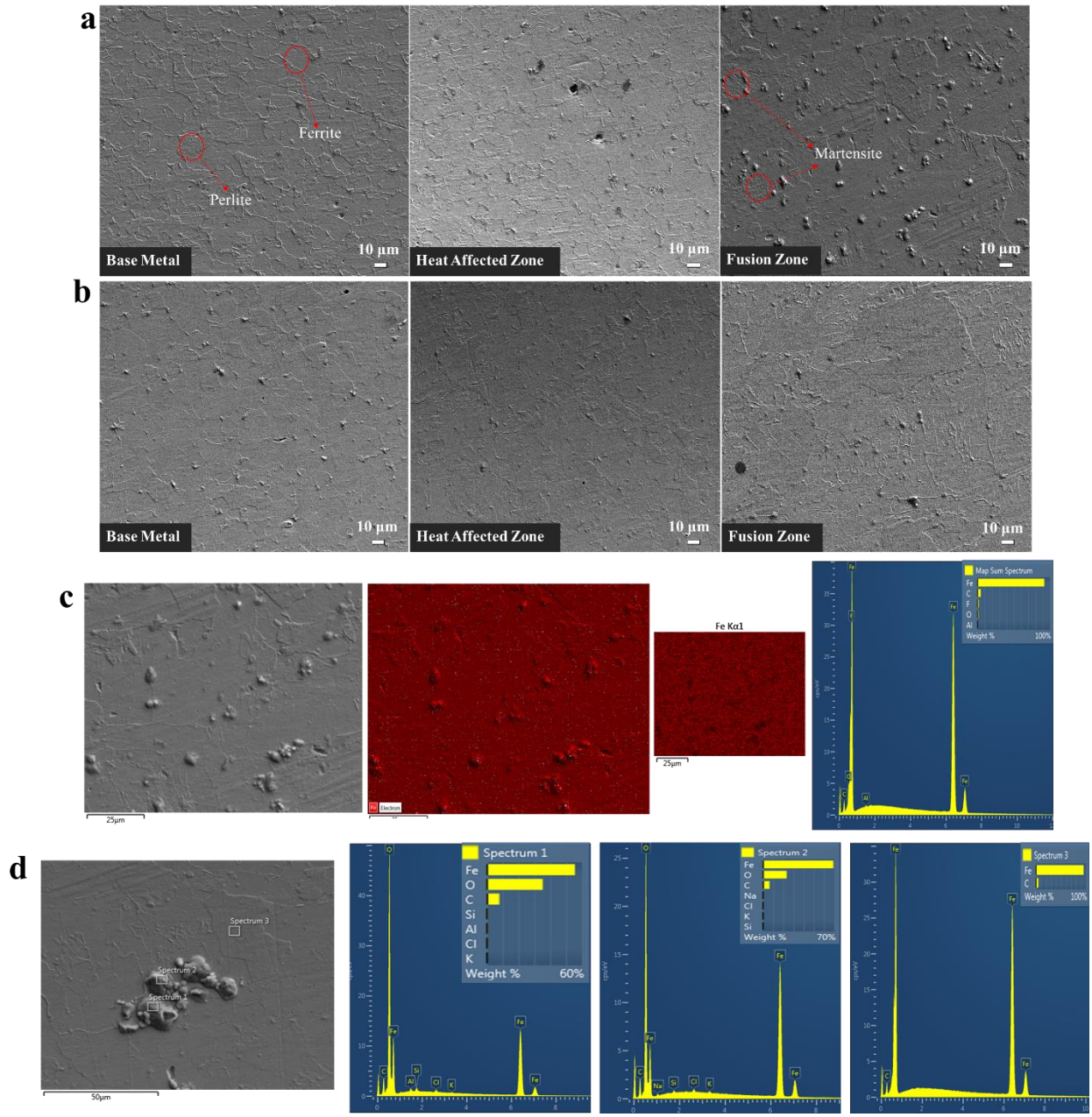

Figure 4. SEM images of (a) 15 mm focal length welded sample, (b) 20 mm focal length welded sample, EDS results of (c) 15 mm focal length welded sample, (d) 20 mm focal length welded sample.

As seen in Figure 4 (a) and (b), the base metal consists of ferrite and pearlite, which is a typical steel microstructure [37]. It is understood that the grains grow as we move from the base metal to the heat-affected zone (HAZ) and the weld zone. As is known, when metals are heated to a temperature above the recrystallization temperature, a phenomenon called grain growth occurs. The grain growth rate increases as the temperature increases, and the growth accelerates as the solidus of the metal approaches. Coarse-grained structures are more brittle and fragile than fine-grained structures [38–40]. Figure 4 shows an island of martensite in the weld regions, typically expected due to the rapid cooling rates inherent in the laser welding process. A coarser martensite structure formed after cooling as a result of the austenite's more immense grain development produced by the higher peak temperature [40, 41].

Energy-dispersive X-ray Spectroscopy (EDS) was used to detect the atomic percent of the zinc and the iron distribution in the preheated zone and the welds. Also, in order to determine the changes in the chemical composition of the material caused by the influence of the laser beam, the distribution of elements in different zones in deep-penetration laser welds is tested by EDS/SEM. It can be seen in Figures 4 (c) and (d) because, compared to base metal, the elements and their atomic fraction in welding joints have changed accordingly. Factors such as Si, C, O, and Fe exhibit

varying degrees of fluctuation in distribution from the welding joint to the base metal. This helps to explain why the elements in welding joints differ from those in the base metal. The equilibrium in the fusion zone's crystallization mechanism is the cause, and the fast cooling rate of welding joints results in insufficient phase transition and diffusion of alloy components. Thus the solute element deviates from its average density due to the unequal chemical composition distributions. If the welding speed is too fast, the time for the melt pool to resolidify is short, making it easy to produce pores in welding joints due to the zinc vaporization during welding [42–44]. Since the amount of zinc was very low and evaporation occurred during the welding process, Zn element was not detected in the EDS results.

3.3 Micro Vickers Hardness

The butt welding Nd: YAG-laser welding of Vicker's micro-hardness measurement was carried out in order to determine the hardness distribution profiles along the weld zone, heat-affected zone (HAZ), and base metal. As can be seen from Figure 5 (b) and (c), the Vickers hardness values were measured by applying a force at a total of 15 points at intervals of 0.5 mm from the two sides of the welding region of the samples. The martensitic transformation in the weld zone and in the heat-affected zone increases the hardness in the zones compared to the hardness of the base metal. The increased hardness in the welding zone can be attributed to re-austenitization and the formation of a martensitic structure upon cooling [41]. The hardness results graph given in Figure 5 (a) shows that the hardness value of the weld zone is harder than the base metal and HAZ for the three samples due to the martensitic transformation of the grains. Samples G 15.1 and G 15.2 are laser-welded samples with a focal length of 15 mm. Samples G 20.1 and G 20.2 are laser-welded samples with a focal length of 20 mm. According to the study, the galvanized steel joined by laser welding has a smoother weld zone, and microstructural examinations show no defect in the structure and a solid joint. According to the microhardness values obtained in base metal, HAZ, and

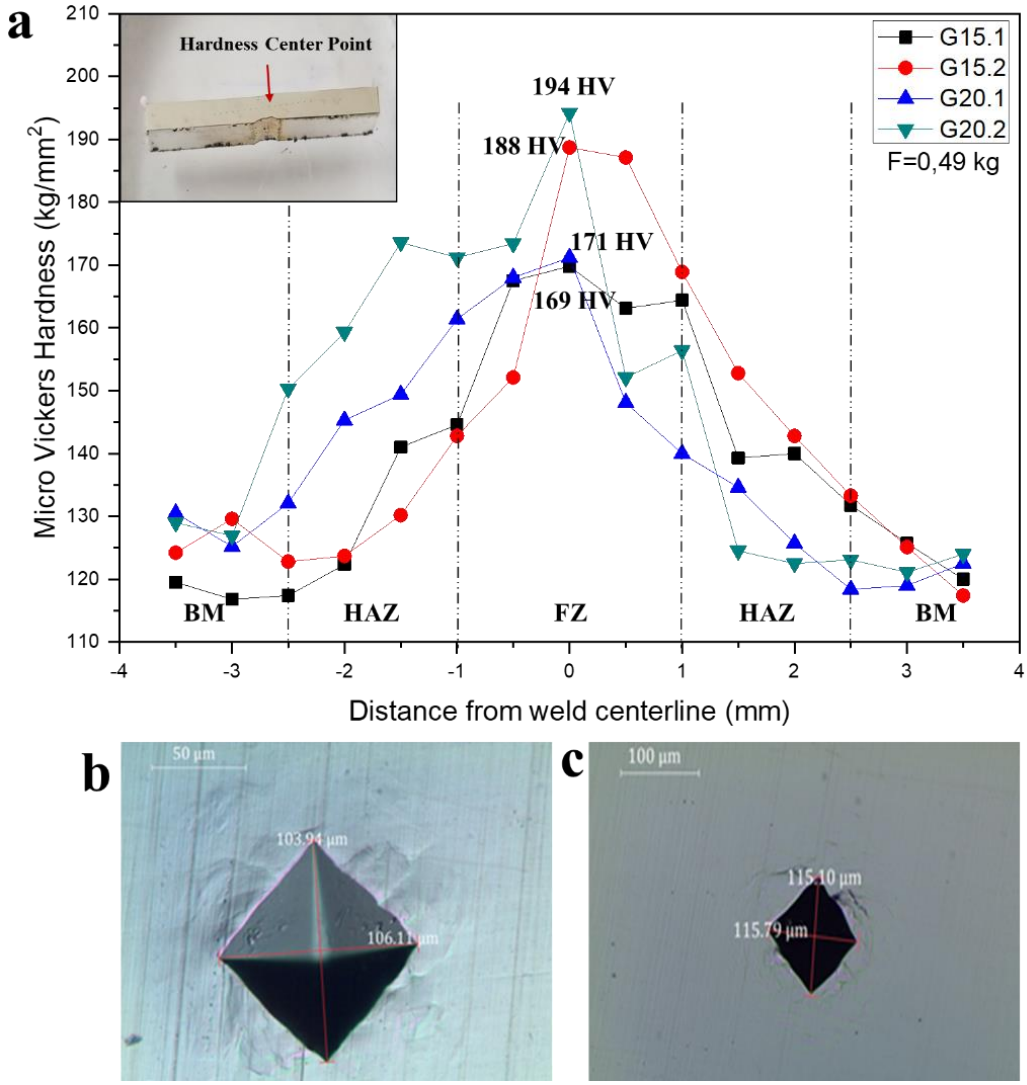

Figure 5. (a) Microhardness result graph of all samples, (b) Hardness trace measurement in the optical microscope of laser welded steel with a focal length of 15 mm, and (c) Hardness trace measurement of laser-welded steel optical microscope with a focal length of 20 mm.

fusion zone, laser welding of galvanized steel sheets does not soften HAZ. The fusion zone's hardness is about 1.5 times greater than that of the base metal due to the quick heating and cooling rate of laser welding, which also results in little lateral displacement of the welding joint. Furthermore, welding joints' hardness can be shielded from the effects of stress concentration by using quick heating and cooling rates. Figure 4 illustrates that the fusion zone's metallurgical structure is upperbainite + low-carbon martensite, whereas the HAZ's metallurgical structure is upperbainite + low-carbon martensite + ferrite. As low-carbon martensites exist, welding joints don't have a particularly high toughness. HAZ's greater hardness than base metal confirms that laser-welded galvanized steel sheets do not cause HAZ to become softer. This is attributed to the fact that the heating and cooling rates are fast enough during laser welding, and the incomplete annealed zone of HAZ is extremely narrow. Moreover, a certain amount of hardened layer is produced in HAZ during laser welding. The measurements of hardness distributions in the cross-section of welding joints have shown that the hardness in the fusion zone significantly increased compared with the base metal. As a result, it was determined that the hardness values of the weld zone increased compared to the base metal in all samples, and the hardness increased with the increase in focal length..

Conclusions

In the current study, the changes in microstructure and microhardness of galvanized steel plates joined by Nd: YAG laser welding were investigated. According to experimental findings, welding joints had greater strength and microhardness than the base metal. It was determined that a martensite structure was formed in the weld area due to rapid cooling, and therefore, the hardness value increased. As a result, the welding quality is trustworthy while producing metal components. It is possible to get joints free of pores and fractures under the circumstances of this experiment. The fusion zones exhibit incredibly high levels of grain refinement as a result of their rapid recrystallization and high welding rate, which raises the hardness of these areas relative to the base metal. SEM images revealed that there were no welding defects in the welding area of the sample combined with a focal length of 20 mm and that a successful process was carried out. In addition, EDS results also showed that zinc was removed from the metal due to high heat and cooling rates in the weld zone. This study showed that 2 mm thick galvanized plates can be successfully welded with a focal length of 20 mm. Thus, new laser welding parameters and their effects were introduced to literature and applications.

Declaration

The author(s) declared no potential conflicts of interest with respect to the research, authorship, and/or publication of this article. The author(s) also declared that this article is original and was prepared in accordance with international publication and research ethics, and ethical committee permission or any special permission is not required.

Author Contributions

A.K. Yontar and S. Çevik developed the methodology. Arife Kübra Yontar performed the analysis. S. Çevik supervised and improved the study. A.K. Yontar and S. Çevik wrote the manuscript together. A.K. Yontar and S. Çevik proofread the manuscript.

References

1. Wang B, Hu SJ, Sun L, Freiheit T. *Intelligent welding system technologies: State-of-the-art review and perspectives*. Journal of Manufacturing Systems 2020; **56**: p. 373–391.
2. Karayel E, Bozkurt Y. *Additive manufacturing method and different welding applications*. Journal of Materials Research and Technology 2020; **9** (5): p. 11424–11438.
3. Manh NH, van Nguyen A, Le Duy H et al. *Development of a novel GTAW process for joining ultra-thin metal sheets.* Journal of Manufacturing Processes 2022; **80** (2): p. 683–691.
4. Ebrahimpour A, Salami S, Saeid T. *Experimental and finite element investigation on hybrid GTAW-GMAW of duplex stainless steel*. International Journal Of Advanced Manufacturing Technology 2023; **125** (3-4): p. 1543–1557.
5. Weis S, Grunert R, Brumm S, Prank U. *Study on MIG-TIG hybrid brazing of galvanized thin sheet.* Weld World 2023; **67** (5): p. 1215–1221.
6. Azadi Moghaddam M, Kolahan F. *Modeling and optimization of A-GTAW process using back propagation neural network and heuristic algorithms*. International Journal of Pressure Vessels and Piping 2021; **194** (December): p. 104531.
7. Voigt AL, Cunha TVd, Niño CE. *Conception, implementation and evaluation of induction wire heating system applied to hot wire GTAW (IHW-GTAW)*. Journal of Materials Processing Technology 2020; **281** (2): p. 116615.
8. Sadeghian A, Iqbal N. *A review on dissimilar laser welding of steel-copper, steel-aluminum, aluminum-copper, and steel-nickel for electric vehicle battery manufacturing*. Optics & Laser Technology 2022; **146** (8): p. 107595.
9. Katayama S, Kawahito Y, Mizutani M. *Latest Progress in Performance and Understanding of Laser Welding*. Physics Procedia 2012; **39** (3): p. 8–16.
10. Wallerstein D, Salminen A, Lusquiños F et al. *Recent Developments in Laser Welding of Aluminum Alloys to Steel*. Metals 2021; **11** (4): p. 622.
11. Razmpoosh MH, Macwan A, Biro E, Zhou Y. *Effect of coating weight on fiber laser welding of Galvanneal-coated 22MnB5 press hardening steel*. Surface and Coatings Technology 2018; **337**: p. 536–543.

12. Chludzinski M, dos Santos RE, Churiaque C et al. *Pulsed Laser Welding Applied to Metallic Materials—A Material Approach*. Metals 2021; **11** (4): p. 640.
13. Mei L, Chen G, Jin X et al. *Research on laser welding of high-strength galvanized automobile steel sheets*. Optics and Lasers in Engineering 2009; **47** (11): p. 1117–1124.
14. Zhao Y, Zhang Y, Hu W, Lai X. *Optimization of laser welding thin-gage galvanized steel via response surface methodology*. Optics and Lasers in Engineering 2012; **50** (9): p. 1267–1273.
15. Murzin SP, Kazanskiy NL, Stiglbrunner C. *Analysis of the Advantages of Laser Processing of Aerospace Materials Using Diffractive Optics*. Metals 2021; **11** (6): p. 963.
16. Deepak JR, R.P A, Saran Sundar S. *Applications of lasers in industries and laser welding: A review*. Materials Today: Proceedings 2023.
17. Lun N, Saha DC, Macwan A et al. *Microstructure and mechanical properties of fibre laser welded medium manganese TRIP steel*. Materials & Design 2017; **131**: p. 450–459.
18. Thorpe SJ, Quinlan N, Ainsworth RW. *The characterisation and application of a pulsed neodymium YAG laser DGV system to a time-varying high-speed flow*. Optics & Laser Technology 2000; **32** (7-8): p. 543–555.
19. Liu B, Ohodnicki PR. *Fabrication and Application of Single Crystal Fiber: Review and Prospective*. Advanced Materials Technologies 2021; **6** (9): p. 5.
20. Schmidt M, Otto A, Kägeler C. *Analysis of YAG laser lap-welding of zinc coated steel sheets.* CIRP Annals 2008; **57** (1): p. 213–216.
21. Chakraborty A, Ghosh R, Sudan M, Mondal A. *Improvement in hot dip galvanized coating microstructure and properties by pre-metallic deposition on steel surface: A comprehensive review*. Surface and Coatings Technology 2022; **449**: p. 128972.
22. Autengruber R, Luckeneder G, Hassel AW. *Corrosion of press-hardened galvanized steel*. Corrosion Science 2012; 63: p. 12–19.
23. Dan A, Bijalwan PK, Pathak AS, Bhagat AN. *A review on physical vapor deposition-based metallic coatings on steel as an alternative to conventional galvanized coatings*. Journal of Coating Technology Research 2022; **19** (2): p. 403–438.
24. Kania H, Mendala J, Kozuba J, Saternus M. *Development of Bath Chemical Composition for Batch Hot-Dip Galvanizing-A Review*. Materials (Basel) 2020; **13** (18).
25. Zhang Z, Zhao Y, Wu S, Lu H. *Optimization of butt welding of zinc-coated thin sheets with oscillating fiber laser beams: Weld formation, microstructure, and mechanical properties.* Weld World 2021; **65** (9): p. 1711–1723.
26. Ma J, Kong F, Carlson B, Kovacevic R. *Two-pass laser welding of galvanized high-strength dual-phase steel for a zero-gap lap joint configuration*. Journal of Materials Processing Technology 2013; **213** (3): p. 495–507.
27. Sinha AK, Anand A. *Development of an alternative for corrosive resistant galvanized steel compatible for laser welding.* Materials Today: Proceedings 2021; **46** (11): p. 9561–9563.
28. Kim C, Choi W, Kim J, Rhee S. *Relationship between the Weldability and the Process Parameters for Laser-TIG Hybrid Welding of Galvanized Steel Sheets*. Materials Transactions 2008; **49** (1): p. 179–186.
29. Górka J, Suder W, Kciuk M, Stano S. *Assessment of the Laser Beam Welding of Galvanized Car Body Steel with an Additional Organic Protective Layer*. Materials (Basel) 2023; **16** (2).
30. Bang H-S, Kim J-C, Go B-S et al. *The Pre-Heating Effect for Porosity Control during the Laser Welding of Galvanized Steel Sheets.* Applied Sciences 2024; **14** (7): p. 2987.
31. Üren N. *Ecological dyeing and UV-protective functionalization of cotton/lyocell blend fabrics designed for high comfort summer clothing*. International Advanced Researches and Engineering Journal 2024; **8** (1): p. 43–50.
32. Sibillano T, Ancona A, Berardi V, Lugarà PM. *Correlation analysis in laser welding plasma*. Optics Communications 2005; **251** (1-3): p. 139–148.
33. Xia H, Tan C, Tian R et al. *Influence of shielding gas on microstructure and mechanical properties of laser welded–brazed Al/steel lapped joint*. Journal of Manufacturing Processes 2020; **54** (4): p. 347–358.
34. Hafez KM. *The influence of shielding gases on keyhole-induced porosity and nitrogen absorption in SS 304 stainless steel fiber laser welds*. International Journal of Advanced Manufacturing Technology 2023; **127** (3-4): p. 1887–1894.
35. Baghdadchi A, Hosseini VA, Hurtig K, Karlsson L. *Promoting austenite formation in laser welding of duplex stainless steel—impact of shielding gas and laser reheating*. Weld World 2021; **65** (3): p. 499–511.
36. Chung BG, Rhee S, Lee CH. *The effect of shielding gas types on CO2 laser tailored blank weldability of low carbon automotive galvanized steel*. Materials Science and Engineering: A 1999; 272 (2): p. 357–362.
37. Shreyas P, Panda B, Vishwanatha AD. *Characteristics of stainless steel-galvanized steel joint: Effect of stainless steel composition and welding parameters*. Materials Today: Proceedings 2019; **19** (1–4): p. 468–473.
38. Yontar AK, Çevik S. *Corrosion behavior of fiber laser welded Ti-6Al-4V alloy rods with different pH and temperature in 0.9 wt% NaCl medium*. Research on Engineering Structures and Materials 2024; ; **10** (2): p. 537-557
39. Liu H, Shui J, Cai T et al. *Microstructural evolution and hardness response in the laser beam welded joints of pure titanium during recrystallization and grain growth*. Materials Characterization 2018; **145**: p. 87–95.
40. Rong Z, Li L, Chen L et al. *The effect of Zn coating layer on the microstructure and mechanical properties of friction stir spot welded galvanized DP590 high-strength steel plates*. International Journal of Advanced Manufacturing Technology 2021; **113** (5-6): p. 1787–1798.
41. Betiku OT, Shojaee M, Sherepenko O et al. *Optimizing post-weld performance of press-hardened steel resistance spot welds by controlling fusion zone porosity*. Weld World 2022; **66** (9): p. 1733–1746.
42. Hao Y, Wang H-P, Sun Y et al. *The evaporation behavior of zinc and its effect on spattering in laser overlap welding of galvanized steels*. Journal of Materials Processing Technology 2022; **306** (9): p. 117625.

43. Hao Y, Chen N, Wang H-P et al. *Effect of zinc vapor forces on spattering in partial penetration laser welding of zinc-coated steels*. Journal of Materials Processing Technology 2021; **298** (part-A): p. 117282.
44. Kim H, Inoue J, Kasuya T. *Unsupervised microstructure segmentation by mimicking metallurgists' approach to pattern recognition*. Scientific Reports 2020; **10** (1): p. 17835.